ELASTIC WAVE SCATTERING

IN CRACKED CYLINDERS

By

HAO BAI

A THESIS SUBMITTED IN PARTIAL FULFILLMENT OF

THE REQUIREMENTS FOR THE DEGREE OF

DOCTOR OF PHILOSOPHY

IN

THE FACULTY OF GRADUATE STUDIES

DEPARTMENT OF MECHANICAL AND INDUSTRIAL ENGINEERING

We accept this thesis as conforming

to the required standard

_____

_____

_____

_____

_____

THE UNIVERSITY OF MANITOBA

THE UNIVERSITY OF MANITOBA

FACULTY OF GRADUATE STUDIES

*****

COPYRIGHT PERMISSION

ELASTIC WAVE SCATTERING IN CRACKED CYLINDERS

BY

HAO BAI

A Thesis/Practicum submitted to the Faculty of Graduate Studies of The University of Manitoba in partial fulfillment of the requirement of the degree

of

DOCTOR OF PHILOSOPHY

Abstract

A brief review of the dispersion relations and Green's functions for cylinders is presented initially. Then a novel and computationally efficient numerical procedure is given for wave scattering by a circumferential crack in an isotropic as well as a laminated composite cylinder. By employing a wave function expansion in both the circumferential and axial directions, as well as symmetry and anti-symmetry decompositions, three dimensional wave scattering is reduced to two quasi-one-dimensional problems. This simplification greatly reduces the computational time. Illustrative numerical results are presented for the reflection and transmission coefficients of different incident wave modes in a steel cylinder and a laminated composite cylinder, each containing a crack having an arbitrary circumferential length and radial depth. They are shown to agree quite closely with available but limited experimental data.

The boundary element method is employed to analyze wave scattering by a crack that is oriented arbitrarily in an isotropic cylinder. However, computational data are presented for only two specific orientations that corresponding to an axial crack and a circumferential crack. A multidomain technique and 8-node quadrilateral elements handle the singularity introduced by the crack. Computed results show good agreement with limited available data.

Acknowledgement

I wish to thank most sincerely my advisors, Profs. N. Popplewell and A. H. Shah for their stimulating support. Their continuous guidance, encouragement, understanding and friendship helped immensely. My deep appreciation also goes to Prof. S. K. Datta for his readiness to help and have fruitful discussions. Furthermore, I wish to express my sincere appreciation to Prof. E. Lajtai for serving as an advisory member. In addition, useful discussions were held with my friends Dr. W. Zhuang and Dr. J. Zhu.

I would also like to thank all those staff and graduate students in the Department of Mechanical and Industrial Engineering, University of Manitoba, who freely offered much friendly assistance.

The financial support of a graduate fellowship from the University of Manitoba, NSERC research support from the operating grants of Profs. A. H. Shah and N. Popplewell, and a teaching assistantship from the Department of Mechanical and Industrial Engineering are acknowledged gratefully.

Finally, I would like to express my gratitude and love to my family who helped me in my study. In particular, my wife Yanyan and sons Owen and Kevin, my father and my deceased mother, and my parents-in-law provided continuous encouragement and support.

TABLE OF CONTENTS

LIST OF FIGURES

LIST OF TABLES

Chapter 1

Introduction

1.1 Nondestructive Evaluation

Nondestructive evaluation (NDE) is a family of specialized technical inspection methods that provides information about the condition of materials and components without impairing their future usefulness. NDE examines actual production pieces and reveals the presence of flaws which can be evaluated to accept or reject a piece. It is one of the major tools for quality control that is entrenched firmly in industries such as aerospace, automotive, power generation and transmission, pulp and paper, refinery, and shipbuilding. There are several established nondestructive testing (NDT) inspection methods currently in industrial use. They involve liquid penetrants, magnetic particles, radiography, ultrasonic waves or eddy currents.

Ultrasonic inspection uses complex electronic equipment but material which transmits mechanical vibrations can be tested for flaws. The ultrasonic instrumentation

converts electrical pulses into mechanical vibrations. The latter travel across a specimen and they are partially reflected from flaws. The reflected pulses can be reconverted to electrical energy that can be measured. Their timing and size determine the position and size of the flaws.

There are several available ultrasonic techniques such as pulse-echo, through-transmission, resonance, frequency modulation, and acoustic imaging. Early techniques used body waves followed later by guided waves. Guided waves have the following advantages.

- The dispersive and multimodal nature of guided waves can be used to generate many data points in a given frequency range.
- The speed of a guided wave is very sensitive to a material's properties.

Comprehensive knowledge of guided waves in a cylinder plays an important role in ultrasonic, nondestructive flaw detection. This thesis is concerned mainly with the study of guided waves in cylinders. A brief literature review is presented next that is related to the theory and numerical modeling of guided waves in cylinders.

1.2 Literature Review

The study of guided waves in cylinders usually falls into two categories. One category corresponds to the analysis of dispersive wave propagation in homogeneous cylinders. The other is the investigation of the waves scattered by inhomogeneities in a cylinder. The dispersion characteristics of guided waves are important for understanding

the properties of wave propagation. Numerical models are usually necessary for the study of wave scattering.

The earliest work related to wave propagation and scattering in cylinders can be found in Miklowitz (1960). The volume edited by Datta *et al.* (1990) contains references on recent developments. However, neither review proposed theoretical solutions or numerical models for finding the wave scattering by flaws in cylindrical structures. A comprehensive literature review by Soldatos (1994), on the other hand, contains many references to the general problems of dynamics and vibration of cylinders and cylindrical shells. In this section, the focus is placed on the study of dispersion relations and numerical modeling.

1.2.1 Guided Waves in Cylinders

The axially symmetric, vibration solution for harmonic waves travelling in an infinitely long homogeneous, isotropic, cylindrical rod was published by Pochhammer (1876) and Chree (1889). The dispersion equation they obtained relates three variables which are, in dimensionless form, Poisson's ratio, the angular frequency, and propagation constants (i.e. the wave number). The dispersion relation satisfies the equations of (elastic) motion and the boundary conditions for a traction-free surface. Because of its complexity, no detailed calculations for the phase and group velocities were reported until 1962 when Onoe *at el.* published numerical results over a wide range of frequencies. Complex wave numbers are used to describe non-propagating and evanescent modes. The real wave numbers, which are only the ones that are physically realizable in an infinitely

long cylinder, correspond to propagating modes. However, the complex wave numbers are needed to satisfy the end conditions of a semi-infinite or a finite cylinder.

A number of approximate theories have appeared for the Pochhammer-Chree problem. See, for example, the survey of Green (1964). Mindlin and Herrmann (1950), as well as Mindlin and McNiven (1960), developed an approximate theory for the analysis of longitudinal waves that included coupling between the longitudinal, radial and axial shear modes. The theory is based on expansions of the displacements in a series of orthogonal polynominals in the radial coordinate. Their results are in very good agreement with the analytical solutions at long wave lengths. McNiven *et al.* (1966a, b) presented a theory for axially symmetric waves that included the first radial mode, as well as the longitudinal and shear modes. This theory can be applied to hollow cylinders having a complete range of thicknesses and it is valid, in the limit, for a solid rod.

Based upon the linear elasticity, the three-dimensional solution of a guided wave in an infinitely long, homogeneous, isotropic hollow cylinder was studied by Gazis (1959) and Armenàkas *et al.* (1969), etc. Their general solution does not need the assumption of axial symmetry. It can be used for estimating the range of applicability of various shell theories.

An analysis becomes more difficult when a cylinder is composed of anisotropic materials. Under the most general form of the constitutive equations, so far there has been no published analytical solutions of guided waves in cylindrical shells. However, analytical solutions are available when simpler materials are considered for many practical applications. McNiven *et al.* (1963) and Armenàkas (1965) studied the propagation of longitudinal and torsional waves, respectively, in an infinitely long,

composite solid rod. The rod is composed of an internal, homogeneous isotropic, solid rod that is perfectly bounded by a coaxial hollow cylinder of a different homogeneous, isotropic material. Moreover, by expressing the radial and axial displacements as a single potential function of the radial coordinate, Keck and Armenàkas (1971) gave an exact solution in an infinitely long composite hollow cylinder having three layers of different, transversely isotropic materials. This procedure can be applied to a laminated isotropic cylinder with many laminae. However, it is a very cumbersome. Rattanawangcharoen and Shah (1992a) presented an analytical and numerical procedure to study the dispersion characteristics of a laminated isotropic cylinder. In this approach, which is based on the three dimensional theory of elasticity, a propagator matrix is formulated that relates the displacement and stresses of one interface to those of another interface. The dispersion relation of the cylinder is established implicitly from the propagator matrix. Numerical evaluations are performed by using Muller's (1956) method with an initial solution taken to as a Rayleigh-Ritz type approximation. Using Frobenius' method, Mirsky (1964, 1966) obtained an exact, infinite power series solution for axisymmetric waves travelling in an infinitely long, orthotropic, solid and hollow cylinder. Based on the same method but somewhat a different solution procedure, Nowinski (1967) obtained an exact, infinite power series solution for a longitudinal wave travelling in a homogeneous orthotropic solid cylinder of infinite extent. Further results on this subject can be found in Chou and Achenbach (1972) and Armenàkas and Reitz (1973).

Due to the complexity of the general problem, many researchers have considered approximate solutions of the dispersion relationship in composite cylinders. Membrane shell theory is one of the approximate theories used to study the vibration and wave

propagation in cylinders. Then, only the normal and shear forces acting in the mid-surface of the shell are considered. The transverse shear forces as well as the bending and twisting moments are assumed to be negligible. As an extension of the Timoshenko beam, there is also a "Timoshenko" shell theory. A list of references for various approximate cylindrical shell theories can be found in the papers by Khdeir *et al.* (1989) and Barbero *et al.* (1990). However, shell theories do not provide sufficiently accurate eigenvalues required for wave scattering problems. Nelson *et al.* (1971) and Huang and Dong (1984) presented a stiffness method to study wave propagation in laminated anisotropic cylinders with an arbitrary number of laminae. In this approach, the thickness of the cylinder is discretized as sublayers. The displacements in each sublayer are evaluated through the use of interpolation functions that involve displacements solely at the interfaces between the sublayers and the middle of each sublayer as the generalized coordinate parameters, i.e. a quadratic interpolation is used. Following a similar numerical procedure, Rattanawangcharoen and Shah (1992b) considered the dispersion relation of laminated composite cylinders. Generally speaking, this approach combines a one-dimensional finite element method with a separation of variables method. Further applications of this approach can be found in, for instance, Xu and Datta (1991), Rattanawangcharoen *et al.* (1994), and Pan *et al.* (1999).

1.2.2 Numerical Modeling

An ultrasonic non-destructive technique relies on information carried by the scattered waves. The theoretical analysis of wave scattering in cylinders is generally quite complicated. However by using a double-integral transform method, combined with the

saddle point method and stationary-phase and group-velocity concepts, an asymptotic analysis based on the exact equations of elasticity has been performed to obtain far-field, head-of-the-pulse information. Such an approach can be found in Davies (1948), Skalak (1957), Folk *et al.* (1958), Jones and Norwood (1967).

An approach based on the approximate equations of motion is an alternative way of studying compressional waves in a rod. Miklowitz (1955) used the Mindlin-Herrmann theory for a rod and considered a step pressure pulse to obtain a formal solution. He (Miklowitz 1957) numerically found the near-field response due to various Poisson ratios and used the stationary-phase method to obtain the far-field response in (Miklowitz 1958). McNiven (1961) considered a three-mode theory to predict the existence of an end resonant frequency. McNiven and Shah (1967) investigated the influence of the end mode on the resonant frequencies of elastic hollow cylinders. Their results showed that hollow cylinders' end resonant frequencies are lower than that of solid rods. High-order (5, 7, 9 mode) approximate theories were used by Zemanek (1972) to study the same problem. The least square method was employed in Gregory and Gladwell (1989) for studying the axisymmetric waves in an infinitely long, elastic rod. The rod is stimulated either by tractions acting over its end face or by a propagating mode reflected at a free end surface. Their work shows that the end resonance frequencies depend strongly on the Poisson ratio.

A wave propagation based, finite element method was employed by Kohl *et al.* (1992) to investigate the effects of dispersion and end conditions on an axially symmetric pulse propagating in a radially inhomogeneous, laminated, semi-infinite cylinder. The boundary conditions were a time varying, uniform axial displacement of the cylinder's

end, together with either zero radial and circumferential displacements or zero shear stresses at the end. Rattanawangcharoen *et al.* (1994) used the wave function expansion method to solve the reflection problem of time-harmonic elastic waves that are incident on the free-edge of a semi-infinite, laminated circular cylinder. Both the least square technique and a variational method were employed to evaluate the unknown complex coefficients and energy fluxes associated with the reflected waves. Numerical results showed that the variational method provided the more accurate results for a laminated anisotropic cylinder. A wave function expansion was used, in conjunction with a finite element method, by Rattanawangcharoen et al. (1997) and Zhuang et al. (1997) to study the axisymmetric guided waves scattered by a jointed, laminated cylinder and by a crack in a welded steel pipe, respectively. In this approach, the cylinder is divided into interior and exterior regions. The interior region contains the welded or jointed region. It is modeled as a finite element region. The exterior region is represented by a wave function expansion. These two regions are connected by the displacement and force continuity conditions at the interfaces of the interior and exterior regions.

In the analysis of wave scattering by cracks, the boundary element method (BEM) is another attractive numerical technique. This method involves discretizing only the boundary of a structure. The governing equation of motion is solved analytically in the boundary's interior. Another advantage of the BEM is that the interior singularity of the stress field is avoided near the crack tip. However, the BEM usually leads to a non-symmetric, non-sparse system of equations, unlike the finite element method (FEM) which produces a symmetric and banded system. Cruse (1988) gave an extensive discussion of modeling techniques associated with the BEM when it is employed to solve

problems involving cracks. Zhuang (1998) used the boundary element method to study the axisymmetric wave scattering by cracks in homogeneous isotropic cylinders.

Several experimental studies concerning the wave reflection and dispersion of a sharp pulse, as well as mode coupling, are worth mentioning. Oliver (1957) was the first to experimentally investigate the free end reflection of an axisymmetric wave travelling in an elastic rod. Fox and Curtis (1958) presented experimental results for longitudinal and bending waves that travel in a rod when the rod is subjected to a step loading. Meitzler (1961) reported the phenomenon of mode coupling in wires that can occur when longitudinal waves propagate at critical frequencies. An experimental study of backward wave transmission in plates and rods was reported by Meitzler (1965). The backward wave happens in certain frequency ranges in which the group and phase velocities have opposite signs. Recently, Alleyne et al. (1998) experimentally and numerically studied wave scattering by circumferential notches in pipes. Their experimental data showed that the reflection coefficient of the incident $L(0,2)$ wave is essentially a linear function of the circumferential extent of the notch whereas the reflection coefficient is a stronger function of the radial depth of the notch.

1.3 Overview of Dissertation

The objective of the present study is to investigate the propagation and scattering of guided waves in cylinders. The dispersion relation of guided waves and Green's function for cylinders are introduced first. Then the wave scattering by a partial circumferential crack in an isotropic and laminated composite cylinder is described.

Finally, wave scattering by an arbitrarily oriented crack in a homogeneous, isotropic cylinder is presented.

1.3.1 Wave Propagation and Green's Functions

The propagator matrix method is used to analyze the dispersion relation of guided waves in a laminated homogeneous, isotropic cylinder. However, a one dimensional finite element method is employed in the radial direction for a laminated composite cylinder. In either case, a dispersion relation is obtained for each circumferential wave number.

The Green's function is obtained through either an integral transform or symmetry and anti-symmetry arguments. It can be expressed as a wave function expansion with summations involving both the circumferential and axial wave numbers. Because of the divergence of the Fourier series representation of a (singular) delta function, a pulse having a uniform intensity over a narrow circumferential distance is used to simulate the delta function. Each Fourier component represents a harmonic, ring-like load that corresponds to a particular circumferential wave number.

1.3.2 Wave Scattering by a Circumferential Crack

A novel numerical procedure is presented first for studying wave scattering by a circumferential crack in a steel pipe. The incident wave field is assumed to be one of the propagating modes generated at infinity. By employing a wave function expansion in the axial direction and by decomposing the problem into symmetric and anti-symmetric sub-problems, three-dimensional wave scattering is reduced to two simpler problems. By

employing a transfer matrix method from one radius to another radius, the two sub-problems are reduced further to two, quasi-one-dimensional problems. This simplification greatly reduces the computational time. The numerical procedure is studied initially for an isotropic cylinder. However, by replacing the exact wave function with an approximate one, the procedure can also be used to solve wave scattering by a crack in a laminated composite cylinder.

1.3.3 General Wave Scattering by Cracks

The Green's functions are used in the boundary element method to study wave scattering in cylinders. Here, the incident wave field is formed by a point load. In this study, a multi-domain technique is used, as well as an efficient numerical procedure, for evaluating the Cauchy principal value integrals and weakly singular integrals (Zhu, et al. 1996 and Zhu and Shah 1997).

1.4 Dissertation's Structure

This thesis is concerned mainly with the investigating the propagation and scattering of guided waves in cylinders. A literature review is presented in Chapter 1. An analytical formulation and an approximate model are given in Chapter 2 to determine the dispersion relations and to evaluate the Green's functions. Symmetric and anti-symmetric arguments are employed in Chapter 3 to analyze the three-dimensional wave scattering arising from a circumferential crack in an isotropic cylinder as well as a laminated composite cylinder. The boundary element method is used in Chapter 4 to study the

three-dimensional wave scattering by an arbitrarily oriented crack in an isotropic cylinder. Finally, conclusions and recommendations for further study are outlined in Chapter 5.

Chapter 2

Wave Modes and Green's Functions of a Cylinder

The study and understanding of wave phenomena in a cylindrical structure is important for an ultrasonic inspection to detect flaws. A brief review of the wave modes and Green's functions of a cylinder is given in this chapter together with numerical data. Two types of frequently used incident fields, namely a single wave mode and a point load, i.e. Green's function, are discussed. The single wave incidence mode will be used in the hybrid method described in Chapter 3. On the other hand, a point load input will be employed in Chapter 4 when dealing with the boundary element method.

There are many analytical and numerical results reported for wave modes in a circular cylinder. The wave modes of a circular cylinder, expressed as functions of Bessel's functions, have been given in Gazis (1959) and in Rattanawangcharoen and Shah (1992a), for example. Zhuang et al. (1999) detailed the Green's functions of a laminated composite cylinder by using a transform method and conditions of symmetry and anti-symmetry. Further information can be found in these references.

2.1 Wave Modes of Laminated Isotropic Cylinders

The time harmonic wave considered in this chapter is assumed to propagate along the cylinder's axial or z-direction. The circular cylinder is considered to be infinitely long and to be composed of perfectly bonded, isotropic elastic layers. The layers may have different mechanical properties and thicknesses. The cylindrical coordinates (r, θ, z), whose origin is located at the centre of the cylinder's cross-section, is used here with $\mathbf{e}_r$, $\mathbf{e}_\theta$ and $\mathbf{e}_z$ as the corresponding base vectors. See Figure 2.1(a). The harmonic time factor $e^{-i\omega t}$, where ω is the circular frequency, is suppressed in the sequel.

2.1.1 Basic Relations for Homogeneous Isotropic Cylinders

In a cylindrical coordinate system, the strain-displacement relation is given by,

$$\boldsymbol{\varepsilon} = \mathbf{P}_r \frac{\partial \mathbf{u}}{\partial r} + \frac{1}{r}\mathbf{P}_\theta \frac{\partial \mathbf{u}}{\partial \theta} + \mathbf{P}_z \frac{\partial \mathbf{u}}{\partial z} + \frac{1}{r}\mathbf{P}_0 \mathbf{u} \tag{2.1}$$

where

$$\boldsymbol{\varepsilon} = \left\{ \varepsilon_{rr},\ \varepsilon_{\theta\theta},\ \varepsilon_{zz},\ \gamma_{\theta z},\ \gamma_{zr},\ \gamma_{r\theta} \right\}^T \tag{2.2}$$

$$\mathbf{u} = \left\{ u_r,\ u_\theta,\ u_z \right\}^T \tag{2.3}$$

and

$$\mathbf{P}_r = \left[\mathbf{e}_1, \mathbf{e}_6, \mathbf{e}_5 \right],\quad \mathbf{P}_\theta = \left[\mathbf{e}_6, \mathbf{e}_2, \mathbf{e}_4 \right],\quad \mathbf{P}_z = \left[\mathbf{e}_5, \mathbf{e}_4, \mathbf{e}_3 \right],\quad \mathbf{P}_0 = \left[\mathbf{e}_2, -\mathbf{e}_6, \mathbf{0} \right]. \tag{2.4}$$

The $\mathbf{e}_i$ (i = *1, 2, ..., 6*) are the fundamental unit column vectors in $\mathbf{R}^6$; $\mathbf{P}_r$, $\mathbf{P}_\theta$, $\mathbf{P}_z$ and $\mathbf{P}_0$ are six by three real matrices and superscript T represents the transpose. The stress-strain relation, on the other hand, is given generally by,

$$\boldsymbol{\sigma} = \mathbf{D}\boldsymbol{\varepsilon} \tag{2.5}$$

where

$$\boldsymbol{\sigma} = \left\{\sigma_{rr},\ \sigma_{\theta\theta},\ \sigma_{zz},\ \sigma_{\theta z},\ \sigma_{zr},\ \sigma_{r\theta}\right\}^T \tag{2.6}$$

and

$$\mathbf{D} = \begin{bmatrix} \lambda+2\mu & \lambda & \lambda & & & \\ \lambda & \lambda+2\mu & \lambda & & & \\ \lambda & \lambda & \lambda+2\mu & & & \\ & & & \mu & & \\ & & & & \mu & \\ & & & & & \mu \end{bmatrix}. \tag{2.7}$$

Here λ and μ are Lame's constants.

The equations of harmonic motion can be expressed, in the frequency domain, in terms of the displacement components u_r, u_θ and u_z as,

$$\begin{aligned} &\mu\left(\nabla^2 u_r - \frac{2}{r^2}\frac{\partial u_\theta}{\partial\theta} - \frac{u_r}{r^2}\right) + (\lambda+\mu)\frac{\partial\Delta}{\partial r} + f_r = -\rho\omega^2 u_r \\ &\mu\left(\nabla^2 u_\theta + \frac{2}{r^2}\frac{\partial u_\theta}{\partial\theta} - \frac{u_\theta}{r^2}\right) + (\lambda+\mu)\frac{\partial\Delta}{r\partial\theta} + f_\theta = -\rho\omega^2 u_\theta \\ &\mu\nabla^2 u_z + (\lambda+\mu)\frac{\partial\Delta}{\partial z} + f_z = -\rho\omega^2 u_z \end{aligned} \tag{2.8}$$

where

$$\Delta = \frac{\partial u_r}{\partial r} + \frac{u_r}{r} + \frac{\partial u_\theta}{r\partial\theta} + \frac{\partial u_z}{\partial z}. \tag{2.9}$$

The f_r, f_θ and f_z are the body force (per unit volume) components in the r, θ and z directions, respectively, and ρ is the mass density. The traction-free boundary conditions are given by,

$$\sigma_{rr} = 0, \quad \sigma_{r\theta} = 0, \quad \sigma_{rz} = 0, \quad \text{at } r = R_{inner} \text{ and } r = R_{outer} \tag{2.10}$$

where R_{inner} and R_{outer} is the inner and outer radius of the cylinder, respectively.

The solution of equation (2.8) is given by,

$$\begin{aligned} u_r &= \left[f' - \xi h_r + \frac{im}{r} h_z \right] e^{i(m\theta+\xi z)} \\ u_\theta &= \left[\frac{im}{r} f + i\xi h_r - h_z' \right] e^{i(m\theta+\xi z)} \\ u_z &= \left[i\xi f - i\left(h_r' + \frac{m+1}{r} h_r \right) \right] e^{i(m\theta+\xi z)} \end{aligned} \tag{2.11}$$

where

$$\begin{aligned} f(r) &= A_1 Z_m(\alpha r) + B_1 W_m(\alpha r) \\ h_r(r) &= A_2 Z_{m+1}(\beta r) + B_2 W_{m+1}(\beta r) \\ h_z(r) &= A_3 Z_m(\beta r) + B_3 W_m(\beta r) \end{aligned} \tag{2.12}$$

while

$$\alpha^2 = \omega^2/c_1^2 - \xi^2, \ \beta^2 = \omega^2/c_2^2 - \xi^2 \tag{2.13}$$

$$m = 0,1,2,\ldots \ . \tag{2.14}$$

A prime superscript in equation (2.11) denotes differentiation with respect to r, m is the circumferential wave number, t represents time, ξ is the wave number in the z direction, and $i = \sqrt{-1}$. Z_m and W_m in equation (2.12) are the Hankel functions $H_m^{(1)}$ and $H_m^{(2)}$, respectively. The A_1, A_2, A_3, B_1, B_2 and B_3 are unknown constants. The speeds of the dilatational and torsional (shear) waves, c_1 and c_2, are defined as,

$$c_1^2 = \frac{\lambda + 2\mu}{\rho} \ \text{ and } \ c_2^2 = \frac{\mu}{\rho}. \tag{2.15}$$

For the special case of a solid cylinder, function Z_m in equation (2.12) is taken as J_m, the Bessel function of the first kind, and $B_i = 0$.

The stress components are given generally by,

$$\sigma_{rr} = \mu\left[-\frac{2}{r}f' + \left(\xi^2 - \beta^2 + \frac{2m^2}{r^2}\right)f - 2\xi h_r' + 2\frac{im}{r}\left(h_z' - \frac{1}{r}h_z\right)\right] \tag{2.16}$$

$$\sigma_{\theta\theta} = \mu\left[\frac{2}{r}f' + \left(\xi^2 + \beta^2 + \frac{2m^2}{r^2}\right)f - 2\frac{(m+1)\xi}{r}h_r - 2\frac{im}{r}\left(h_z' - \frac{1}{r}h_z\right)\right] \tag{2.17}$$

$$\sigma_{zz} = \mu\left[\left(2\alpha^2 - \xi^2 - \beta^2\right)f + 2\xi\left(h_r' + \frac{m+1}{r}h_r\right)\right] \tag{2.18}$$

$$\sigma_{\theta z} = \mu\left[-2\frac{m\xi}{r}f + \frac{m}{r}h_r' + \left(\frac{m^2+m}{r^2} - \xi^2\right)h_r - i\xi h_z'\right] \tag{2.19}$$

$$\sigma_{zr} = \mu\left[2i\xi f' - \frac{im}{r}h' - i\left(\xi^2 - \beta^2 + \frac{m^2+m}{r^2}\right)h_r - \frac{m\xi}{r}h_z\right] \tag{2.20}$$

and

$$\sigma_{r\theta} = \mu\left[2\frac{im}{r}\left(f' - \frac{1}{r}f\right) + i\xi\left(h_r' - \frac{m+1}{r}h_r\right) + \frac{2}{r}h_z' + \left(\beta^2 - \frac{2m^2}{r^2}\right)h_z\right] \tag{2.21}$$

where the common factor $e^{i(m\theta+\xi z)}$ is omitted for convenience.

2.1.2 Propagator Matrix Approach

The previous results only pertain strictly to isotropic, homogeneous cylinders. When a laminated isotropic cylinder is considered, however, a propagator matrix approach can be used that employs the results in the following manner. First, the thickness of the cylinder, H, is discretized into N sublayers to model the radial inhomogeneity. See Figure 2.1(b). Consider the k^{th} layer, for example, which is bounded by the $r = R_k$ and $r = R_{k+1}$ surfaces. By using equations (2.11), (2.16), (2.21) and (2.20), the displacement and stress components at the interface $r = R_k$ can be expressed as

$$\begin{Bmatrix} \mathbf{U}_k \\ \mathbf{S}_k \end{Bmatrix} = \mathbf{Q}_k \begin{Bmatrix} \mathbf{A} \\ \mathbf{B} \end{Bmatrix} \tag{2.22}$$

with

$$\mathbf{U}_k = \begin{pmatrix} u_{rk} & u_{\theta k} & u_{zk} \end{pmatrix}^T, \ \mathbf{S}_k = \begin{pmatrix} \sigma_{rrk} & \sigma_{r\theta k} & \sigma_{rzk} \end{pmatrix}^T \tag{2.23}$$

and

$$\mathbf{A} = \begin{pmatrix} A_1 & A_2 & A_3 \end{pmatrix}^T, \ \mathbf{B} = \begin{pmatrix} B_1 & B_2 & B_3 \end{pmatrix}^T. \tag{2.24}$$

Subscript k indicates the nodal values at the k^{th} interface. By repeating the above procedure at the surface $r = R_{k+1}$ and using equation (2.22), the following relation is achieved

$$\begin{Bmatrix} \mathbf{U}_{k+1} \\ \mathbf{S}_{k+1} \end{Bmatrix} = \mathbf{P}_k \begin{Bmatrix} \mathbf{U}_k \\ \mathbf{S}_k \end{Bmatrix}, \quad 1 \le k \le N \tag{2.25}$$

with

$$\mathbf{P}_k = \mathbf{Q}_{k+1} \mathbf{Q}_k^{-1}. \tag{2.26}$$

The six by six matrix $\mathbf{P}_k$ is called the propagator matrix for the k^{th} layer. The specific form of matrix $\mathbf{Q}_k$ is given in Appendix A. (Also see Rattanawangcharoen and Shah, 1992a.) Once the wave number, ξ, is known for the given frequency, ω, or vice versa, equation (2.25) can be used to evaluate the displacements and stresses at each sublayer.

Special consideration has to be given to the innermost core for a solid cylinder. In order to have a bounded solution in the region $0 \le r \le R_{outer}$, the function Z_m in equation (2.12) is taken as J_m, the Bessel function of the first kind, and $B_i = 0$. The displacement and stress components at the interface $r = R_1$ satisfy the relation,

$$\mathbf{S}_1 = \mathbf{K}\mathbf{U}_1. \tag{2.27}$$

When the wave number, ξ, and displacement components, $\mathbf{U}_l$, are known, equations (2.25) and (2.27) can be used to calculate the displacement and stress components at each interface. Details of matrix $\mathbf{K}$ can be found in Rattanawangcharoen and Shah (1992). They are reproduced in Appendix A for convenience.

By repeatedly applying relation (2.25) in each successive sublayer of the hollow cylinder, the displacement and stress relation between the outer and inner surfaces can be found to be,

$$\begin{Bmatrix} \mathbf{U}_{N+1} \\ \mathbf{S}_{N+1} \end{Bmatrix} = \mathbf{P} \begin{Bmatrix} \mathbf{U}_1 \\ \mathbf{S}_1 \end{Bmatrix} \tag{2.28}$$

with

$$\mathbf{P} = \prod_{k=1}^{N} \mathbf{P}_{N+1-k} = \begin{bmatrix} \mathbf{P}_{11} & \mathbf{P}_{12} \\ \mathbf{P}_{21} & \mathbf{P}_{22} \end{bmatrix}. \tag{2.29}$$

Then the dispersion equation for a hollow cylinder is given by,

$$\det\left(\mathbf{P}_{21}\right) = 0. \tag{2.30}$$

On the other hand, the last formulation has to be combined with equation (2.27) for the final sublayer of the solid cylinder so that the corresponding dispersion relation takes the form,

$$\det\left(\mathbf{P}_{21} + \mathbf{K}\mathbf{P}_{22}\right) = 0. \tag{2.31}$$

In deriving equations (2.30) and (2.31), the traction-free boundary condition (2.10) is applied. The $\mathbf{P}$ in equation (2.29) is a six by six, complex matrix whereas the $\mathbf{P}_{ij}$, $i, j = 1, 2$, in equation (2.29) are three by three complex matrices.

2.2 Wave Modes of Composite Cylinders

Laminated composite cylinders possess general anisotropy so that the corresponding wave modes cannot be determined analytically. However, semi-analytical finite element method - the Rayleigh-Ritz-type approximation (Huang and Dong, 1984) - may be used to determine the wave modes. In this method, only the radial dependence is modeled by the one dimensional finite element procedure.

The displacement components, u_r, u_θ, and u_z, of the k^{th} layer (see, for example, Figure 2.1(b)), which is bounded by R_k and R_{k+1}, are approximated by interpolation polynomials in the radial direction as,

$$\mathbf{u}(r,\ \theta,\ z) = \mathbf{N}(\eta)\mathbf{q}(\theta,\ z) \tag{2.32}$$

with

$$r = n_1(\eta)R_k + n_2(\eta)R_m + n_3(\eta)R_{k+1} \tag{2.33}$$

$$\mathbf{N}(\eta) = \begin{bmatrix} n_1 & 0 & 0 & n_2 & 0 & 0 & n_3 & 0 & 0 \\ 0 & n_1 & 0 & 0 & n_2 & 0 & 0 & n_3 & 0 \\ 0 & 0 & n_1 & 0 & 0 & n_2 & 0 & 0 & n_3 \end{bmatrix} \tag{2.34}$$

and

$$\mathbf{q}(\theta, z) = \{u_{r1},\ u_{\theta 1},\ u_{z1},\ u_{r2},\ u_{\theta 2},\ u_{z2},\ u_{r3},\ u_{\theta 3},\ u_{z3}\}^T. \tag{2.35}$$

In equation (2.32), the nodal displacements u_{rj}, $u_{\theta j}$, and u_{zj}, $j = 1, 2, 3$, are taken at the $r = R_k$, $r = R_m = (R_k+R_{k+1})/2$, and $r = R_{k+1}$ surfaces. The interpolation polynomials, n_i, are quadratic functions given by,

$$n_1(\eta) = \tfrac{1}{2}\left(\eta^2 - \eta\right),\quad n_2(\eta) = 1 - \eta^2,\quad n_3(\eta) = \tfrac{1}{2}\left(\eta^2 + \eta\right),\ -1 \le \eta \le 1. \tag{2.36}$$

It can be shown from equations (2.33) and (2.36) that,

$$r = \frac{1-\eta}{2} R_k + \frac{1+\eta}{2} R_{k+1}, \quad -1 \le \eta \le 1 \tag{2.37}$$

and

$$\eta = \frac{2r - R_k - R_{k+1}}{R_{k+1} - R_k}, \quad R_k \le r \le R_{k+1}. \tag{2.38}$$

The general relation between the stress and strain components in a typical sublayer is,

$$\boldsymbol{\sigma} = \mathbf{D}\,\boldsymbol{\varepsilon} \tag{2.39}$$

where $\mathbf{D}$ is a 6 by 6 matrix of anisotropic elastic moduli for which the unique axis coincides with the z-axis. The $\boldsymbol{\sigma}$ and $\boldsymbol{\varepsilon}$ are stress and strain vectors defined in equations (2.6) and (2.2), respectively. Substituting equation (2.32) into equation (2.1) gives the strain vector as,

$$\boldsymbol{\varepsilon} = \mathbf{B}_r \mathbf{U} + \mathbf{B}_\theta \frac{\partial \mathbf{U}}{\partial \theta} + \mathbf{B}_z \frac{\partial \mathbf{U}}{\partial z} \tag{2.40}$$

where

$$\mathbf{B}_r = \mathbf{P}_r \frac{d\mathbf{N}(\eta)}{dr} + \mathbf{P}_0, \quad \mathbf{B}_\theta = \frac{1}{r}\mathbf{P}_\theta \mathbf{N}(\eta), \quad \mathbf{B}_z = \mathbf{P}_z \mathbf{N}(\eta). \tag{2.41}$$

Combining equations (2.39) and (2.40) gives the stress vector in the global coordinate system as,

$$\boldsymbol{\sigma} = \mathbf{D}_r \mathbf{U} + \mathbf{D}_\theta \frac{\partial \mathbf{U}}{\partial \theta} + \mathbf{D}_z \frac{\partial \mathbf{U}}{\partial z} \tag{2.42}$$

where the stress-transformation matrices, $\mathbf{D}_i$ ($i = r, \theta, z$), are defined by,

$$\mathbf{D}_i = \mathbf{D}\mathbf{B}_i, \quad i = r, \theta, z\,. \tag{2.43}$$

Hamilton's principle is used next in the form,

$$\overline{\delta} \int_{t_1}^{t_2} (T - V)\, dt = 0 \tag{2.44}$$

where $\overline{\delta}$ is the first variation. T and V, on the other hand, are respectively the kinetic and (total) potential energy that are given by,

$$T = \frac{1}{2}\omega^2 \int_{\text{vol}} \rho \mathbf{u}^T \mathbf{u}\, d\text{vol} \text{ and } V = \frac{1}{2}\int_{\text{vol}} \boldsymbol{\varepsilon}^T \mathbf{D}\boldsymbol{\varepsilon}\, d\text{vol}. \tag{2.45}$$

Then the governing equation in the frequency domain is formulated conventionally for the entire cylinder. It takes the form,

$$\mathbf{K}_{rr}\mathbf{Q} + \mathbf{K}_{\theta}\mathbf{Q}_{,\theta} + \mathbf{K}_{z}\mathbf{Q}_{,z} - \mathbf{K}_{\theta\theta}\mathbf{Q}_{,\theta\theta} - \mathbf{K}_{z\theta}\mathbf{Q}_{,z\theta} - \mathbf{K}_{zz}\mathbf{Q}_{,zz} - \omega^2\mathbf{M}\mathbf{Q} = 0 \tag{2.46}$$

where $\mathbf{Q}_{,\theta} = \dfrac{\partial \mathbf{Q}}{\partial \theta}$ and $\mathbf{Q}_{,z} = \dfrac{\partial \mathbf{Q}}{\partial z}$. The $\mathbf{K}_{rr}$, $\mathbf{K}_{\theta\theta}$, $\mathbf{K}_{z\theta}$, $\mathbf{K}_{zz}$ and $\mathbf{M}$ are real, symmetric matrices but $\mathbf{K}_z$ and $\mathbf{K}_\theta$ are real, anti-symmetric matrices. They are given by,

$$\mathbf{M} = 2\pi \int_{R_i}^{R_o} \rho \mathbf{N}^T \mathbf{N} r dr \tag{2.47}$$

$$\mathbf{K}_{ii} = 2\pi \int_{R_i}^{R_o} \mathbf{B}_i^T \mathbf{D}\mathbf{B}_i r dr, \quad i = r, \theta, z \tag{2.48}$$

$$\mathbf{K}_{\theta z} = 2\pi \int_{R_i}^{R_o} \left(\mathbf{B}_\theta^T \mathbf{D}\mathbf{B}_z + \mathbf{B}_z^T \mathbf{D}\mathbf{B}_\theta\right) r dr \tag{2.49}$$

and

$$\mathbf{K}_j = 2\pi \int_{R_i}^{R_o} \left(\mathbf{B}_r^T \mathbf{D}\mathbf{B}_j - \mathbf{B}_j^T \mathbf{D}\mathbf{B}_r\right) r dr, \quad j = \theta, z. \tag{2.50}$$

Vector $\mathbf{Q}$ in equation (2.46) contains the nodal displacements along one radius of the cylinder.

A solution of equation (2.46) that represents harmonic wave propagation can be assumed to take the form,

$$\mathbf{Q}(\theta, z) = \mathbf{Q}_0 e^{i(m\theta + \xi z)} \tag{2.51}$$

where $\mathbf{Q}_0$ represents the nodal amplitude vector, ξ is the wave number in the z- direction, m is the circumferential wave number, and ω is the circular frequency. Substituting equation (2.51) into equation (2.46) results in the set of linear homogeneous equations,

$$\left(-\xi^2\mathbf{K}_0 + i\xi\mathbf{K}_1 - \mathbf{K}_2\right)\mathbf{Q}_0 + \omega^2\mathbf{M}\mathbf{Q}_0 = 0 \tag{2.52}$$

where

$$\mathbf{K}_0 = \mathbf{K}_{zz}, \quad \mathbf{K}_1 = im\mathbf{K}_{z\theta} - \mathbf{K}_z, \quad \mathbf{K}_2 = m^2\mathbf{K}_{\theta\theta} + im\mathbf{K}_\theta + \mathbf{K}_{rr}. \tag{2.53}$$

For a given frequency, ω, the quadratic algebraic eigenvalue problem (2.52) can be rearranged as,

$$\begin{bmatrix} \mathbf{0} & \mathbf{I} \\ \omega^2\mathbf{M} - \mathbf{K}_2 & i\mathbf{K}_1 \end{bmatrix} \begin{Bmatrix} \mathbf{Q}_0 \\ \xi\mathbf{Q}_0 \end{Bmatrix} = \xi \begin{bmatrix} \mathbf{I} & \mathbf{0} \\ \mathbf{0} & \mathbf{K}_0 \end{bmatrix} \begin{Bmatrix} \mathbf{Q}_0 \\ \xi\mathbf{Q}_0 \end{Bmatrix}. \tag{2.54}$$

The eigenvalues of the general eigenvalue problem (2.54) are the wave numbers, ξ. The upper half of the eigenvectors corresponds to the wave function, $\mathbf{Q}_0$. Equation (2.54) serves as the dispersion relation for an anisotropic cylinder. The eigenvalues of equation (2.54) are used as the initial approximations when solving equation (2.31) for an isotropic cylinder by using Muller's method (Muller, 1956).

2.3 Green's Functions for Cylinders

The elastodynamic Green's function for laminated, anisotropic, circular cylinders has been studied numerically by Zhuang (1998) and Zhuang *et al.* (1999) using integral transform and modal summation methods. As these two methods give equivalent numerical results and the Green's functions obtained from the transform method are used later, only a brief discussion of the transform method is given next.

Equation (2.46) is derived for no body force. When the Green's functions are involved so that a point load (i.e. a body force) is needed, this equation should be modified accordingly. Assume that the time harmonic, unit magnitude, concentrated load has the form,

$$\begin{aligned}\mathbf{f}(r,\theta,z,t) &= \boldsymbol{\alpha}_f \frac{1}{r}\delta(r-r_b)\delta(\theta)\delta(z)e^{-i\omega t} \\ &= \boldsymbol{\alpha}_f \frac{1}{r_b}\delta(r-r_b)\delta(\theta)\delta(z)e^{-i\omega t}\end{aligned} \tag{2.55}$$

where $\delta(*)$ is the Dirac delta function and

$$\boldsymbol{\alpha}_f = \alpha_r \mathbf{e}_r + \alpha_\theta \mathbf{e}_\theta + \alpha_z \mathbf{e}_z, \quad \left\|\boldsymbol{\alpha}_f\right\| = 1 \tag{2.56}$$

is the direction cosine of the load whilst $\|\bullet\|$ denotes the length of a vector.

As stated earlier, the cylinder's thickness is discretized into N sublayers. Therefore, there are $(2N+1)$ nodes in the radial direction. Let r_b coincide with a finite element node point, Assume that the node number corresponding to r_b is n_b. Then the spatial representation of the body force (in the finite element sense where the consistent force formulation is used in the computation – see, for example, Bathe (1982)), takes the form,

$$\mathbf{F}(\theta,z,t) = \mathbf{F}_b \frac{1}{r_b}\delta(\theta)\delta(z)e^{-i\omega t} \tag{2.57}$$

where

$$\mathbf{F}_b = \left\{\alpha_r \mathbf{e}_{n_b}^T, \alpha_\theta \mathbf{e}_{n_b}^T, \alpha_z \mathbf{e}_{n_b}^T\right\}^T \in \mathbf{R}^{N_m \times 1}, \quad N_m = 3(2N+1) \tag{2.58}$$

is the radially distributed force vector. The $\mathbf{e}_{n_b}$ is the fundamental unit vector in $\mathbf{R}^{2N+1}$. Then equation (2.46) may be rewritten as,

$$\mathbf{K}_{rr}\mathbf{Q}+\mathbf{K}_{\theta}\mathbf{Q}_{,\theta}+\mathbf{K}_{z}\mathbf{Q}_{,z}-\mathbf{K}_{\theta\theta}\mathbf{Q}_{,\theta\theta}-\mathbf{K}_{z\theta}\mathbf{Q}_{,z\theta}-\mathbf{K}_{zz}\mathbf{Q}_{,zz}-\omega^{2}\mathbf{M}\mathbf{Q}=\frac{1}{r_b}\mathbf{F}_b\delta(\theta)\delta(z). \quad (2.59)$$

Because of the non-convergence of the Fourier series representation of $\delta(\theta)$, it is approximated here as an impulse that has a uniform intensity in the circumferential direction between $-\hat{\theta}_0 \le \theta \le \hat{\theta}_0$. Thus, $\delta(\theta)$ is approximated as $\hat{\delta}(\theta)$ where,

$$\hat{\delta}(\theta)=\begin{cases}1/(2\hat{\theta}_0), & -\hat{\theta}_0 \le \theta \le \hat{\theta}_0\\ 0, & \text{otherwise.}\end{cases} \quad (2.60)$$

The Fourier series of function $\hat{\delta}(\theta)$ is given as,

$$\hat{\delta}(\theta)\approx\sum_{m=-M}^{M} s_m e^{im\theta} \quad (2.61)$$

where

$$s_0=\frac{1}{2\pi}, \quad s_m=\frac{1}{2\pi}\frac{\sin(m\hat{\theta}_0)}{m\hat{\theta}_0}, \quad m=\pm1,\pm2,\ldots. \quad (2.62)$$

Therefore, the solution of equation (2.59) can be expressed as a Fourier series of the variable θ so that,

$$\mathbf{Q}(\theta,z)=\sum_{m=-M}^{M}\mathbf{Q}_m(z)e^{im\theta}. \quad (2.63)$$

Substituting equations (2.61) and (2.63) into equation (2.59) yields the following system of ordinary differential equation of the Fourier coefficients, $\mathbf{Q}_m(z)$, m = 0, ±1, ±2, …, ±∞,

$$(\mathbf{K}_2-\omega^{2}\mathbf{M})\mathbf{Q}_m-\mathbf{K}_1\mathbf{Q}_{m,z}-\mathbf{K}_{zz}\mathbf{Q}_{m,zz}=\frac{s_m}{r_b}\mathbf{F}_b\delta(z). \quad (2.64)$$

The matrices $\mathbf{K}_0$, $\mathbf{K}_1$ and $\mathbf{K}_2$ are defined in equation (2.53). The Fourier integral transform (Sneddon, 1951) is used for the z-dependent quantities, $\mathbf{Q}_m(z)$. It is given by,

$$\tilde{f}(k_m)=\frac{1}{\sqrt{2\pi}}\int_{-\infty}^{+\infty} f(z)e^{ik_m z}dz, \quad f(z)=\frac{1}{\sqrt{2\pi}}\int_{-\infty}^{+\infty}\tilde{f}(k_m)e^{-ik_m z}dk_m \tag{2.65}$$

where k_m is the transform parameter. Applying the transform to equation (2.64) gives,

$$\left[\left(\mathbf{K}_2-\omega^2\mathbf{M}\right)-ik\mathbf{K}_1+k^2\mathbf{K}_{zz}\right]\tilde{\mathbf{Q}}_m=\frac{1}{\sqrt{2\pi}}\frac{s_m}{r_b}\mathbf{F}_b. \tag{2.66}$$

The quadratic equation (2.66) can be recast into a first order form (as done already in equation (2.54)) so that,

$$\mathbf{A}\mathbf{x}=k\mathbf{B}\mathbf{x}+\tilde{\mathbf{F}}_m \tag{2.67}$$

where

$$\mathbf{A}=\begin{bmatrix}\mathbf{0} & \mathbf{I}\\ \omega^2\mathbf{M}-\mathbf{K}_2 & i\mathbf{K}_1\end{bmatrix}, \quad \mathbf{B}=\begin{bmatrix}\mathbf{I} & \mathbf{0}\\ \mathbf{0} & \mathbf{K}_0\end{bmatrix}, \quad \mathbf{x}=\begin{Bmatrix}\tilde{\mathbf{Q}}_m\\ k\tilde{\mathbf{Q}}_m\end{Bmatrix}, \quad \overline{\mathbf{F}}_m=\begin{Bmatrix}\mathbf{0}\\ \mathbf{F}_m\end{Bmatrix} \tag{2.68}$$

and

$$\mathbf{F}_m=\frac{1}{\sqrt{2\pi}}\frac{s_m}{r_b}\mathbf{F}_b. \tag{2.69}$$

Equation (2.67) corresponds to a forced motion. Its solution can be represented by a modal expansion of the corresponding homogeneous system (2.54). For a given circular frequency, ω, and a specified circumferential wave number m, the eigenvalues of the general eigenvalue problem (2.54) are k_{mn} (n = 1, 2, …, $2N_m$). N_m is the length of vector $\mathbf{F}_b$. (See equation (2.58).) The corresponding left and right eigenvectors are,

$$\boldsymbol{\varphi}_{mn}^{L}=\begin{Bmatrix}\boldsymbol{\varphi}_{mn,u}^{L}\\ \boldsymbol{\varphi}_{mn,l}^{L}\end{Bmatrix}, \quad \boldsymbol{\varphi}_{mn}^{R}=\begin{Bmatrix}\boldsymbol{\varphi}_{mn,u}^{R}\\ \boldsymbol{\varphi}_{mn,l}^{R}\end{Bmatrix}. \tag{2.70}$$

Superscripts L and R in the above relationships represent the left and right eigenvectors, respectively. Subscripts l and u, on the other hand, stand for the lower half and upper half

of the eigenvector, respectively. The bi-orthogonality relations of the right and left eigenvectors are,

$$\left(\boldsymbol{\varphi}_{mn}^{L}\right)^{T}\mathbf{A}\boldsymbol{\varphi}_{mp}^{R}=k_{mn}B_{mn}\delta_{np},\quad \left(\boldsymbol{\varphi}_{mn}^{L}\right)^{T}\mathbf{B}\boldsymbol{\varphi}_{mp}^{R}=B_{mn}\delta_{np},\quad n,p=1,2,...,2N_{m} \tag{2.71}$$

and

$$B_{mn}=\left(\boldsymbol{\varphi}_{mn}^{L}\right)^{T}\mathbf{B}\boldsymbol{\varphi}_{mn}^{R}=\left(\boldsymbol{\varphi}_{mn,u}^{L}\right)^{T}\boldsymbol{\varphi}_{mn,u}^{R}-\left(\boldsymbol{\varphi}_{mn,l}^{L}\right)^{T}\mathbf{K}_{0}\boldsymbol{\varphi}_{mn,u}^{R},\quad n=1,2,...,2N_{m}. \tag{2.72}$$

Note that there is no summation for the indices m or n in equations (2.71) and (2.72). Thus, the solution of equation (2.67) is given by a modal expansion as,

$$\mathbf{x}=\sum_{n=1}^{2N_{m}}x_{n}\boldsymbol{\varphi}_{mn}^{R}. \tag{2.73}$$

The coefficient x_n is determined by using the bi-orthogonality relation (2.71). It is given as (see equations (2.68) and (2.69)),

$$x_{n}=\frac{\left(\boldsymbol{\varphi}_{mn}^{L}\right)^{T}\bar{\mathbf{F}}_{m}}{\left(k_{mn}-k\right)B_{mn}}=\frac{\left(\boldsymbol{\varphi}_{mn,l}^{L}\right)^{T}\mathbf{F}_{m}}{\left(k_{mn}-k\right)B_{mn}}=\frac{1}{\sqrt{2\pi}}\frac{s_{m}}{r_{b}}\frac{\left(\boldsymbol{\varphi}_{mn,l}^{L}\right)^{T}\mathbf{F}_{b}}{\left(k_{mn}-k\right)B_{mn}}. \tag{2.74}$$

Hence, the transformed solution, $\tilde{\mathbf{Q}}_m$, $-\infty \le m \le \infty$, which is the upper half of the solved vector **x**, has the form,

$$\tilde{\mathbf{Q}}_{m}=\sum_{n=1}^{2N_{m}}x_{n}\boldsymbol{\varphi}_{mn,u}^{R}=\frac{1}{\sqrt{2\pi}}\frac{s_{m}}{r_{b}}\sum_{n=1}^{2N_{m}}\frac{\left(\boldsymbol{\varphi}_{mn,l}^{L}\right)^{T}\mathbf{F}_{b}}{\left(k_{mn}-k\right)B_{mn}}\boldsymbol{\varphi}_{mn,u}^{R}. \tag{2.75}$$

The Fourier coefficient $\mathbf{Q}_m(z)$ is derived from equation (2.75) by employing the inverse Fourier integral transform. It is given by,

$$\mathbf{Q}_{m}(z)=\frac{1}{\sqrt{2\pi}}\int_{-\infty}^{\infty}\tilde{\mathbf{Q}}_{m}e^{-ikz}dk=\frac{s_{m}}{2\pi r_{b}}\sum_{n=1}^{2N_{m}}\int_{-\infty}^{\infty}\frac{\left(\boldsymbol{\varphi}_{mn,l}^{L}\right)^{T}\mathbf{F}_{b}}{\left(k_{mn}-k\right)B_{mn}}\boldsymbol{\varphi}_{mn,u}^{R}e^{ikz}dk. \tag{2.76}$$

Before applying the Cauchy residue theorem (Mitrinovic and Keckic, 1984) to the last equation, it should be noted that the eigenvalues may be divided into two groups. One

group having real eigenvalues corresponds to waves traveling without decay from the origin along the z direction. The other group has purely imaginary or complex eigenvalues and represents amplitude decaying waves. Then equation (2.76) can be simplified to,

$$\mathbf{Q}_m(z)=\begin{cases}-\dfrac{s_m}{r_b}\displaystyle\sum_{n=1}^{N_m}\dfrac{\left(\boldsymbol{\varphi}^L_{mn,l}\right)^T\mathbf{F}_b}{B_{mn}}\boldsymbol{\varphi}^R_{mn,u}e^{ik_{mn}z}, & z>0\\ -\dfrac{s_m}{r_b}\displaystyle\sum_{n=1}^{N_m}\dfrac{\left(\boldsymbol{\varphi}^L_{mn,l}\right)^T\mathbf{F}_b}{B_{mn}}\boldsymbol{\varphi}^R_{mn,u}e^{-ik_{mn}z}, & z<0\end{cases} \tag{2.77}$$

where the wave number (or eigenvalue, k_{mn}) is either a positive real number or a purely imaginary or complex number having a positive imaginary part. The Green's function of the cylinder is given by equation (2.63).

2.4 Numerical Applications

Illustrative numerical results are presented in this section for wave spectra and displacement Green's functions corresponding to a circular cylinder that is composed of isotropic or laminated composite materials. These results are used in Chapters 3 and 4 for solving wave scattering problems in cylinders. Examples 1 and 2 involve wave spectra for isotropic and laminated composite materials, respectively. Example 3 employs a convergence check of the Green's function arising from a point load in an isotropic material. The geometrical configuration of each cylinder is shown in Figure 2.1.

Example 1

The cylinder to be considered here was investigated, both experimentally and numerically, by Alleyne *et al.* (1998) and Lowe *et al.* (1998). It is made of steel so that the longitudinal and torsional wave speeds are given by,

$$c_1 = 5.96\times10^3\, m/s,\ c_2 = 3.26\times10^3\, m/s \tag{2.78}$$

respectively. Young's modulus is 216.9GPa. Two different pipes are considered that have a diameter of 76 *mm* or 152 *mm* and a thickness of 5.5 *mm* and 7 *mm*, respectively. Results for both cases are found to be quite similar. Therefore, for the present study, the inner radius, R_{inner}, and thickness, H, are chosen to be,

$$R_{inner} = 38mm \text{ and } H = 5.5mm. \tag{2.79}$$

The Poisson ratio, ν, and the ratio of the thickness to the mean radius, H/R, are, respectively,

$$\nu = 0.287,\quad H/R = 0.135. \tag{2.80}$$

The frequency spectrum for the longitudinal wave (m = 0) and the first flexural wave (m = 1) are shown in Figure 2.2. The phase speed is given as a function of frequency in Figure 2.3. The non-dimensional frequency, Ω, and the non-dimensional wave number, γ, are used in these figures. They are given by,

$$\Omega = \frac{\omega}{\omega_{ref}},\ \gamma = \frac{\xi}{\xi_{ref}} \tag{2.81}$$

where

$$\omega_{ref} = \frac{1}{H}\sqrt{\frac{\mu}{\rho}},\ \xi_{ref} = \frac{1}{H}. \tag{2.82}$$

Thus, a frequency of 100kHz corresponds to $\Omega = 1.06$. Figures 2.2 and 2.3 show that there are two longitudinal modes ($L(0, 1)$ and $L(0, 2)$) and three flexural modes ($F(1, 1)$, $F(1, 2)$, and $F(1, 3)$) propagating at this $\Omega = 1.06$ non-dimensional frequency. Other modes $F(m, n)$, $m > 1$, propagate at this frequency but they are not given so that a direct comparison can be made with the limited data of Alleyne *et al.* (1998).

Figure 2.3 shows that the $5.29\,mm/\mu s$ speed of the $L(0,2)$ and $F(1, 3)$ modes is nearly independent of frequency in the range $\Omega = 0.6 - 3$, or in the dimensional range from 56.6KHz to 283KHz. This value is somewhat higher than the speed ($c = 5.22\,mm/\mu s$) of the $L(0, 1)$ mode at very low frequencies. Note that the phase speed of the $F(1, 3)$ mode approaches that of the $L(0,2)$ mode at frequencies higher than about 75kHz. The phase speed of $F(1, 2)$ approaches the shear wave speed, c_2.

Due to their essentially non-dispersive nature over a significant frequency range, the incident waves for wave scattering in a cylinder are selected as $L(0,2)$ and $F(1, 3)$ in Chapter 3. The behaviour of these two wave modes is highlighted in Figure 2.3.

Example 2

A two-ply [0°/90°] graphite/epoxy, composite cylinder is considered next. The thickness of each sublayer is taken to be equal, i.e. $H_1 = H_2 = 0.5H$ where the hollow cylinder's total thickness is $H = H_1 + H_2$. The ratio of the thickness to the mean radius of the cylinder, H/R, is 0.1. The elastic properties of each ply are listed in Table 2.1.

The non-dimensional frequency, Ω, and wave number, γ, are defined in equation (2.81). The reference frequency and wave number are given here by,

$$\omega_{ref} = \frac{1}{H}\sqrt{\left(\frac{C_{55}}{\rho}\right)_{0^o}}, \quad \xi_{ref} = \frac{1}{H} \tag{2.83}$$

respectively.

Table 2.1 Laminated composite cylinder's material properties (C_{ij} in GPa). 0^o corresponds to the z direction.

Lamina	C_{11}	C_{12}	C_{13}	C_{33}	C_{44}	$\rho\,(g/cm^3)$
0^o Inside	13.92	6.92	6.44	160.73	7.07	1.8
90^o Outside	13.92	6.44	6.92	13.92	7.07	1.8

The frequency spectra for m equal 0 and 1 are shown in Figure 2.4. It can be seen from this figure that, there are three propagating modes for $m = 0$ and five for $m = 1$ in the non-dimensional frequency range $1 \le \Omega \le 3$. There are five propagating modes for $2 \le m \le 4$, and four for $m = 5$. For $m = 0$, the first cutoff frequency is $\Omega = 2.523$. For $m = 1$, the cutoff frequencies for the $4th$ and $5th$ modes are, respectively, 2.525 and 2.545; for $m = 2$, they are 2.531 and 2.600.

Figure 2.5 shows the variation in phase speed for different frequencies when $m = 0$ and $m = 1$. It can be seen from this figure that the phase speeds of each of the two wave modes, $L(0, 1)$ and $F(1, 1)$, are almost constant when $1 \le \Omega \le 3$ (or, alternatively, from 94.3Khz to 283Khz). Thus, the numerical results presented in Chapter 3 for wave scattering in a composite cylinder are in this range of Ω. (The analogous frequency-thickness product is between $0.3 \le fH \le 0.9 mm/\mu s$.) Moreover, the incident waves correspond to the $L(0, 1)$ and $F(1, 1)$ modes that are highlighted in Figure 2.5.

Example 3

Green's functions are used as incident fields in Chapter 4 for wave scattering problems solved by utilizing the boundary element method. Here, the results of a convergence check are shown in Figure 2.6 for an isotropic material. The material constants are the same as those used in example 1.

The point load acts on the outer surface of the cylinder, i.e. at (R_{outer}, 0^0, 0). The observation points are all along the radius of the cylinder at $\theta = 45^0$ and $z = H/4$. As discussed in the previous section, the Dirac delta function is approximated by the uniformly distributed force, $\hat{\delta}(\theta)$. The results shown in Figure 2.6 are for five different angles, $\hat{\theta}_0$, ranging from 0.001 to 0.2 (radian). The maximum values of $|G_M/G_{300}|$ that occur along r are presented. Here, M is the maximum circumferential wave number used to calculate the Green's function by employing the transform method. (See equation (2.63), for example.) G_M is the displacement Green's function involving the summation of circumferential wave numbers from $-M$ to $+M$, see equation (2.63). It can be seen from Figure 2.6 that more terms are needed as $\hat{\theta}_0$ decreases. For $\hat{\theta}_0 = 0.1$(radian), for instance, $|G_{60}/G_{300}| = 1.005$ which gives a relative difference of merely 0.5%. Therefore, when the boundary element method is used in Chapter 4, $\hat{\theta}_0$ is taken as 0.1(radian) for the approximation of $\delta(\theta)$ and M equal to 60 is used for the wave mode expansion.

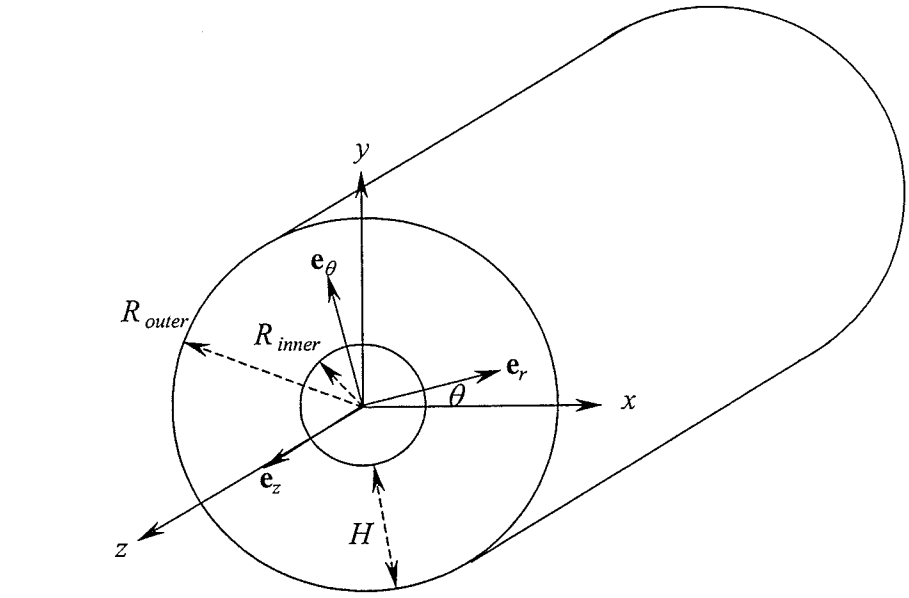

(a)

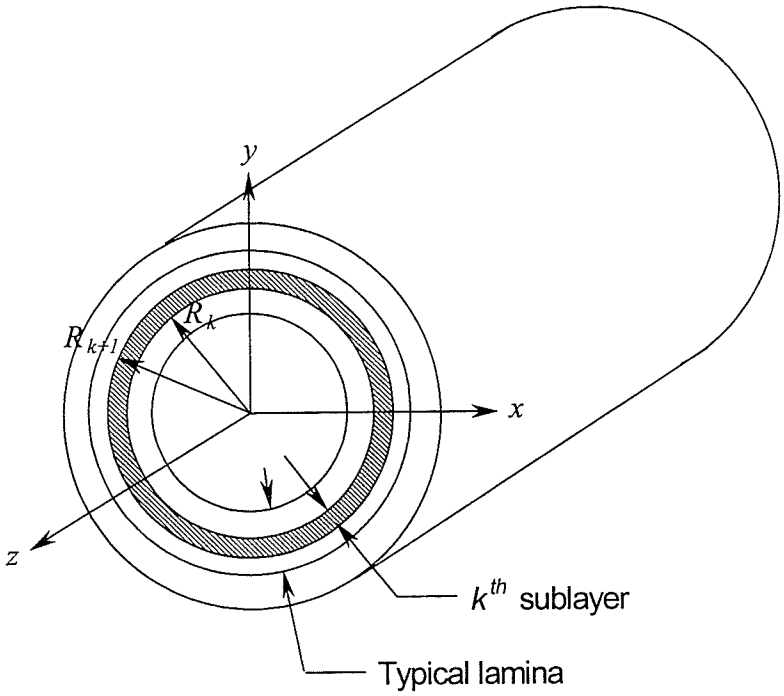

(b)

Figure 2.1. Configuration of (a) an isotropic cylinder, and (b) a laminated cylinder. R_{inner}: inner radius, R_{outer}: outer radius, H: cylinder's thickness

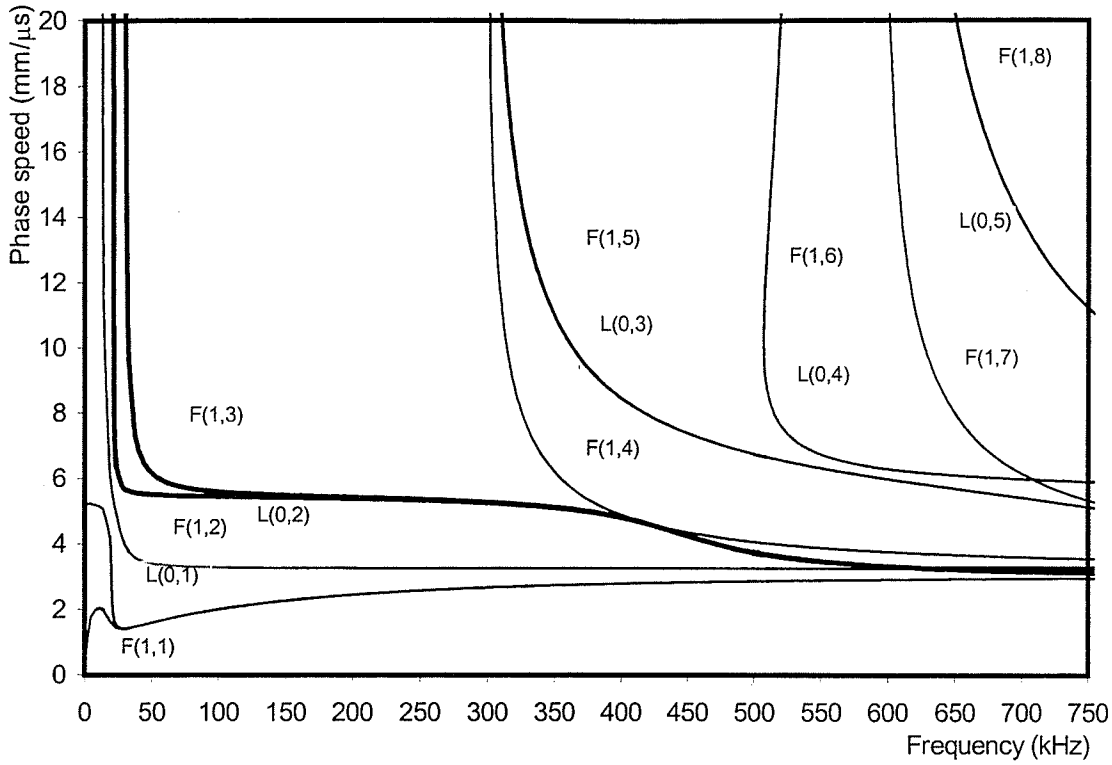

Figure 2.3. Phase speed as a function of frequency for a steel pipe. $H/R = 0.135$ and $\nu = 0.287$

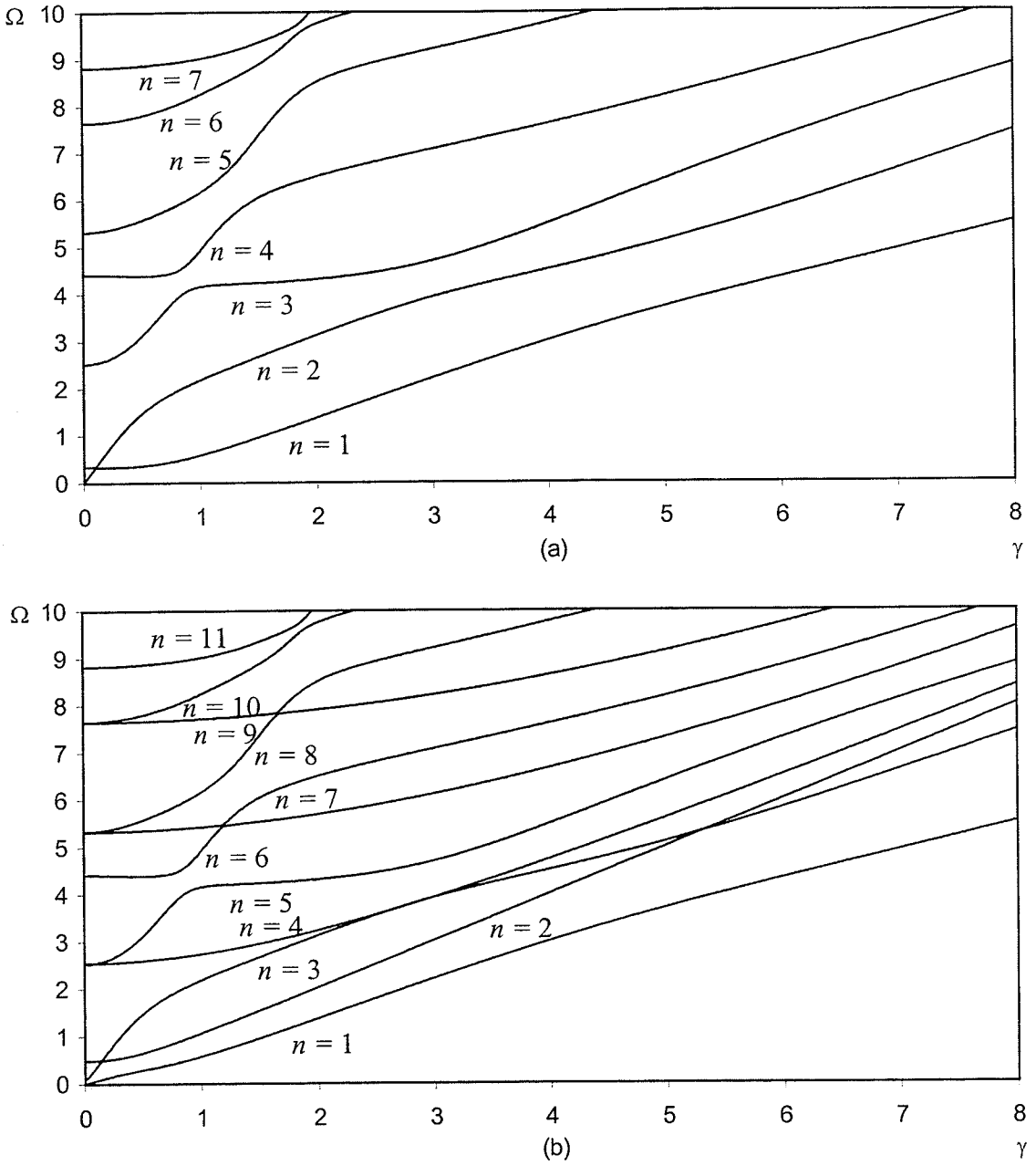

Figure 2.4. Frequency spectrum of a laminated cylinder [0°/90°]. (a) Longitudinal wave ($m = 0$), and (b) flexural wave ($m = 1$)

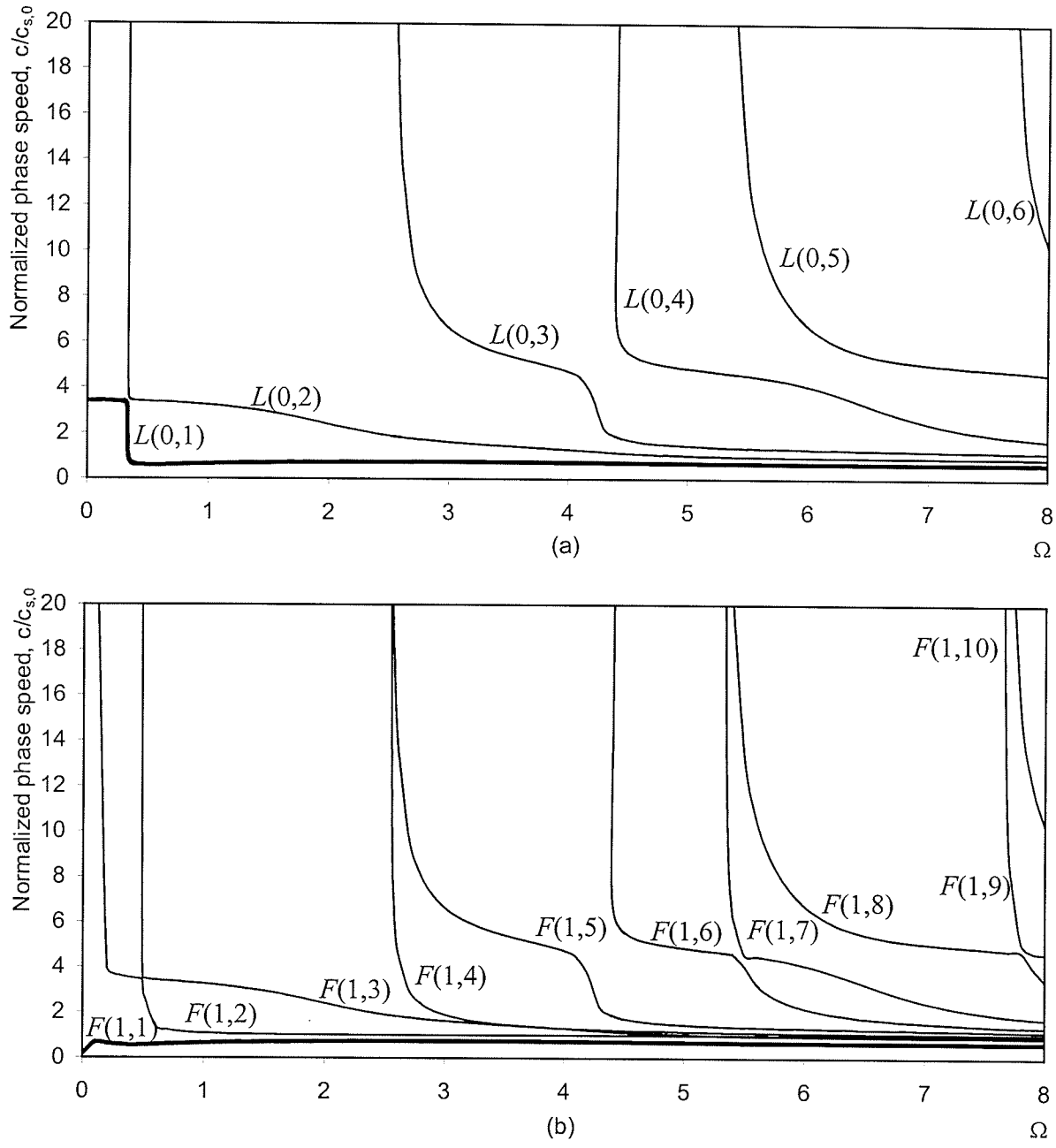

Figure 2.5. Normalized phase speed versus frequency for a 2-ply [0/90] graphite/epoxy cylinder with $H/R = 0.1$. (a) $m = 0$, and (b) $m = 1$

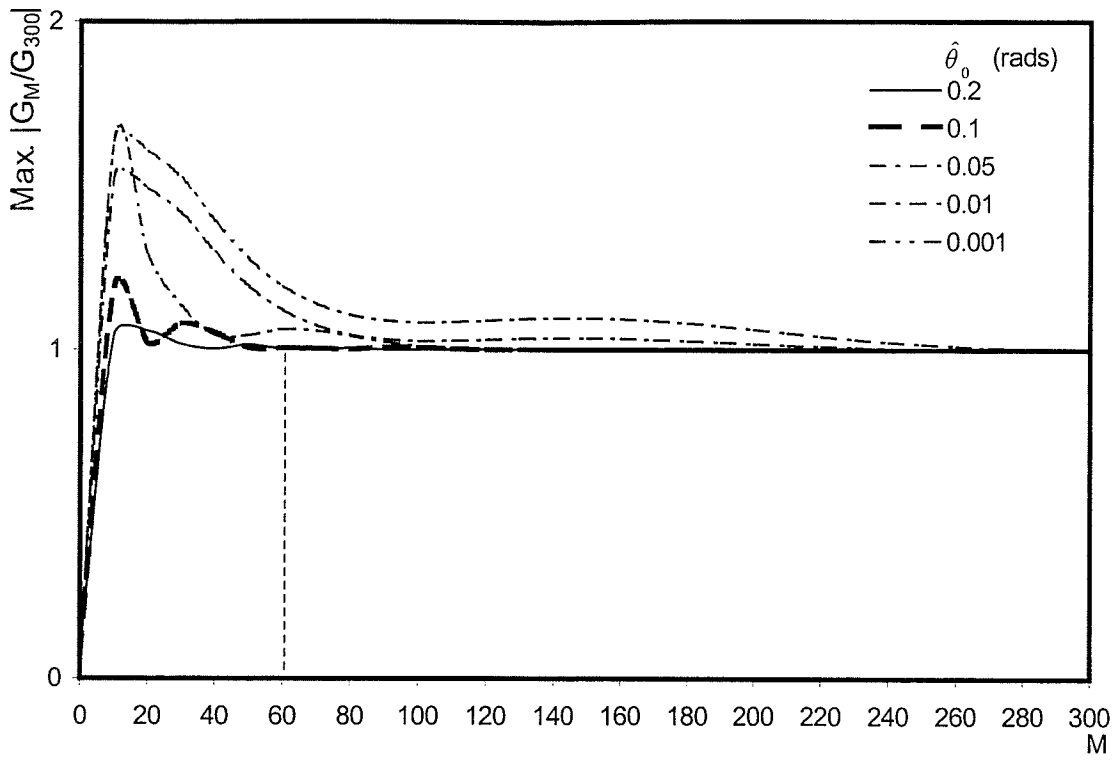

Figure 2.6. Convergence check for a point load located at (R_{outer}, 0^0, 0). The response is taken at (r, 45^0, $0.25H$)

Chapter 3

Wave Scattering in a Cylinder

3.1 Introduction

Circular tubes and pipelines are used extensively in the energy and transportation industries. These structural components are normally fabricated from metallic or composite materials. Damage occurs with handling, service load, natural disturbances, and environmental causes. Of particular interest in this study is the stress corrosion cracking that occurs in pipelines used in the oil, gas, and petrochemical industries. Ultrasonic nondestructive techniques are being developed to inspect the structural integrity of such industrial pipelines.

Guided waves in cylindrical pipes are similar in nature to those in plates. However, many more modes are excited in pipes (Alleyne et al., 1998). This difference makes an appropriate mode selection very critical for the success of an ultrasonic technique for a pipeline's inspection. The problem is complicated further if there are large cracks in the

pipe's wall. Thus, it is important to have accurate theoretical studies of ultrasonic wave propagation and scattering in cylindrical pipes.

As shown in previous studies (see, Zhuang et al., 1997 and Rattanawangcharoen et al., 1997), the hybrid method is effective for axisymmetric, wave scattering problems. However, for the three-dimensional scattering problem considered by Alleyne et al. (1998), either the hybrid or the full finite element method entails considerable, time consuming computations. The objective of this chapter is to give a more efficient combined analytical/numerical tool for the investigation of three-dimensional wave scattering by a circumferential crack in a cylindrical pipe. A treatment for arbitrarily oriented cracks is presented in the next chapter.

3.2 Description of the Problem

The problem of an infinitely long cylinder is considered. The cylinder is assumed to be homogeneous, isotropic or anisotropic. The crack is an ideal mathematical crack occupying a region located in the plane $z = 0$. It can have both an arbitrary length in the circumferential direction and an arbitrary depth in the radial direction. The geometry of the cracked cylinder is shown in Figure 3.1. A time harmonic incident wave having angular frequency ω and wave number ξ_{kl}, where k denotes the circumferential wave number and l is the axial wave mode, is generated at $z = +\infty$ and travels in the negative z-direction.

In order to model wave scattering by a partial or fully circumferential crack, the problem is decomposed into a symmetric problem and an antisymmetric problem about the plane of the crack. This approach has been used by Zhuang et al. (1999) to solve the

Green's function for a cylindrical shell. The scattered wave fields are expressed, in this approach, as the sums of admissible wave functions in the axial direction. The wave functions have been studied in Chapter 2. During the calculation of the reflection and transmission coefficients, the cylinder is discretized in both the circumferential, θ, and radial, r, directions over the cross-section $z = 0$. This situation is illustrated in Figure 3.2. Boundary conditions for the symmetric and anti-symmetric problems are imposed on these discrete points (nodes). Then, by using a transfer matrix approach, the problem can be simplified to a quasi-one-dimensional problem.

The objective of this study is to investigate how the circumferential length and radial depth of circumferential cracks affect the wave scattering characteristics in a cylinder. Reflection and transmission coefficients are presented for a steel pipe, as well as for a laminated composite pipe, for various incident wave fields. The principle of energy conservation is used to ensure accurate numerical computations. Reflection coefficients in a steel pipe for the incident $L(0, 2)$ mode are compared with the experiment data of Alleyne *et al.* (1998).

3.3 Symmetry and Anti-symmetry Arguments

Because of the linearity of the governing equations and boundary conditions at $z = 0$, the superposition principle can be used. Also, the displacement and traction components at the plane $z = 0$ can be arranged into two groups. One group has displacement components in the radial and circumferential directions, as well as a traction component in the axial direction, that are all prescribed. The other group contains the axial displacement component and the traction components in the radial and circumferential directions. It can

be shown that the quantities in the first group are known when the external forces are symmetrical about the plane $z = 0$. On the other hand, quantities in the second group are known if the external forces are anti-symmetrical about $z = 0$. In either case, only half the pipe ($z \geq 0$) needs to be modeled. Then, by using superposition, a solution to the general three-dimensional case can be constructed.

3.3.1 Modal Expansion

In the numerical procedure, a wave function expansion method is used to represent the three dimensional, incident and scattered wave fields travelling in the axial direction. It should be pointed out that material properties affect the wave modes but not the overall numerical procedure.

Assume that the incident wave is generated at $z = +\infty$ and travels in the negative z-direction. Scattering (i.e. reflection and transmission) occurs when the incident wave strikes the crack located at z = 0. The scattered wave field has a finite number of propagating modes and an infinite number of non-propagating modes. Due to symmetry and anti-symmetry considerations, only the reflected wave field needs to be evaluated in the positive z-direction. (Note that the time dependent factor $e^{-i\omega t}$ is suppressed again in the following formulation.) The displacements and stresses of the wave field are expanded as,

$$
\begin{aligned}
u_r(r,\theta,z) &= \sum_{m=-M}^{M}\sum_{n=1}^{N_m} u_{r,mn}(r)\,a_{kl,mn}\,e^{i(m\theta+\xi_{mn}z)} = \sum_{m=-M}^{M} \mathbf{U}_{r,m}(r)\,\mathbf{E}_m(z)\,\mathbf{a}_{kl,m}\,e^{im\theta} \\
u_\theta(r,\theta,z) &= \sum_{m=-M}^{M}\sum_{n=1}^{N_m} u_{\theta,mn}(r)\,a_{kl,mn}\,e^{i(m\theta+\xi_{mn}z)} = \sum_{m=-M}^{M} \mathbf{U}_{\theta,m}(r)\,\mathbf{E}_m(z)\,\mathbf{a}_{kl,m}\,e^{im\theta} \\
u_z(r,\theta,z) &= \sum_{m=-M}^{M}\sum_{n=1}^{N_m} u_{z,mn}(r)\,a_{kl,mn}\,e^{i(m\theta+\xi_{mn}z)} = \sum_{m=-M}^{M} \mathbf{U}_{z,m}(r)\,\mathbf{E}_m(z)\,\mathbf{a}_{kl,m}\,e^{im\theta}
\end{aligned}
\qquad (3.1)
$$

and

$$\begin{aligned}
\sigma_{zr}(r,\theta,z) &= \sum_{m=-M}^{M}\sum_{n=1}^{N_m}\sigma_{zr,mn}(r)\,a_{kl,mn}e^{i(m\theta+\xi_{mn}z)} = \sum_{m=-M}^{M}\mathbf{S}_{zr,m}(r)\,\mathbf{E}_m(z)\,\mathbf{a}_{kl,m}e^{im\theta}\\
\sigma_{z\theta}(r,\theta,z) &= \sum_{m=-M}^{M}\sum_{n=1}^{N_m}\sigma_{z\theta,mn}(r)\,a_{kl,mn}e^{i(m\theta+\xi_{mn}z)} = \sum_{m=-M}^{M}\mathbf{S}_{z\theta,m}(r)\,\mathbf{E}_m(z)\,\mathbf{a}_{kl,m}e^{im\theta}\\
\sigma_{zz}(r,\theta,z) &= \sum_{m=-M}^{M}\sum_{n=1}^{N_m}\sigma_{zz,mn}(r)\,a_{kl,mn}e^{i(m\theta+\xi_{mn}z)} = \sum_{m=-M}^{M}\mathbf{S}_{zz,m}(r)\,\mathbf{E}_m(z)\,\mathbf{a}_{kl,m}e^{im\theta}
\end{aligned} \tag{3.2}$$

with

$$\begin{aligned}
\mathbf{U}_{r,m}(r) &= \left[u_{r,m1}(r) \quad u_{r,m2}(r) \quad \cdots \quad u_{r,mN_m}(r)\right] \in \mathbf{C}^{1\times N_m}\\
\mathbf{U}_{\theta,m}(r) &= \left[u_{\theta,m1}(r) \quad u_{\theta,m2}(r) \quad \cdots \quad u_{\theta,mN_m}(r)\right] \in \mathbf{C}^{1\times N_m}\\
\mathbf{U}_{z,m}(r) &= \left[u_{z,m1}(r) \quad u_{z,m2}(r) \quad \cdots \quad u_{z,mN_m}(r)\right] \in \mathbf{C}^{1\times N_m}
\end{aligned} \tag{3.3}$$

$$\begin{aligned}
\mathbf{S}_{zr,m}(r) &= \left[\sigma_{zr,m1}(r) \quad \sigma_{zr,m2}(r) \quad \cdots \quad \sigma_{zr,mN_m}(r)\right] \in \mathbf{C}^{1\times N_m}\\
\mathbf{S}_{z\theta,m}(r) &= \left[\sigma_{z\theta,m1}(r) \quad \sigma_{z\theta,m2}(r) \quad \cdots \quad \sigma_{z\theta,mN_m}(r)\right] \in \mathbf{C}^{1\times N_m}\\
\mathbf{S}_{zz,m}(r) &= \left[\sigma_{zz,m1}(r) \quad \sigma_{zz,m2}(r) \quad \cdots \quad \sigma_{zz,mN_m}(r)\right] \in \mathbf{C}^{1\times N_m}
\end{aligned} \tag{3.4}$$

$$\mathbf{a}_{kl,m} = \left\{a_{kl,m1} \quad a_{kl,m2} \quad \cdots \quad a_{kl,mN_m}\right\}^T \in \mathbf{C}^{N_m\times 1} \tag{3.5}$$

and

$$\mathbf{E}_m(z) = \mathrm{diag}\left[e^{i\xi_{m1}z} \quad e^{i\xi_{m2}z} \quad \cdots \quad e^{i\xi_{mN_m}z}\right] \in \mathbf{C}^{N_m\times N_m}. \tag{3.6}$$

The $a_{kl,mn}$ are unknown complex coefficients that need to be determined. The first two subscripts, k and l, of the coefficients indicate the wave numbers of the incident wave in the circumferential and axial directions, respectively. The last two subscripts show the coefficients of the scattered wave fields corresponding to the wave numbers, m and n, in the circumferential and axial directions, respectively. The symbol $\boldsymbol{x} \in \mathbf{C}^{m\times n}$ means that $\boldsymbol{x}$ is a complex matrix having order m by n. It may be pointed out that the number of axial modes, N_m, need not be the same for each circumferential wave number, m. The

displacement wave functions, $u_{i,mn}$, $i = r, \theta, z,$ are derived in Chapter 2. The stress wave functions $\sigma_{ij,mn}$, $i, j = r, \theta, z,$ are obtained from the general displacement-strain and stress-strain relations.

For computational purposes, the continuous functions used in expansions (3.1) and (3.2) are evaluated at discrete points of the cross section containing the crack. This cross-section is divided into 6-node elements having a uniform distribution in both the circumferential and radial directions, as shown in Figure 3.2. The number of divisions in the radial and circumferential directions is p and q, respectively. In order to represent the circular cross-section, three nodes are used in the circumferential direction. With the geometry of the mesh shown in Figure 3.2, consistent forces can be obtained by using standard procedures (see Bathe, 1982) from the stresses associated with the wave modes.

Expansions (3.1) and (3.2) satisfy the traction free conditions required on the inner and outer surfaces of the cylinder. Hence, only the boundary conditions at the end, $z = 0$, have to be satisfied. Because of the crack's existence, care must be taken on this region of the cross-section when dealing with the boundary conditions. Traction-free boundary conditions for both the symmetrical and anti-symmetrical cases are imposed on the crack face. Therefore, for the symmetrical case, the boundary conditions are given by,

$$\mathbf{S} = \mathbf{S}^I + \mathbf{S}^R = \begin{Bmatrix} \mathbf{S}_C^I \\ \mathbf{S}_N^I \end{Bmatrix} + \begin{Bmatrix} \mathbf{S}_C^R \\ \mathbf{S}_N^R \end{Bmatrix} = 0, \text{ at } z = 0 \tag{3.7}$$

with

$$\mathbf{S}_C^I = \begin{Bmatrix} f_r^I \\ f_\theta^I \\ f_z^I \end{Bmatrix}, \ \mathbf{S}_N^I = \begin{Bmatrix} f_r^I \\ f_\theta^I \\ u_z^I \end{Bmatrix}, \ \mathbf{S}_C^R = \begin{Bmatrix} f_r^R \\ f_\theta^R \\ f_z^R \end{Bmatrix}, \ \mathbf{S}_N^R = \begin{Bmatrix} f_r^R \\ f_\theta^R \\ u_z^R \end{Bmatrix}. \tag{3.8}$$

For anti-symmetry, on the other hand, the boundary conditions are,

$$\mathbf{A} = \mathbf{A}^I + \mathbf{A}^R = \begin{Bmatrix} \mathbf{A}_C^I \\ \mathbf{A}_N^I \end{Bmatrix} + \begin{Bmatrix} \mathbf{A}_C^R \\ \mathbf{A}_N^R \end{Bmatrix} = 0, \text{ at } z = 0 \tag{3.9}$$

with

$$\mathbf{A}_C^I = \begin{Bmatrix} f_r^I \\ f_\theta^I \\ f_z^I \end{Bmatrix}, \ \mathbf{A}_N^I = \begin{Bmatrix} u_r^I \\ u_\theta^I \\ f_z^I \end{Bmatrix}, \ \mathbf{A}_C^R = \begin{Bmatrix} f_r^R \\ f_\theta^R \\ f_z^R \end{Bmatrix}, \ \mathbf{A}_N^R = \begin{Bmatrix} u_r^R \\ u_\theta^R \\ f_z^R \end{Bmatrix}. \tag{3.10}$$

The f_r, f_θ and f_z are the consistent force components in the r, θ and z directions, respectively, at the boundary $z = 0$. Superscript I and R represent quantities associated with the incident and scattered wave fields, respectively. Subscript C and N, on the other hand, represent whether a given point is located in the cracked or the uncracked region, respectively. Without loss of generality, assume that the nodal sequence is arranged so that the first P_C points are located in the cracked region with the remaining $P_N = P - P_C$ points located in the uncracked region.

Consider the symmetric case first. It should be pointed out that, when the mixed displacement and force components f_r, f_θ and u_z are known, the dual components u_r, u_θ and f_z are unknown for the point located in the uncracked region and vice versa. For the cracked region, all the force components are known and the corresponding dual displacement components are unknown.

Pointwise evaluation at the cross section $z = 0$ of the summation in equations (3.1) and (3.2) leads to,

$$\mathbf{E}_{m_i}(0) = \text{diag}\begin{bmatrix} 1 & 1 & \cdots & 1 \end{bmatrix} \in \mathbf{R}^{N_m \times N_m}.$$

Vectors $\mathbf{S}_C^R$ and $\mathbf{S}_N^R$ that are used in the boundary conditions (3.7) may be rewritten as,

$$\mathbf{S}_C^R = \mathbf{G}_C^R \mathbf{a}, \quad \mathbf{S}_N^R = \mathbf{G}_N^R \mathbf{a} \tag{3.11}$$

where

$$\begin{aligned}\mathbf{G}_C^R &= \begin{bmatrix}\mathbf{G}_{C,-M}^R & \cdots & \mathbf{G}_{C,m}^R & \cdots & \mathbf{G}_{C,M}^R\end{bmatrix} \in \mathbf{C}^{3P_C\times N} \\ \mathbf{G}_N^R &= \begin{bmatrix}\mathbf{G}_{N,-M}^R & \cdots & \mathbf{G}_{N,m}^R & \cdots & \mathbf{G}_{N,M}^R\end{bmatrix} \in \mathbf{C}^{3P_N\times N}\end{aligned} \tag{3.12}$$

$$\mathbf{a} = \begin{Bmatrix}\mathbf{a}_{kl,-M} & \cdots & \mathbf{a}_{kl,m} & \cdots & \mathbf{a}_{kl,M}\end{Bmatrix}^T \in \mathbf{C}^{N\times 1} \tag{3.13}$$

and

$$\mathbf{G}_{C,m}^R = \begin{bmatrix}\mathbf{F}_{C,r,m}^R \\ \mathbf{F}_{C,\theta,m}^R \\ \mathbf{F}_{C,z,m}^R\end{bmatrix} \in \mathbf{C}^{3P_C\times N_m},\ \mathbf{G}_{N,m}^R = \begin{bmatrix}\mathbf{F}_{N,r,m}^R \\ \mathbf{F}_{N,\theta,m}^R \\ \mathbf{U}_{N,z,m}^R\end{bmatrix} \in \mathbf{C}^{3P_N\times N_m}. \tag{3.14}$$

The total number of wave modes, N_T, considered in the wave function expansion is given by

$$N_T = \sum_{m=-M}^{M} N_m\ . \tag{3.15}$$

The N_m is the number of axial modes corresponding to the circumferential number m. The $\mathbf{a}_{kl,m}$ of equation (3.13) are given by equation (3.5). The specific forms of matrices $\mathbf{F}_{C,r,m}^R$, $\mathbf{F}_{C,\theta,m}^R$, $\mathbf{F}_{C,z,m}^R$, $\mathbf{F}_{N,r,m}^R$, $\mathbf{F}_{N,\theta,m}^R$ and $\mathbf{U}_{N,z,m}^R$ are presented more conveniently in Appendix B.

In a similar manner, the incident wave field, $\mathbf{S}^I$, can be constructed as,

$$\mathbf{S}_C^I = a_{kl}^I \mathbf{g}_{C,kl}^I,\ \mathbf{S}_N^I = a_{kl}^I \mathbf{g}_{N,kl}^I\ . \tag{3.16}$$

Here, vector $\mathbf{g}_{C,kl}^I$ is obtained from the l^{th} column of matrix $\mathbf{G}_{C,k}^R$ after replacing each r and θ directional force component by its negative value. The vector $\mathbf{g}_{N,kl}^I$ is obtained from the l^{th} column of matrix $\mathbf{G}_{N,k}^R$ after replacing each z direction force component by its negative value. The a_{kl}^I is the amplitude of the incident wave.

Equation (3.7) is solved by using the principle of virtual work. This is accomplished by forming vectors $\mathbf{T}_C^R$ and $\mathbf{T}_N^R$, which are the dual components of vectors $\mathbf{S}_C^R$ and $\mathbf{S}_N^R$, as,

$$\mathbf{T}^R = \begin{Bmatrix} \mathbf{T}_C^R \\ \mathbf{T}_N^R \end{Bmatrix} = \begin{bmatrix} \mathbf{H}_C^R \\ \mathbf{H}_N^R \end{bmatrix} \mathbf{a} \tag{3.17}$$

with

$$\mathbf{T}_C^R = \begin{Bmatrix} u_r^R \\ u_\theta^R \\ u_z^R \end{Bmatrix}, \ \mathbf{T}_N^R = \begin{Bmatrix} u_r^R \\ u_\theta^R \\ f_z^R \end{Bmatrix} \tag{3.18}$$

$$\begin{aligned} \mathbf{H}_C^R &= \begin{bmatrix} \mathbf{H}_{C,-M}^R & \cdots & \mathbf{H}_{C,m}^R & \cdots & \mathbf{H}_{C,M}^R \end{bmatrix} \in \mathbf{C}^{3P_C \times N}, \\ \mathbf{H}_N^R &= \begin{bmatrix} \mathbf{H}_{N,-M}^R & \cdots & \mathbf{H}_{N,m}^R & \cdots & \mathbf{H}_{N,M}^R \end{bmatrix} \in \mathbf{C}^{3P_N \times N}, \end{aligned} \tag{3.19}$$

$$\mathbf{H}_{C,m}^R = \begin{bmatrix} \mathbf{U}_{C,r,m}^R \\ \mathbf{U}_{C,\theta,m}^R \\ \mathbf{U}_{C,z,m}^R \end{bmatrix} \in \mathbf{C}^{3P_C \times N_m}, \ \mathbf{H}_{N,m}^R = \begin{bmatrix} \mathbf{U}_{N,r,m}^R \\ \mathbf{U}_{N,\theta,m}^R \\ \mathbf{F}_{N,z,m}^R \end{bmatrix} \in \mathbf{C}^{3P_N \times N_m}. \tag{3.20}$$

The specific form of the block matrices appearing in equation (3.20) can be found in Appendix B.

Applying the principle of virtual work to boundary condition (3.7) by multiplying it with the dual components, $\mathbf{T}_C^R$ and $\mathbf{T}_N^R$, yields,

$$\begin{bmatrix} \mathbf{H}_C^R \\ \mathbf{H}_N^R \end{bmatrix}^* \begin{bmatrix} \mathbf{G}_C^R \\ \mathbf{G}_N^R \end{bmatrix} \mathbf{a} = -a_{kl}^I \begin{bmatrix} \mathbf{H}_C^R \\ \mathbf{H}_N^R \end{bmatrix}^* \begin{Bmatrix} \mathbf{g}_{C,kl}^I \\ \mathbf{g}_{N,kl}^I \end{Bmatrix}. \tag{3.21}$$

Here the $*$ superscript denotes the complex conjugate plus matrix transpose.

The solutions of equation (3.21) are the reflection coefficients that are associated with different wave modes. Knowing these coefficients, values of the displacement and stress components are readily obtained at different locations in the cylinder by substituting the coefficients into expansions (3.1) and (3.2).

3.3.2 Transfer Matrix Approach

It should be noted that equation (3.21) is derived by using pointwise conditions. Due to the large number of nodes in the two-dimensional mesh of plane $z = 0$, as shown in Figure 3.2, this procedure is computationally demanding. If a transfer matrix is considered from radius to radius, instead of from point to point, calculations can be performed more efficiently. This idea is based upon the circular symmetry of the cylinder's geometry and the physical characteristics of the problem. (See, for example, the expansions (3.1) and (3.2).)

Let p be the number of nodes in a radius and q be the number of subdivisions in the circumferential direction. Define two adjacent radii, $\theta = 2j\pi/q$ and $\theta = (2j+1)\pi/q$, for j = 0, 1, …, q-1, as the j^{th} radius pair. Without loss of generality, assume that q_C radii pairs are located in the cracked region and q_N are in the uncracked region.

Consider two vectors, $\mathbf{f}_{C,r,mn} \in \mathbf{C}^{P_C \times 1}$ and $\mathbf{f}_{N,r,mn} \in \mathbf{C}^{P_N \times 1}$, which are in the n^{th} column of the matrices $\mathbf{F}^R_{C,r,m}$ and $\mathbf{F}^R_{N,r,m}$ given in (B.1) and (B.2), as an illustrative example. These two vectors are evaluated at all the nodes of the cracked and uncracked regions, respectively. The specified forms of these two vectors are,

$$\mathbf{f}_{C,r,mn} = \begin{Bmatrix} \mathbf{f}^{(1)}_{C,r,mn} \\ \mathbf{f}^{(2)}_{C,r,mn} \\ \vdots \\ \mathbf{f}^{(q_c)}_{C,r,mn} \end{Bmatrix} \in \mathbf{C}^{P_c \times 1}, \quad \mathbf{f}_{N,r,mn} = \begin{Bmatrix} \mathbf{f}^{(q_c+1)}_{N,r,mn} \\ \mathbf{f}^{(q_c+2)}_{N,r,mn} \\ \vdots \\ \mathbf{f}^{(q_c+q_N)}_{N,r,mn} \end{Bmatrix} \in \mathbf{C}^{P_N \times 1} \tag{3.22}$$

where $\mathbf{f}^{(j)}_{C,r,mn} \in \mathbf{C}^{2p \times 1}$ (j = 1, 2, …, q_C) and $\mathbf{f}^{(j)}_{N,r,mn} \in \mathbf{C}^{2p \times 1}$ ($j = q_C$+1, q_C+2, …, q_C+q_N) are vectors evaluated at the two adjacent radii pair $\theta = 2j\pi/q$ and $\theta = (2j+1)\pi/q$.

Considering the wave functions in equations (3.1) and (3.2), it can be shown that the values of the two vectors, $\mathbf{f}_{C,r,mn}^{(j)}$ and $\mathbf{f}_{N,r,mn}^{(j)}$, are obtained by using only a rotation, $e^{2im(j-1)\pi/q}$, of the two vectors $\mathbf{f}_{C,r,mn}^{(1)}$ and $\mathbf{f}_{N,r,mn}^{(1)}$. Therefore, the following relations hold,

$$\mathbf{f}_{C,r,mn}^{(j)} = \lambda_m^{j-1}\mathbf{f}_{C,r,mn}^{(1)}, \quad 1 \le j \le q_C \tag{3.23}$$

and

$$\mathbf{f}_{N,r,mn}^{(j)} = \lambda_m^{j-1}\mathbf{f}_{N,r,mn}^{(1)}, \quad q_C + 1 \le j \le q = q_C + q_N \tag{3.24}$$

where

$$\lambda_m = e^{2im\pi/q}. \tag{3.25}$$

Thus, equation (3.22) can be rewritten in a more compact form as,

$$\mathbf{f}_{C,r,mn} = \mathbf{\Lambda}_{C,m} f_{C,r,mn}^{(1)}, \; \mathbf{f}_{N,r,mn} = \mathbf{\Lambda}_{N,m}\mathbf{f}_{N,r,mn}^{(1)} \tag{3.26}$$

with the transfer matrices, $\mathbf{\Lambda}_{C,m}$ and $\mathbf{\Lambda}_{N,m}$, given by,

$$\mathbf{\Lambda}_{C,m} = \left[\hat{\mathbf{I}} \quad \lambda_m\hat{\mathbf{I}} \quad \ldots \quad \lambda_m^{q_C-1}\hat{\mathbf{I}}\right]^T \in \mathbf{C}^{2pq_C \times 2p} \tag{3.27}$$

and

$$\mathbf{\Lambda}_{N,m} = \lambda_m^{q_C}\left[\hat{\mathbf{I}} \quad \lambda_m\hat{\mathbf{I}} \quad \ldots \quad \lambda_m^{q_N-1}\hat{\mathbf{I}}\right]^T \in \mathbf{C}^{2pq_N \times 2p}. \tag{3.28}$$

Here, $\hat{\mathbf{I}}$ is the unit square matrix of order $2p$, where $2p$ is the total number of nodes in a radii pair. With the help of equation (3.26), the matrices $\mathbf{F}_{C,r,m}^R$ and $\mathbf{F}_{N,r,m}^R$ can be expressed as,

$$\mathbf{F}_{C,r,m}^R = \mathbf{\Lambda}_{C,m}\mathbf{F}_{C,r,m}^{(1)R}, \quad \mathbf{F}_{N,r,m}^R = \mathbf{\Lambda}_{N,m}\mathbf{F}_{N,r,m}^{(1)R}. \tag{3.29}$$

All the other matrices given in Appendix B have similar expressions. By using these expressions, the matrices $\mathbf{G}_C^R$ and $\mathbf{G}_N^R$ can be shown to have the following forms,

$$\mathbf{G}_C^R = \left[\tilde{\mathbf{\Lambda}}_{C,-M}\mathbf{G}_{C,-M}^{(1)R} \quad \cdots \quad \tilde{\mathbf{\Lambda}}_{C,m}\mathbf{G}_{C,m}^{(1)R} \quad \cdots \quad \tilde{\mathbf{\Lambda}}_{C,M}\mathbf{G}_{C,M}^{(1)R} \right] \tag{3.30}$$

and

$$\mathbf{G}_N^R = \left[\tilde{\mathbf{\Lambda}}_{N,-M}\mathbf{G}_{N,-M}^{(1)R} \quad \cdots \quad \tilde{\mathbf{\Lambda}}_{N,m}\mathbf{G}_{N,m}^{(1)R} \quad \cdots \quad \tilde{\mathbf{\Lambda}}_{N,M}\mathbf{G}_{N,M}^{(1)R} \right] \tag{3.31}$$

where

$$\tilde{\mathbf{\Lambda}}_{C,m} = \begin{bmatrix} \mathbf{\Lambda}_{C,m} & & \\ & \mathbf{\Lambda}_{C,m} & \\ & & \mathbf{\Lambda}_{C,m} \end{bmatrix} \text{ and } \tilde{\mathbf{\Lambda}}_{N,m} = \begin{bmatrix} \mathbf{\Lambda}_{N,m} & & \\ & \mathbf{\Lambda}_{N,m} & \\ & & \mathbf{\Lambda}_{N,m} \end{bmatrix} \in \mathbf{C}^{6pq_N \times 6p}. \tag{3.32}$$

The block matrices, $\mathbf{G}_{C,m}^{(1)R}$ and $\mathbf{G}_{N,m}^{(1)R}$, are obtained from $\mathbf{G}_{C,m}^R$ and $\mathbf{G}_{N,m}^R$ by replacing the corresponding force and displacement components with their reference vectors. The latter are evaluated only at the first radius pair. Similar relations hold also for the matrices $\mathbf{H}_C^R$, $\mathbf{H}_N^R$ and vectors $\mathbf{S}_C^I$, $\mathbf{S}_N^I$.

With the above simplifications, the following results are obtained,

$$\left(\mathbf{H}_C^R\right)^* \mathbf{G}_C^R = \begin{bmatrix} \cdots & \cdots & \cdots \\ \cdots & \mu_{C,m_1m_2}\left(\mathbf{H}_{C,m_1}^{(1)R}\right)^* \mathbf{G}_{C,m_2}^{(1)R} & \cdots \\ \cdots & \cdots & \cdots \end{bmatrix} \in \mathbf{C}^{N\times N} \tag{3.33}$$

$$\left(\mathbf{H}_N^R\right)^* \mathbf{G}_N^R = \begin{bmatrix} \cdots & \cdots & \cdots \\ \cdots & \mu_{N,m_1m_2}\left(\mathbf{H}_{N,m_1}^{(1)R}\right)^* \mathbf{G}_{N,m_2}^{(1)R} & \cdots \\ \cdots & \cdots & \cdots \end{bmatrix} \in \mathbf{C}^{N\times N} \tag{3.34}$$

$$\left(\mathbf{H}_C^R\right)^* \mathbf{S}_C^I = \begin{Bmatrix} \vdots \\ \mu_{C,mk}\left(\mathbf{H}_{C,m}^{(1)R}\right)^* \mathbf{g}_{C,kl}^{(1)R} \\ \vdots \end{Bmatrix} \in \mathbf{C}^{N\times 1} \tag{3.35}$$

$$\left(\mathbf{H}_N^R\right)^* \mathbf{S}_N^I = \left\{ \begin{array}{c} \vdots \\ \mu_{N,mk} \left(\mathbf{H}_{N,m}^{(1)R}\right)^* \mathbf{g}_{N,kl}^{(1)R} \\ \vdots \end{array} \right\} \in \mathbf{C}^{N\times 1} \tag{3.36}$$

and

$$\mu_{C,m_1m_2} = \begin{cases} q_C, & \text{for } m_1 = m_2 \\ \dfrac{1-\lambda_{m_1,m_2}^{q_C}}{1-\lambda_{m_1,m_2}}, & \text{for } m_1 \neq m_2 \end{cases} \tag{3.37}$$

$$\mu_{N,m_1m_2} = \begin{cases} q_N, & \text{for } m_1 = m_2 \\ -\dfrac{1-\lambda_{m_1,m_2}^{q_C}}{1-\lambda_{m_1,m_2}}, & \text{for } m_1 \neq m_2 \end{cases} \tag{3.38}$$

$$\lambda_{m_1,m_2} = \overline{\lambda}_{m_1} \lambda_{m_2} = e^{2i(m_2-m_1)\pi/q}. \tag{3.39}$$

Equations (3.37) and (3.38) may also be written as,

$$\mu_{C,m_1m_2} + \mu_{N,m_1m_2} = q\delta_{m_1m_2} \tag{3.40}$$

where

$$\delta_{m_1m_2} = \begin{cases} 1, & \text{for } m_1 = m_2 \\ 0, & \text{for } m_1 \neq m_2. \end{cases} \tag{3.41}$$

Substituting equations (3.33) through (3.36) into equation (3.21) results in the final equation,

$$\left[\left(\mathbf{H}_C^R\right)^* \mathbf{G}_C^R + \left(\mathbf{H}_N^R\right)^* \mathbf{G}_N^R\right] \mathbf{a} = -a_{kl}^I \left[\left(\mathbf{H}_C^R\right)^* \mathbf{S}_C^I + \left(\mathbf{H}_N^R\right)^* \mathbf{S}_N^I\right]. \tag{3.42}$$

It can be seen from equations (3.33) to (3.38) that all the matrices need be computed solely once, i.e. only for the first radius pair. In other words, the circumferential discretization does not affect the size of the matrices or the computational time. Hence, the problem is reduced to a quasi-one-dimensional nature.

When q_C equals q, q_N becomes zero. This condition arises from an axisymmetrical crack. Then it is obvious that $\mu_{C,m_1m_2}=0$, when $m_1 \neq m_2$, $\mu_{N,m_1m_2}=0$ for all m_1 and m_2, and $\mu_{C,mm}=q$. Therefore, matrices $\left(\mathbf{H}_C^R\right)^* \mathbf{G}_C^R$ and $\left(\mathbf{H}_N^R\right)^* \mathbf{G}_N^R$ are reduced to a diagonal block form. Furthermore, the vectors in equations (3.35) and (3.36), $\left(\mathbf{H}_C^R\right)^* \mathbf{S}_C^I$ and $\left(\mathbf{H}_N^R\right)^* \mathbf{S}_N^I$, are reduced to zero. But the k^{th} block vector remains unchanged. Hence, the problem has a smaller dimension and only the wave modes related to the circumferential wave number, k, and the incident wave number in the circumferential direction, need be considered. In this situation, it is straightforward to show that the subdivision in the circumferential direction does not add complexity to the numerical procedure because parameter q is eliminated from the final linear equation.

Once the linear equation (3.21) is established, the reflection coefficients for the symmetrical case can be obtained. The anti-symmetrical case can be solved similarly so that it is not repeated for brevity. Knowing the solutions of these two cases, the reflection and transmission coefficients, $R_{kl,mn}$ and $T_{kl,mn}$, for the complete problem are derived easily as,

$$R_{kl,mn}=\frac{a_{kl,mn}^S+a_{kl,mn}^A}{2a_{kl}^I} \text{ and } T_{kl,mn}=\frac{a_{kl,mn}^S-a_{kl,mn}^A}{2a_{kl}^I}. \tag{3.43}$$

The $a_{kl,mn}^S$ and $a_{kl,mn}^A$ represent the solutions for the symmetrical and anti-symmetrical problems, respectively.

3.3.3 Energy Conservation

One of the physical quantities of interest is the mean total energy flux. Energy is carried only by the propagating modes existing at a given frequency. The time-average energy fluxes of the reflection and transmission waves for the mn^{th} propagating mode are given by,

$$E_{mn}^{R} = \omega \mid R_{kl,mn} \mid^2 \operatorname{Im}\left(\int_{R_i}^{R_o} \mathbf{F}_{mn}^{T} \overline{\boldsymbol{\varphi}}_{mn} r dr \right) \text{ and } E_{mn}^{T} = \omega \mid T_{kl,mn} \mid^2 \operatorname{Im}\left(\int_{R_i}^{R_o} \mathbf{F}_{mn}^{T} \overline{\boldsymbol{\varphi}}_{mn} r dr \right). \quad (3.44)$$

The $R_{kl,mn}$ *and* $T_{kl,mn}$ are the reflection and transmission coefficients, respectively. $\boldsymbol{\varphi}_{mn}$ is the displacement mode, i.e. the eigenvector derived in Chapter 2. $\mathbf{F}_{mn}$ is the corresponding force obtained from the regular stress-strain and strain-displacement relations. The mean total energy flux is obtained from the sum of the energy fluxes carried by all the propagating modes that are involved in both the reflections and transmissions. It is given by,

$$E_{total} = \sum_{m,n} \left(E_{mn}^{R} + E_{mn}^{T} \right). \quad (3.45)$$

The mean energy flux of the incident field has the similar form,

$$E_{in} = \omega \operatorname{Im}\left(\int_{R_i}^{R_o} \mathbf{F}_{kl}^{T} \overline{\boldsymbol{\varphi}}_{kl} r dr \right). \quad (3.46)$$

Define ε as the percentage difference in the energy balance or,

$$\varepsilon = \left| \frac{E_{in} - E_{total}}{E_{in}} \right| \times 100\%. \quad (3.47)$$

Since there is no energy dissipation during wave scattering, $\varepsilon = 0$ because of energy conservation. Thus, the value of ε serves as an accuracy check of the numerical data.

3.4 Numerical Results and Discussion

The method described in the previous section to analyze the effect of planar cracks located in a cross-section of a pipe wall can be used for both isotropic and anisotropic materials. As shown before, the crack can have both a circumferential length and an arbitrary depth in the radial direction. (Note that the crack need not break the pipe's outer surface.) Now θ_0 is defined, again, as the half circumferential crack angle (in radians), d is the crack depth, measured from the pipe's outer surface, and the non-dimensional crack length, L, is given by,

$$L = \frac{2R\theta_0}{2\pi R} = \frac{\theta_0}{\pi} \tag{3.48}$$

where R is the mean radius of the cylinder. The non-dimensional crack depth, D, on the other hand, is,

$$D = \frac{d}{H} \tag{3.49}$$

where H is the pipe's thickness.

Two examples are considered to demonstrate the effectiveness and accuracy of the present approach.

1. The first example is a steel pipe that was investigated by Alleyne et al. (1998) and Lowe et al. (1998). The same geometrical and material properties are used so that

the present method's predictions can be compared directly with the experimental observations.

2. The second example is a 2-ply [0°/90°] graphite/epoxy hollow cylinder. This example demonstrates the versatility of the present approach.

Example 1. A steel pipe

In this example, the cross-section containing the crack is discretized into 6-node planar elements with three nodes in the θ direction of each element and two nodes in the r direction. The material properties are identical to those used for example 1 of Chapter 2. They are reproduced here for convenience.

Young's modulus is 216.9 GPa. The longitudinal and torsional wave speeds are,

$$c_1 = 5.96\times10^3\ m/s,\ c_2 = 3.26\times10^3\ m/s$$

and the inner radius, R_{inner}, and thickness, H, of the cylinder are chosen to be,

$$R_{inner} = 38mm,\ H = 5.5mm$$

Therefore, the ratio of the thickness to the mean radius is $H/R = 0.135$ and the Poisson ratio is $\nu = 0.287$. The non-dimensional frequency, Ω, and the non-dimensional wave number, γ, are given as,

$$\Omega = \frac{\omega}{\omega_{ref}},\quad \gamma = \frac{\xi}{\xi_{ref}}$$

where

$$\omega_{ref} = \frac{1}{H}\sqrt{\frac{\mu}{\rho}};\quad \xi_{ref} = \frac{1}{H}$$

Thus, for a frequency of $100kHz$, $\Omega = 1.06$.

The wave spectra and the selection of the incident waves have been discussed in Chapter 2. Alleyene *et al.* (1998) presented experimental results in the frequency range of 60 to 85*KHz* (i.e. Ω = 0.64 to 0.90). The reflection of the incident $L(0, 2)$ mode was considered for circumferential cracks having different lengths and depths.

Numerical results are presented in this example for the reflection coefficients of mode-converted waves when the two modes $L(0, 2)$ and $F(1, 3)$ are incident separately on various circumferential cracks. A comparison is also given, whenever possible, with the experimental results.

First, the convergence of the numerical procedure was tested for different mesh sizes. The results were compared for several scattering problems. For each case, a different number of circumferential and axial modes was chosen in the modal expansion to check the convergence. The incident wave was selected to be the second wave mode, $L(0, 2)$, for which experimental data was available. By comparing successive sums from an increasing number of terms in the modal expansion, it was found that a mesh having p = 100 and q = 10000 nodes and M = 11 and N_m = 51 modes for m = 0 and N_m = 40 for $m = \pm 1, \pm 2, \ldots, \pm M$ gave acceptable results. Table 3.1 shows the rate of convergence of the series for the reflection coefficient from a crack having a 50% circumferential length and a depth of 0.5*H*. As noted in the previous section, convergence was also tested by checking the energy conservation. Since attention has been focused here on the reflection and transmission coefficients, singularities at the crack corners were not taken into account numerically because they have little effect in the far field. This observation has been verified by comparison with the experimental results reported in Alleyene *et al.* (1998).

After establishing convergence, the mesh size and number of modes were fixed for the remaining calculations. Reflection coefficients were calculated for two different crack depths, namely $0.5H$ and $0.55H$. It was found that the results for the $0.55H$ crack depth agreed better with the experimental data. Then the percentage error between the experimental data and the computations was less than 6% for the 100% circumferential crack. Using the same mesh and crack depth, the corresponding error for a 50% circumferential crack length was around 10%. This error was higher than that observed for the axisymmetrical case. There may be various reasons for this discrepancy. One major reason could be that the experimental notch had a finite width. Also, there could easily be inaccuracy in the measured notch depth. Furthermore, the experimental notch may not have been strictly planar. Consequently, all the results presented here correspond to a crack depth of $0.55H$ rather than 0.5H.

The comparison of the experimental and numerical reflection coefficients, expressed as functions of a frequency ranging from 60kHz to 85kHz (i.e. $\Omega = 0.64$ to 0.90) for the $L(0, 2)$ mode, are shown in Figure 3.3. Results are given for three different cracks having a length of 10%, 50%, and 100% along the pipe's circumference. The good agreement of the results validate the present numerical method.

The reflection and transmission coefficients, $|R_{02,mn}|$, $|T_{02,mn}|$, and $|R_{13,mn}|$, $|T_{13,mn}|$ are shown in Figures 3.4 and 3.5 for a circumferential crack length of 10%. All the reflection coefficients are very small, less then 0.07 . It is interesting to note that the presence of the crack has little influence on the incident $L(0,2)$ mode because most of its energy is transmitted. For the incident $F(1, 3)$ mode, on the other hand, most of the transmitted energy is shared between the $F(1, 2)$ and $F(1, 3)$ modes. The transmitted energy in the

$F(1,2)$ mode increases with frequency so that, not surprisingly, the $F(1,3)$ mode energy loses energy with increasing frequency.

Similar results are presented in Figures 3.6 and 3.7 for the 50% circumferential crack length. Again, the transmitted wave field has very similar characteristics to that produced by the $L = 10\%$ circumferential crack. However, in the reflected field, $|R_{02,01}|$ has the largest value, followed by $|R_{02,02}|$and $|R_{02,11}|$. It is seen that the reflection and transmission coefficients have a very weak dependence on frequency. This would be desirable for ultrasonic measurements over long pipes. For the incident mode $F(1, 3)$, Figure 3.7 shows that the reflected amplitude $|R_{13,11}|$ is largest, followed by $|R_{13,13}|$ and $|R_{13,01}|$. Thus, the asymmetry of the crack causes more energy to go into the bending modes, as expected.

Results of the reflection and transmission coefficients, $|R_{02,mn}|$, $|T_{02,mn}|$, as well as $|R_{13,mn}|$ and $|T_{13,mn}|$, are shown in Figures 3.8 and 3.9 as functions of the circumferential crack length for a frequency, f, of $70KHz$. The experimental results are also presented in Figure 3.8. As noted by Alleyne *et al.* (1998), it is interesting that the reflection coefficient, $|R_{kl,kl}|$, for $k = 0$, $l = 2$, is nearly a linear function of the circumferential crack length. The same observation holds true for $|R_{02,01}|$, $|R_{13,13}|$, and $|R_{13,11}|$. It is to be noted that $|R_{02,01}|$ is larger than $|R_{02,02}|$. For the transmission coefficients, the numerical results given in Figure 3.8 have the interesting feature that $|T_{02,02}|$ and $|T_{02,01}|$ are also nearly linear functions of L; the former decreases with increasing L and the latter increases with L.

Example 1 is reassessed next to compare the results of employing approximate eigenvectors in equations (3.1) through (3.4) as opposed to the analytical eigenfunctions. (See Sections 2.1 and 2.2.) The reflection and transmission coefficients are presented in

Figure 3.10. The results obtained with the approximate eigenvectors are designated "present" while the ones found by using the analytical eigenfunctions are labelled "previous". It can be seen that two sets of the results are in good agreement. Therefore, the more computationally efficient, approximate eigenvectors are used in the following example.

Example 2. A 2-ply [0°/90°] graphite/epoxy hollow cylinder

In this example, the cross-section containing the crack is discretized into 9-node, planar elements. The material properties were given in Table 3.2. They are reproduced again below for convenience.

Table 3.2 Laminated composite cylinder's material properties (C_{ij} in GPa). 0^o corresponds to the z direction.

Lamina	C_{11}	C_{12}	C_{13}	C_{33}	C_{44}	$\rho\,(g/cm^3)$
0^o Inside	13.92	6.92	6.44	160.73	7.07	1.8
90^o Outside	13.92	6.44	6.92	13.92	7.07	1.8

As discussed in example 2 of Chapter 2, the scattering of the incoming, propagating $L(0, 1)$ and $F(1, 1)$ modes is considered in a two-ply $[0^o/90^o]$ graphite/epoxy cylinder. The non-dimensional frequency, Ω, and the non-dimensional wave number, γ, are given as,

$$\Omega = \frac{\omega}{\omega_{ref}}; \quad \gamma = \frac{\xi}{\xi_{ref}} \tag{3.50}$$

where

$$\omega_{ref} = \frac{1}{H}\sqrt{\left(\frac{C_{55}}{\rho}\right)_{0^o}}, \quad \xi_{ref} = \frac{1}{H}. \tag{3.51}$$

The non-dimensional circumferential crack length, L, and radial crack depth, D, are defined in equations (3.48) and (3.49). Here $H_1 = H_2$ and $H = H_1 + H_2$. It may be noted that there are three propagating modes for $m = 0$ and five for $m = 1$ in the frequency range $1 \le \Omega \le 3$. (See Figure 2.4.) There are five propagating modes for $2 \le m \le 4$, and four for $m = 5$. For $m = 0$, the first cutoff frequency is $\Omega = 2.523$. For $m = 1$, the cutoff frequencies for the $4th$ and $5th$ modes are, respectively, 2.525 and 2.545; for $m = 2$, they are 2.531 and 2.600.

For the numerical results, the thickness to mean radius and non-dimensional radial crack depth are given by,

$$H/R = 0.1 \text{ and } D = 0.50$$

so that the crack extends through the thickness of the 90^o ply. The non-dimensional circumferential crack length, L, is varied from 10% to 50% and 100% of the circumferential length.

The convergence of the numerical results was checked first by considering different mesh sizes as well as by comparing successive sums for an increasing number of circumferential and axial wave modes. It was found that a mesh having 16 sublayers in the radial direction, 10000 segments in the circumferential direction and 23 circumferential wave numbers (i.e. the $N_0 = 30$ modes for $m = 0$ and $N_m = 43$ modes for $1 \le |m| \le 11$ where N_m is the number of axial wave number corresponding to the circumferential wave number, m, used in the wave mode expansion) generated results that essentially remained unchanged with additional increases in either number or meshes or number of wave modes.

Figure 3.11 shows the reflection coefficients for different modes when the incident mode is $L(0, 1)$. Three different normalized circumferential crack lengths of 10%, 50%, and 100% are considered. Note that, in the last case, the problem is axisymmetric so that only the $m = 0$ modes are excited. Sharp peaks are observed in the reflection coefficients at the first cutoff frequency, Ω =2.53. Furthermore, the reflection coefficients are found to be quite significant for all the propagating modes when $m = 1$. Figure 3.12, on the other hand, presents the reflection and transmission coefficients as functions of the non-dimensional crack depth, D, when $\Omega = 3.0$. $|R_{01,02}|$ and $|T_{01,01}|$ show a characteristic monotonic increase and decrease, respectively, with increasing D. Interestingly, $|R_{01,01}|$ and $|T_{01,02}|$ are maximum when D equals 0.24 and 0.30, respectively.

Figure 3.13 gives the reflection and transmission coefficients as the crack length increases. It can be seen that the reflection coefficients, $|R_{01,0n}|$, increase linearly with the crack length, L, – a behavior that is similar to that found in example 1. Note that in this case, however, there are three axisymmetric propagating modes at $\Omega = 3.0$.

Results for the m =1 incident modes are shown in Figure 3.14. A sharp peak can be noticed at the first cutoff frequency. The behavior of the reflection and transmission coefficients is similar, with changes in the crack depth, to the case for $m = 0$. See in Figure 3.15. Finally, the reflection and transmission coefficients for different crack lengths are shown in Figure 3.16. $|R_{11,13}|$ and $|T_{11,12}|$ are much stronger than the other coefficients.

3.5 Concluding Remarks

The scattering of guided waves in a pipe having a planar circumferential crack of arbitrary circumferential length and radial depth is studied by using a novel solution technique. In this technique, only the plane of the crack needs to be discretized by surface elements. This procedure is much less computationally time demanding than a fully two or three dimensional finite element analysis. It is found that the numerical results agree well with available experimental data.

It is shown that the modal representation of scattered and incident fields is sensitive to the length and depth of a planar crack. The proposed method is extended easily to a more complex, composite lay-up in cylindrical pipes, because the semi-analytic finite element method is quite generally applicable. It can be used for arbitrary anisotropy.

In this chapter, planar cracks in a cross section of a circular pipe have been considered. Other types of cracks that appear in pipelines are oriented axially. The method presented here would have to be modified to analyze the wave scattering by such cracks.

Table 3.1: Amplitude of reflection coefficients as a function of the total number of wave modes for $\Omega = 0.74$, $L = 50\%$, $D = 0.50$.

M	N_T	$\lvert R_{02,01}\rvert$	$\lvert R_{02,02}\rvert$	$\lvert R_{02,11}\rvert$	$\lvert R_{02,12}\rvert$	$\lvert R_{02,13}\rvert$
0	51	0.242	0.195	*N/A*	*N/A*	*N/A*
1	131	0.241	0.154	0.161	0.041	0.118
2	211	0.254	0.169	0.155	0.034	0.100
3	291	0.237	0.153	0.151	0.033	0.099
4	371	0.252	0.168	0.152	0.032	0.096
5	451	0.233	0.147	0.149	0.032	0.096
6	531	0.240	0.157	0.150	0.032	0.096
7	611	0.236	0.152	0.149	0.032	0.096
8	691	0.237	0.153	0.149	0.032	0.096
9	771	0.235	0.152	0.149	0.032	0.096
10	851	0.235	0.152	0.149	0.032	0.096
11	931	0.235	0.152	0.149	0.032	0.096

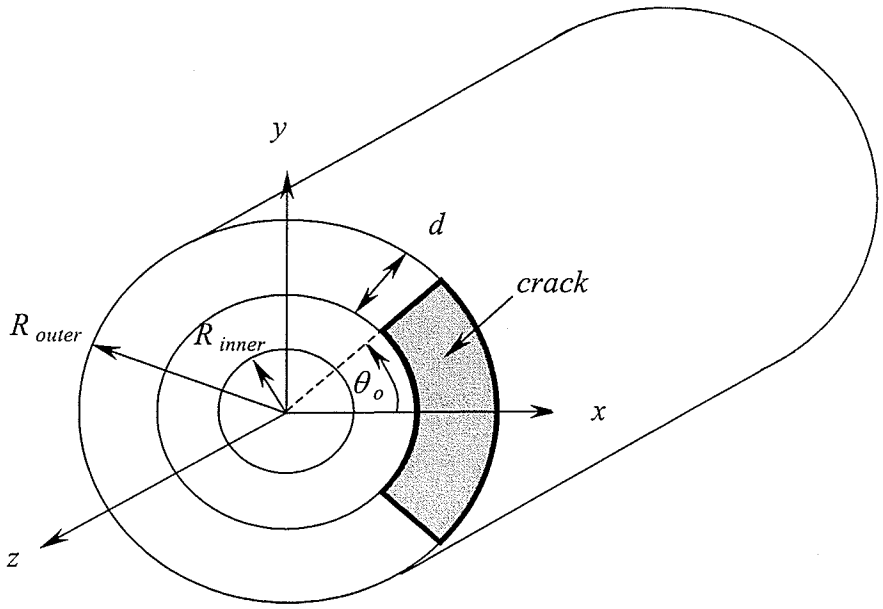

Figure 3.1. Geometry of a pipe. R_{inner}, inner radius; R_{outer}, outer radius; d, crack depth; θ_o, half circumferential crack angle

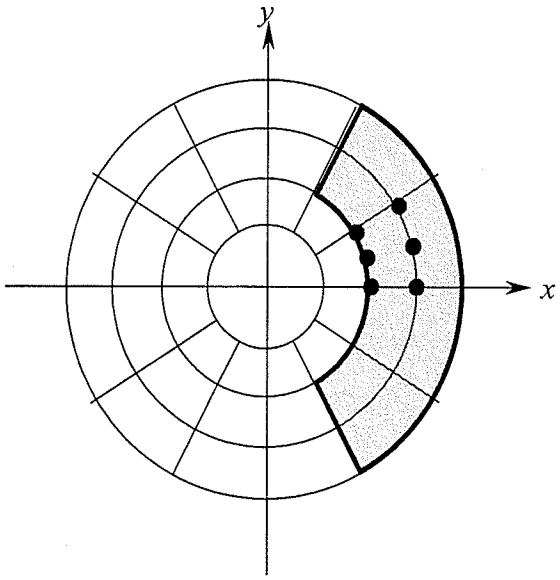

Figure 3.2. A typical mesh in the cross-section containing the crack. The shadow region represents the crack

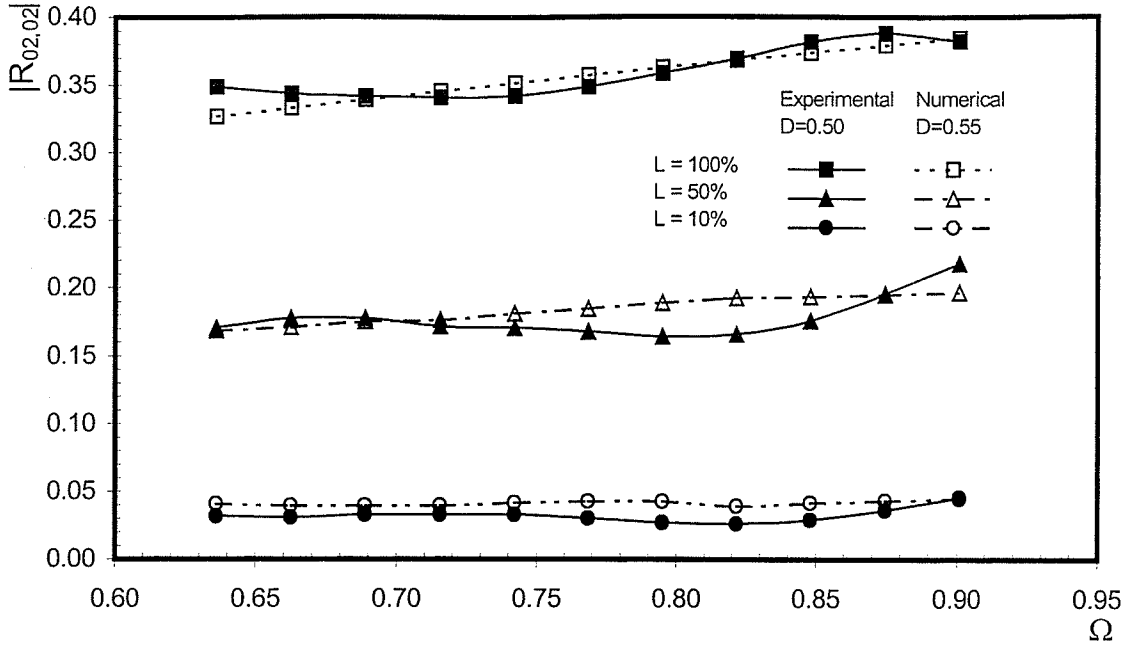

Figure 3.3. Reflection coefficients for three different crack lengths

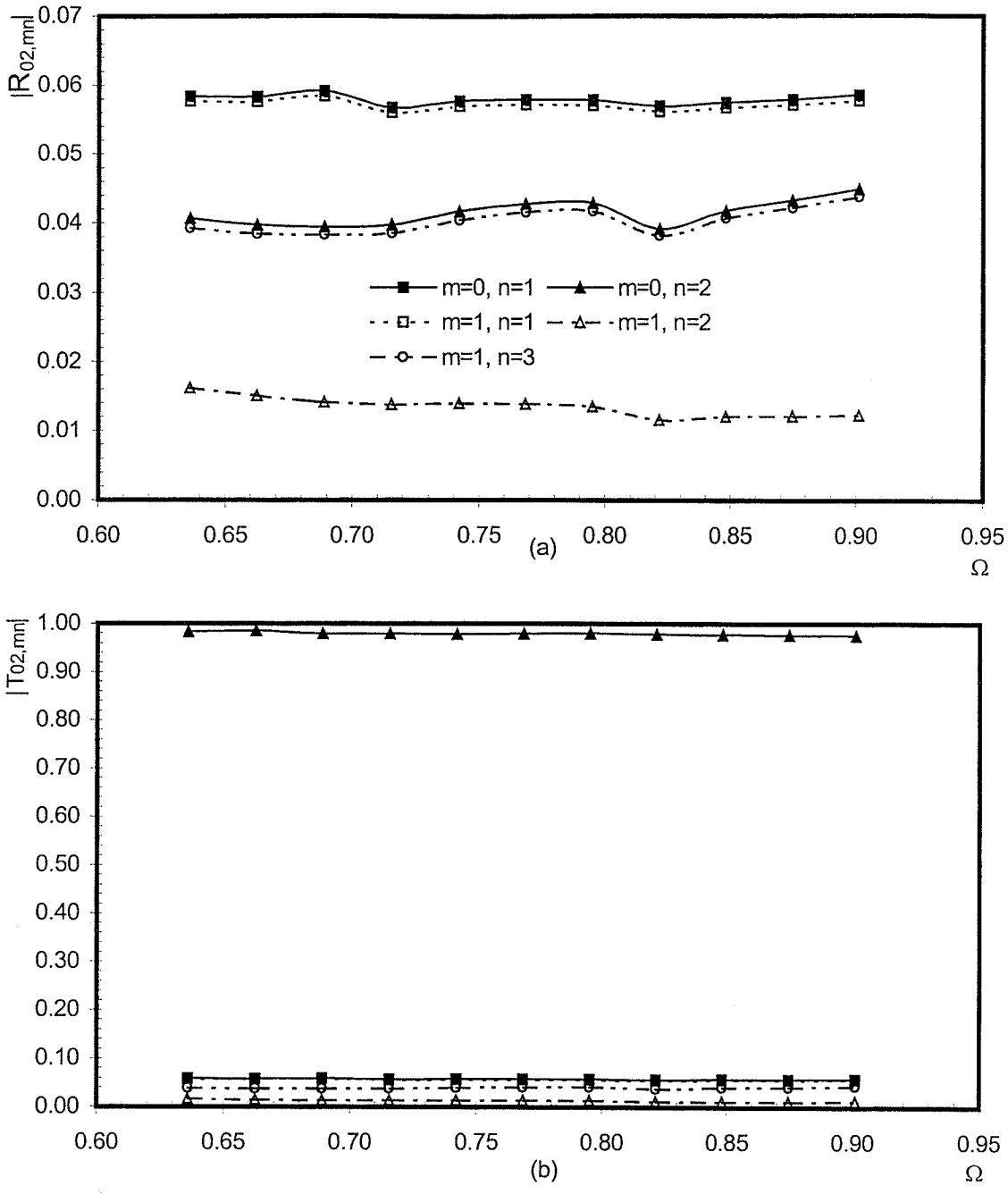

Figure 3.4. Normalized reflection and transmission coefficients in a steel pipe. H/R = 0.135, ν = 0.287, L = 10%, D = 0.55. (a) Reflection coefficient, and (b) transmission coefficient

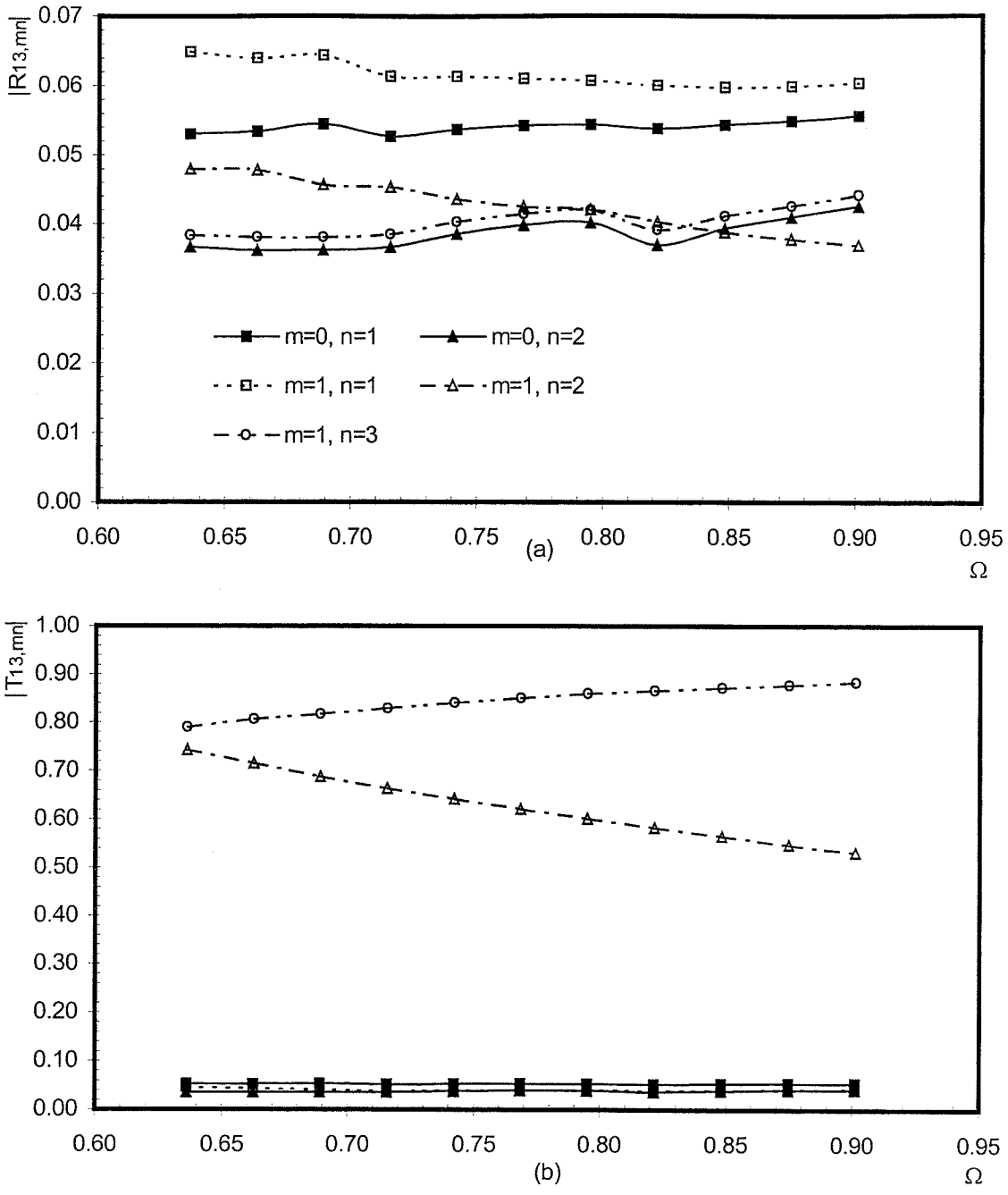

Figure 3.5. Normalized reflection and transmission coefficients in a steel pipe. H/R = 0.135, ν = 0.287, L = 10%, D = 0.55. (a) Reflection coefficient, and (b) transmission coefficient

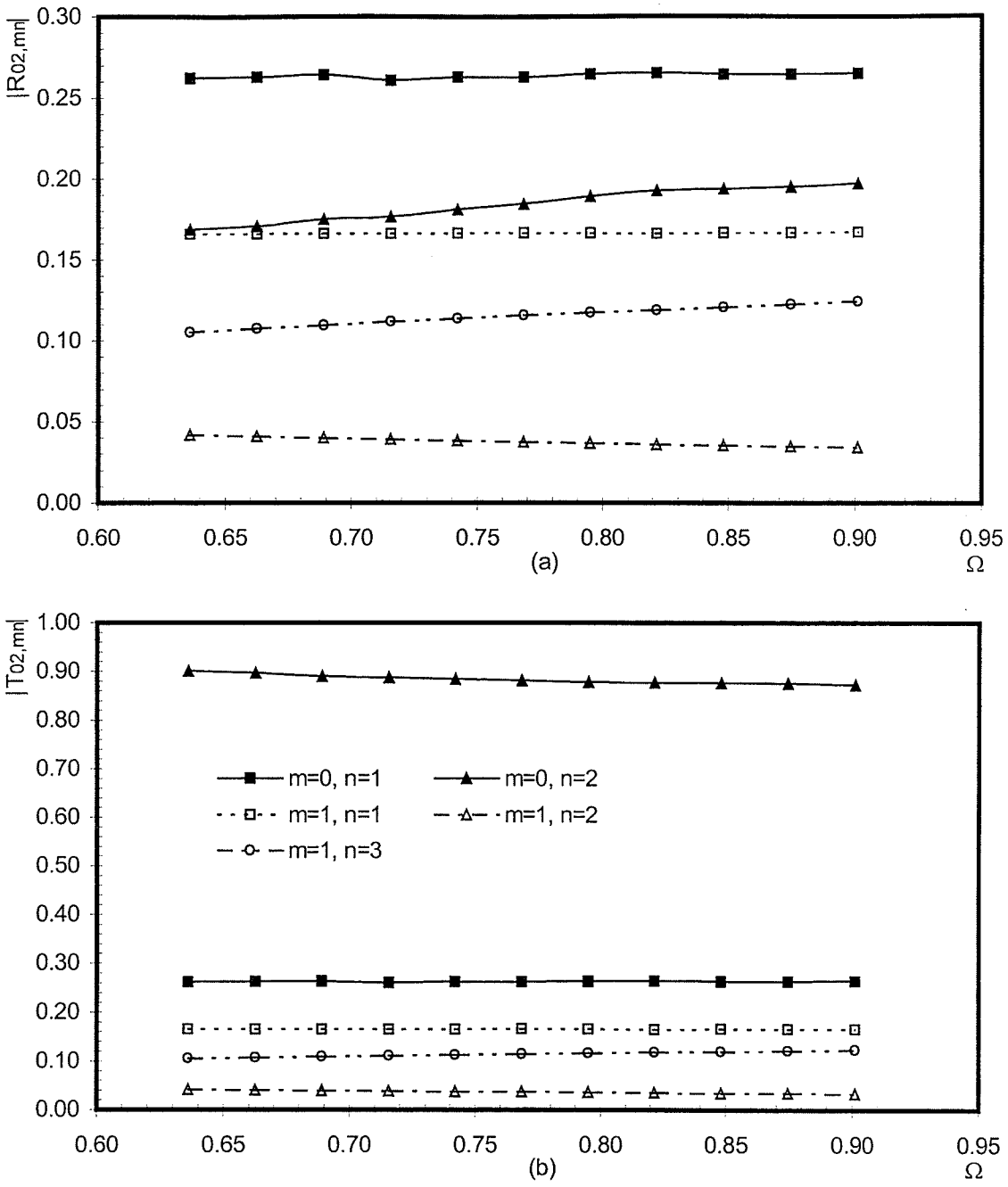

Figure 3.6. Normalized reflection and transmission coefficients in a steel pipe. H/R = 0.135, ν = 0.287, L = 50%, D = 0.55. (a) Reflection coefficient, and (b) transmission coefficient

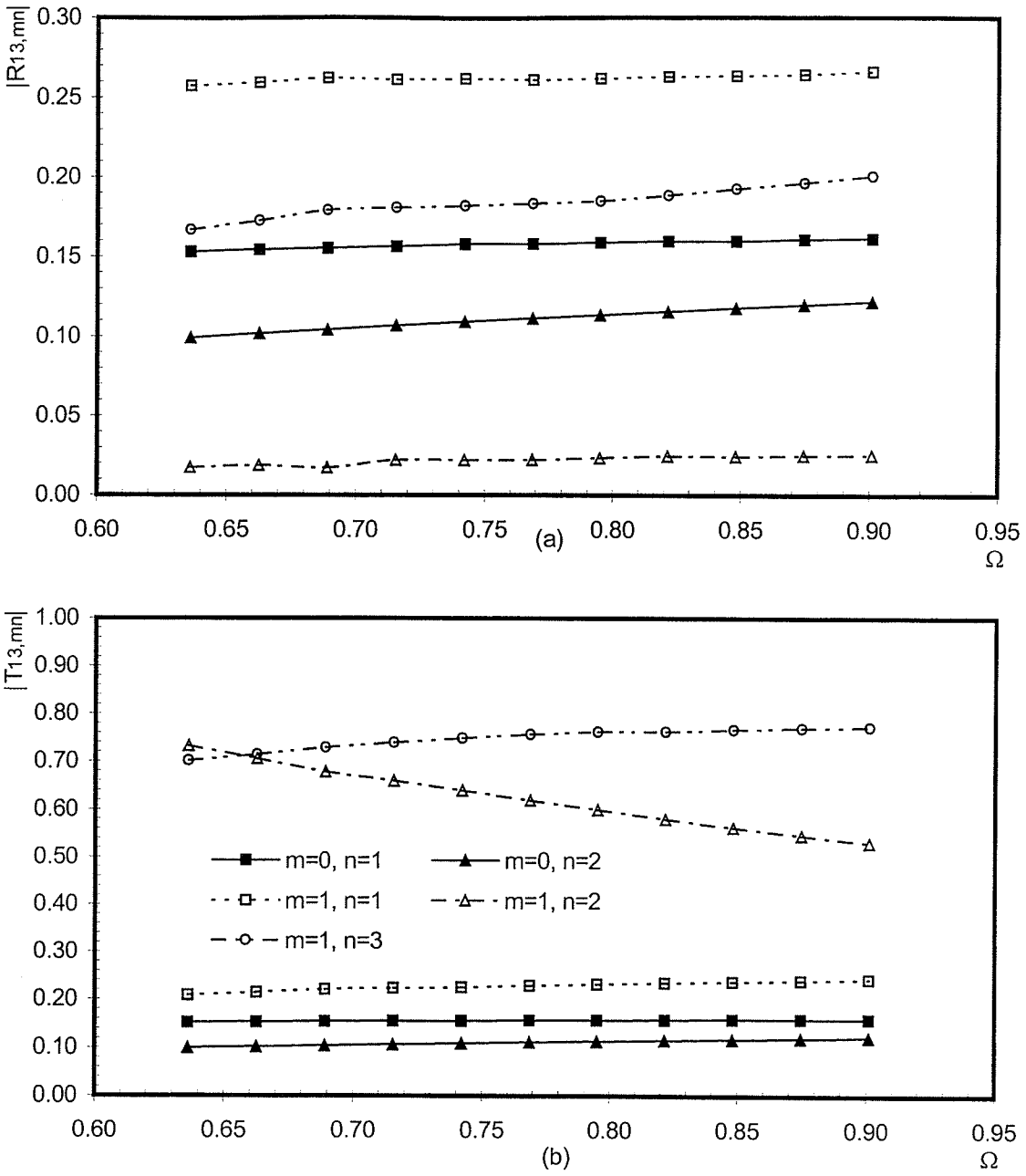

Figure 3.7. Normalized reflection and transmission coefficients in a steel pipe. H/R = 0.135, ν = 0.287, L = 50%, D = 0.55 (a) Reflection coefficient, and (b) transmission coefficient

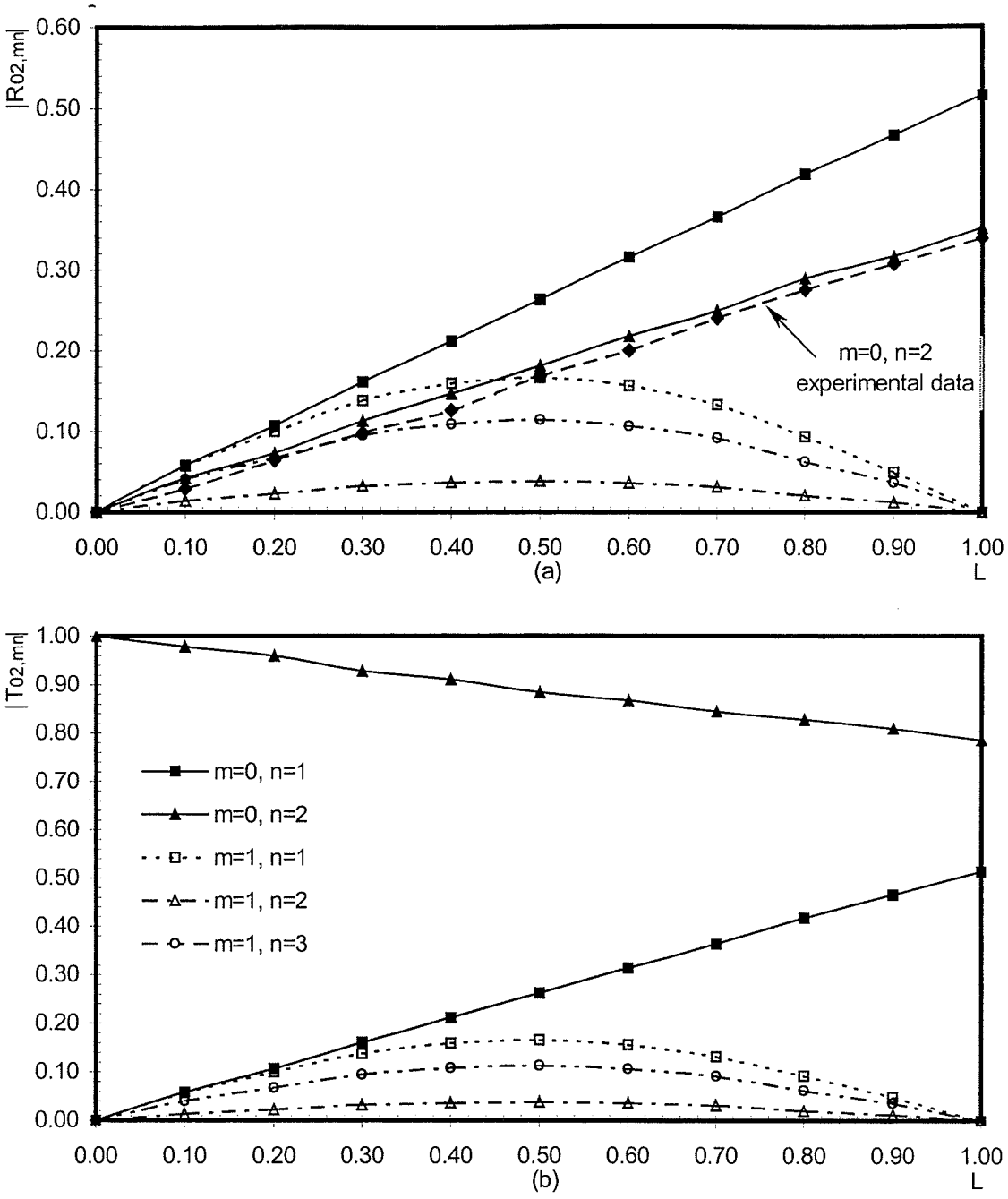

Figure 3.8. Normalized reflection and transmission coefficients in a steel pipe as functions of the crack length at $f = 70$ *kHz*. $H/R = 0.135$, $\nu = 0.287$, $D = 0.55$. (a) Reflection coefficient, and (b) transmission coefficient

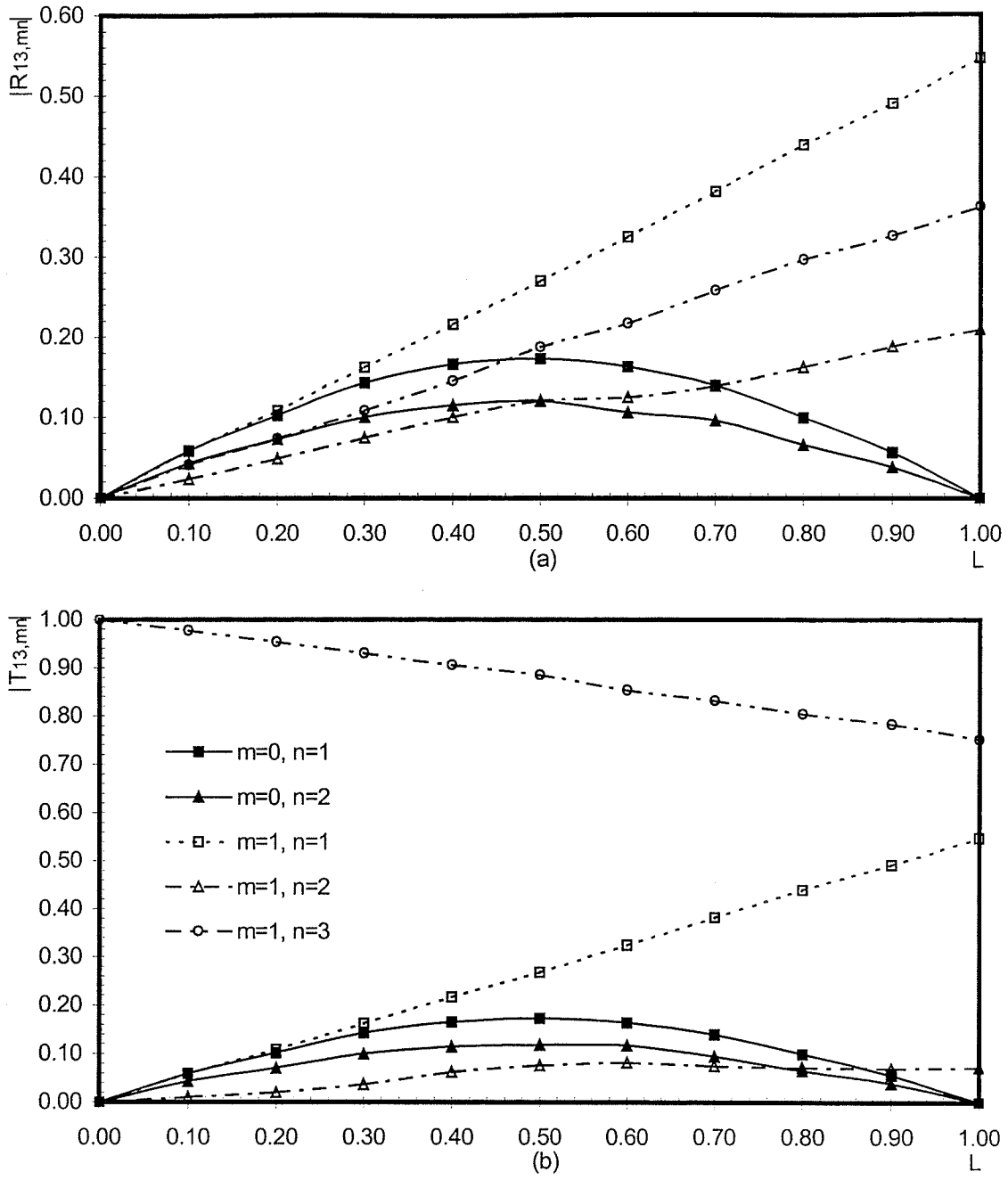

Figure 3.9. Normalized reflection and transmission coefficients in a steel pipe as functions of the crack length at $f = 70$ *kHz*. $H/R = 0.135$, $\nu = 0.287$, $D = 0.55$. (a) Reflection coefficient, and (b) transmission coefficient

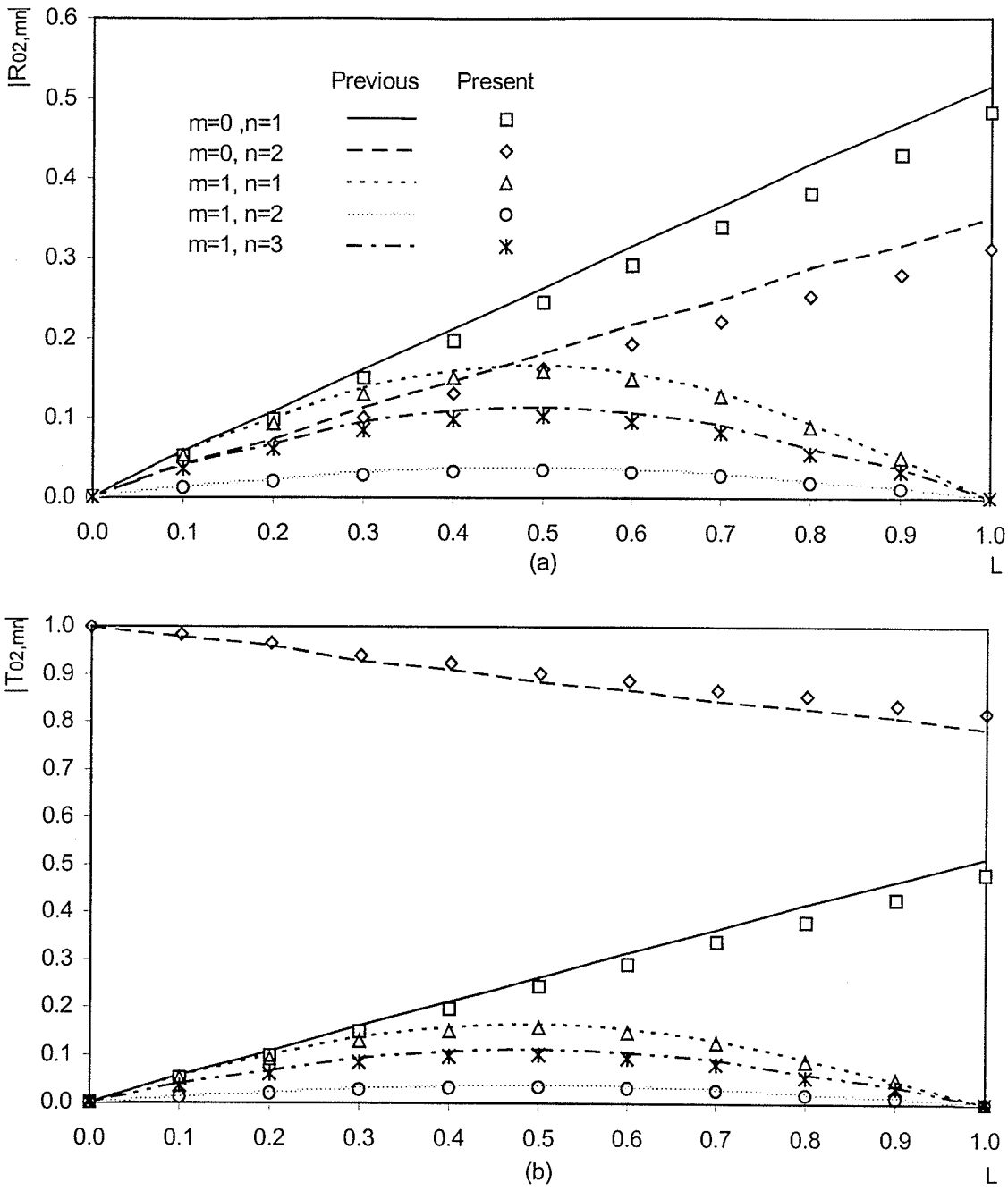

Figure 3.10. Reflection and transmission coefficients, $|R_{02,mn}|$ and $|T_{02,mn}|$, as functions of normalized crack length at frequency, $f = 70KHz$ in a steel pipe. $H/R = 0.135$, $\nu = 0.287$, $D = 0.55$

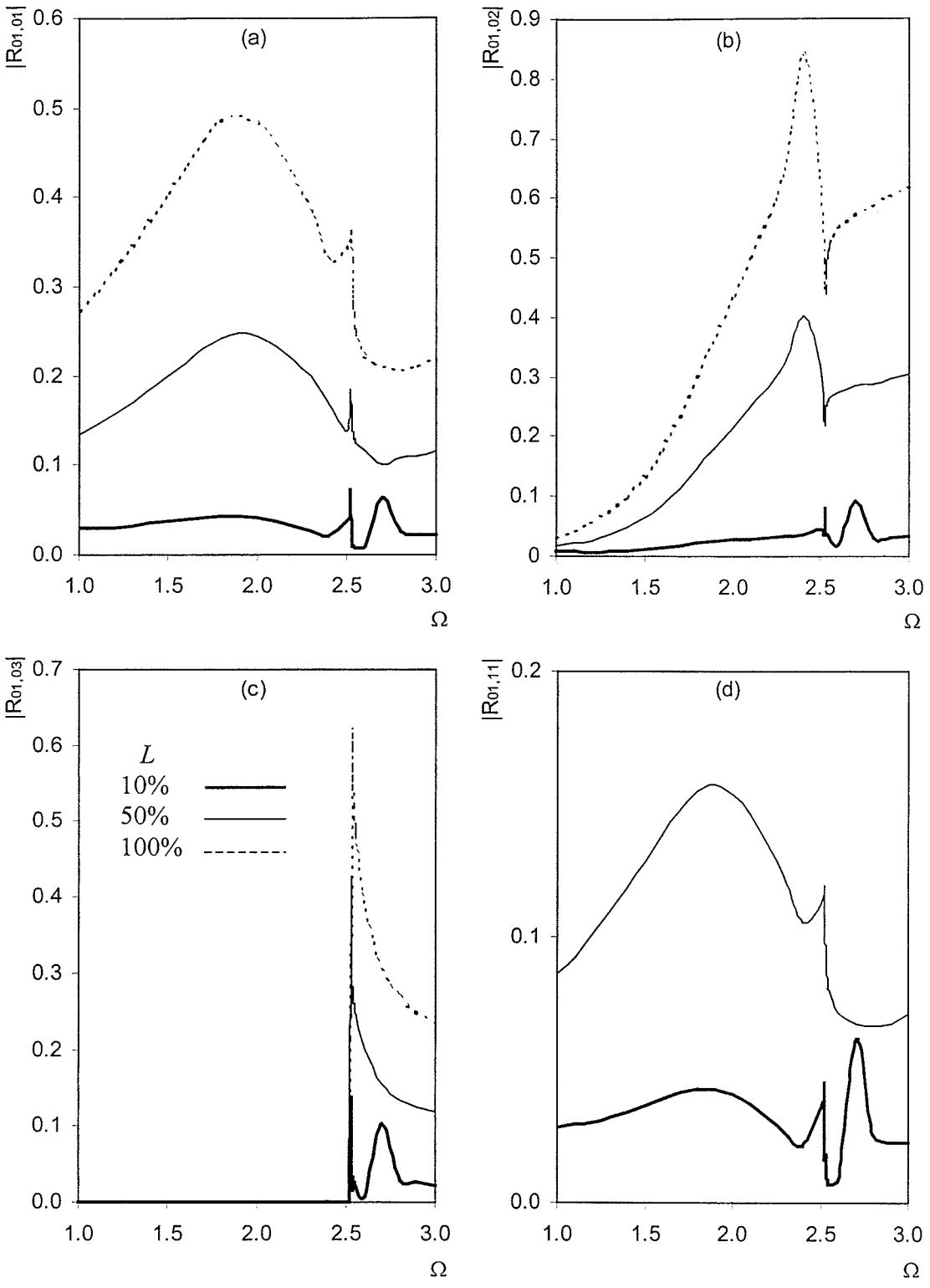

Figure 3.11. Variation of reflection coefficients with different Ω for three normalized crack lengths in a 2-ply [0°/90°] graphite/epoxy cylinder. $H/R = 0.1$, $D = 0.50$. (a) $|R_{01,01}|$, (b) $|R_{01,02}|$, (c) $|R_{01,03}|$, (d) $|R_{01,11}|$

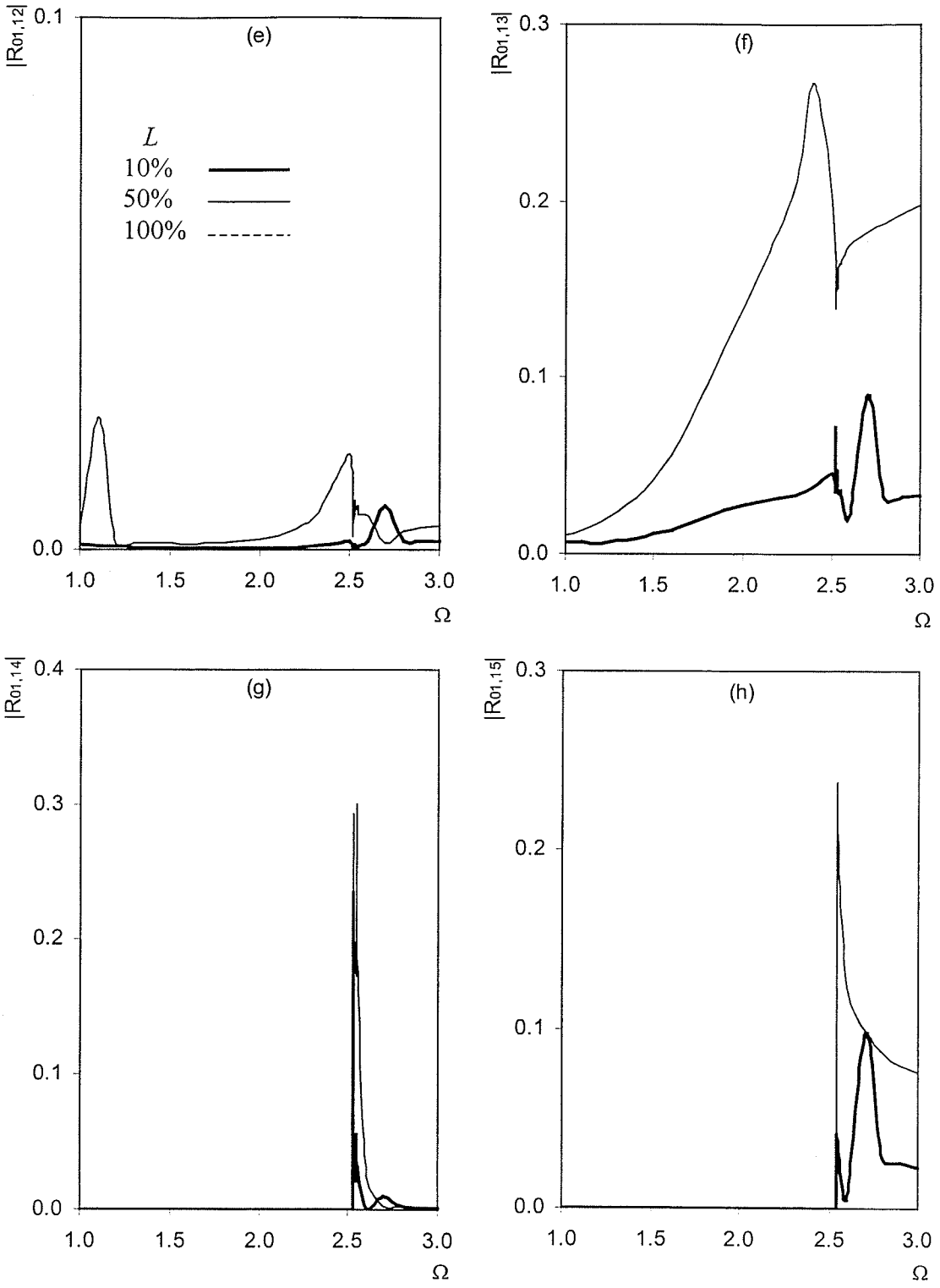

Figure 3.11. Variation of reflection coefficients with different Ω for three normalized crack lengths in a 2-ply [0°/90°] graphite/epoxy cylinder. $H/R = 0.1$, $D = 0.50$. (e) $|R_{01,12}|$, (f) $|R_{01,13}|$, (g) $|R_{01,14}|$, (h) $|R_{01,15}|$

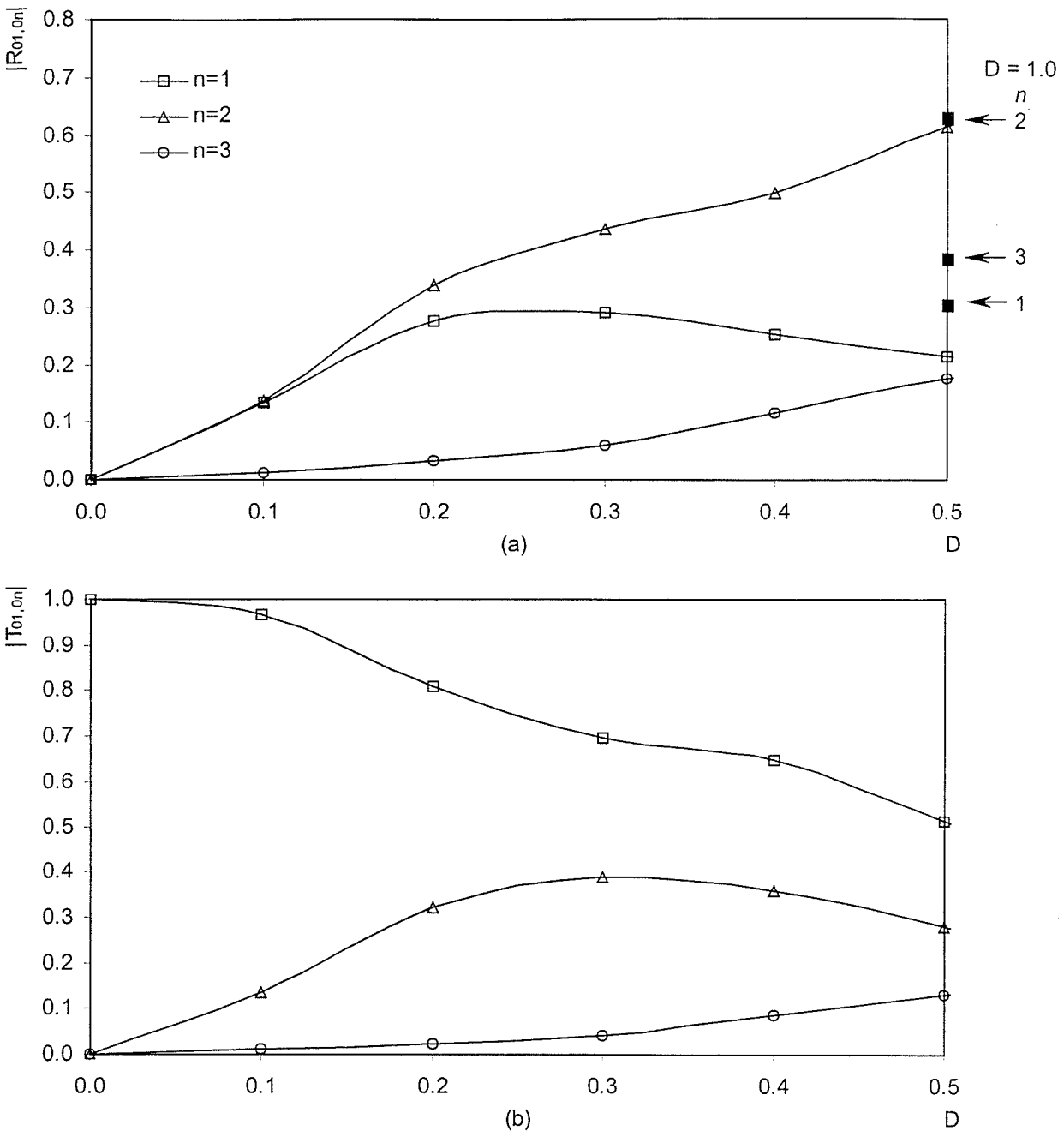

Figure 3.12. Reflection and transmission coefficients, $|R_{01,0n}|$ and $|T_{01,0n}|$, as functions of crack depth in a 2-ply [0/90] graphite/epoxy cylinder at $\Omega = 3.0$. $H/R = 0.1$, $L = 100\%$

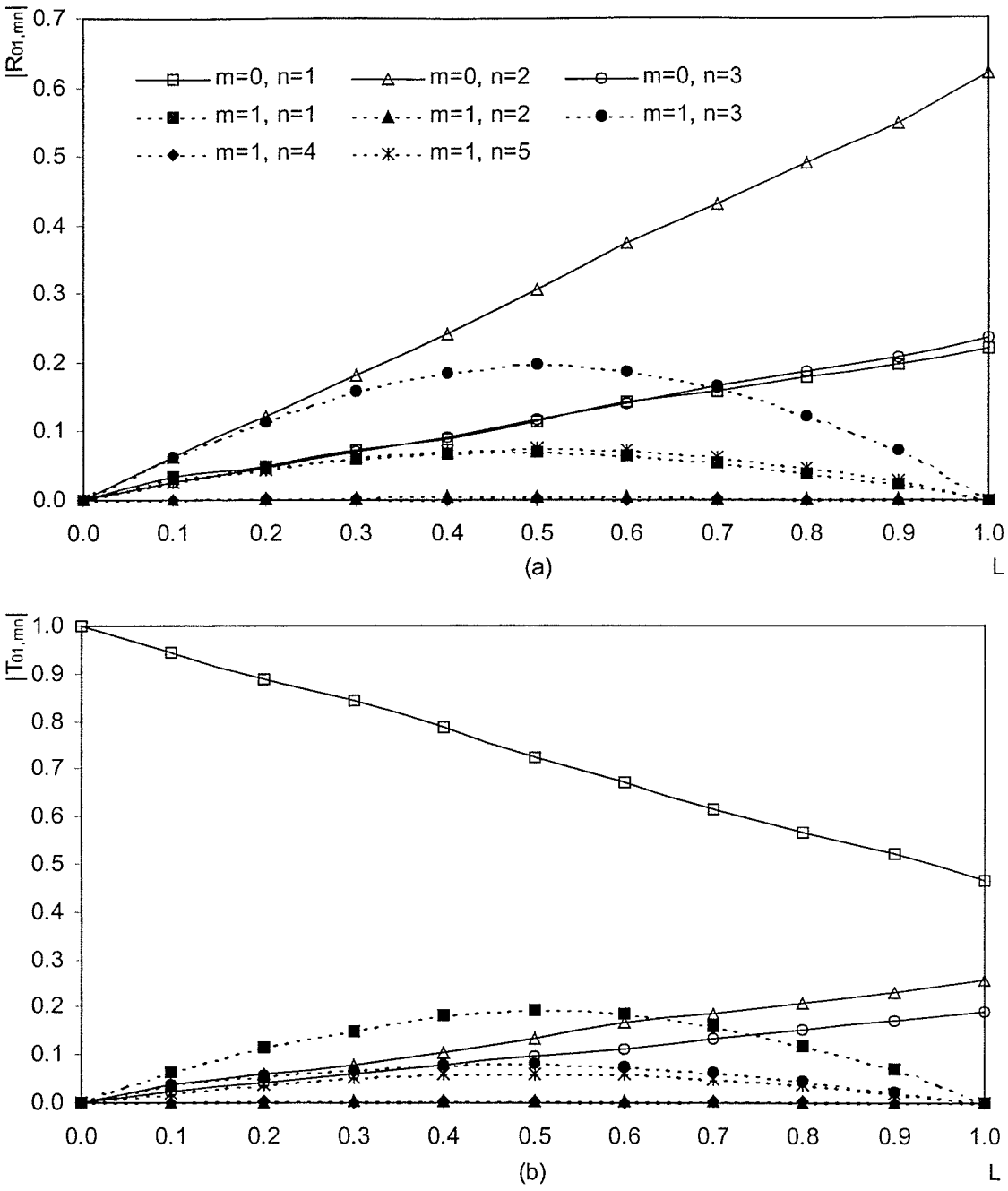

Figure 3.13. Reflection and transmission coefficients, $|R_{01,mn}|$ and $|T_{01,mn}|$, as functions of normalized crack length, L, in a 2-ply [0/90] graphite/epoxy cylinder at $\Omega = 3.0$. $H/R = 0.1$ and $D = 0.5$

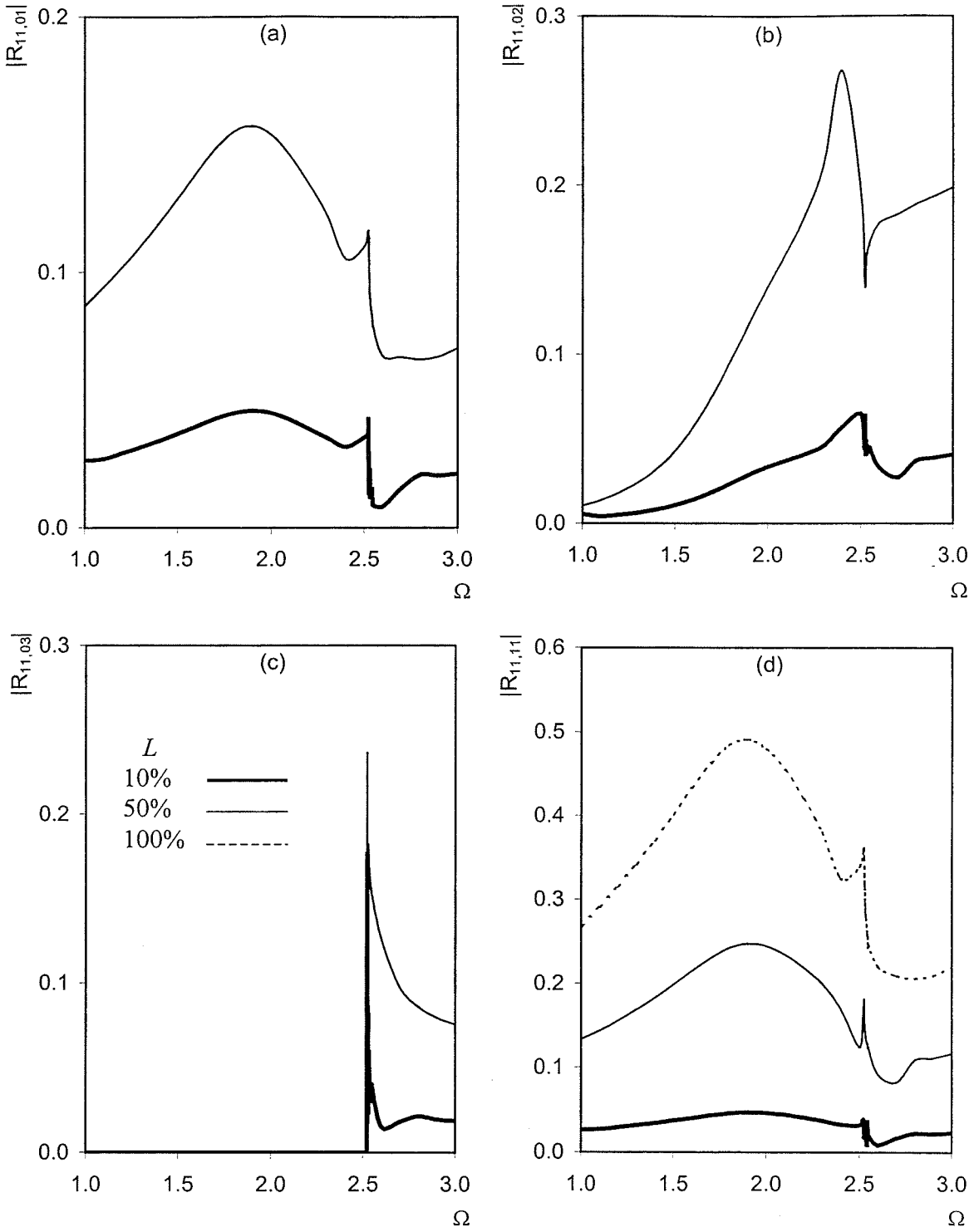

Figure 3.14. Variation of reflection coefficients with different Ω for three normalized crack lengths in a 2-ply [0°/90°] graphite/epoxy cylinder. $H/R = 0.1$, $D = 0.50$. (a) $|R_{11,01}|$, (b) $|R_{11,02}|$, (c) $|R_{11,03}|$, (d) $|R_{11,11}|$

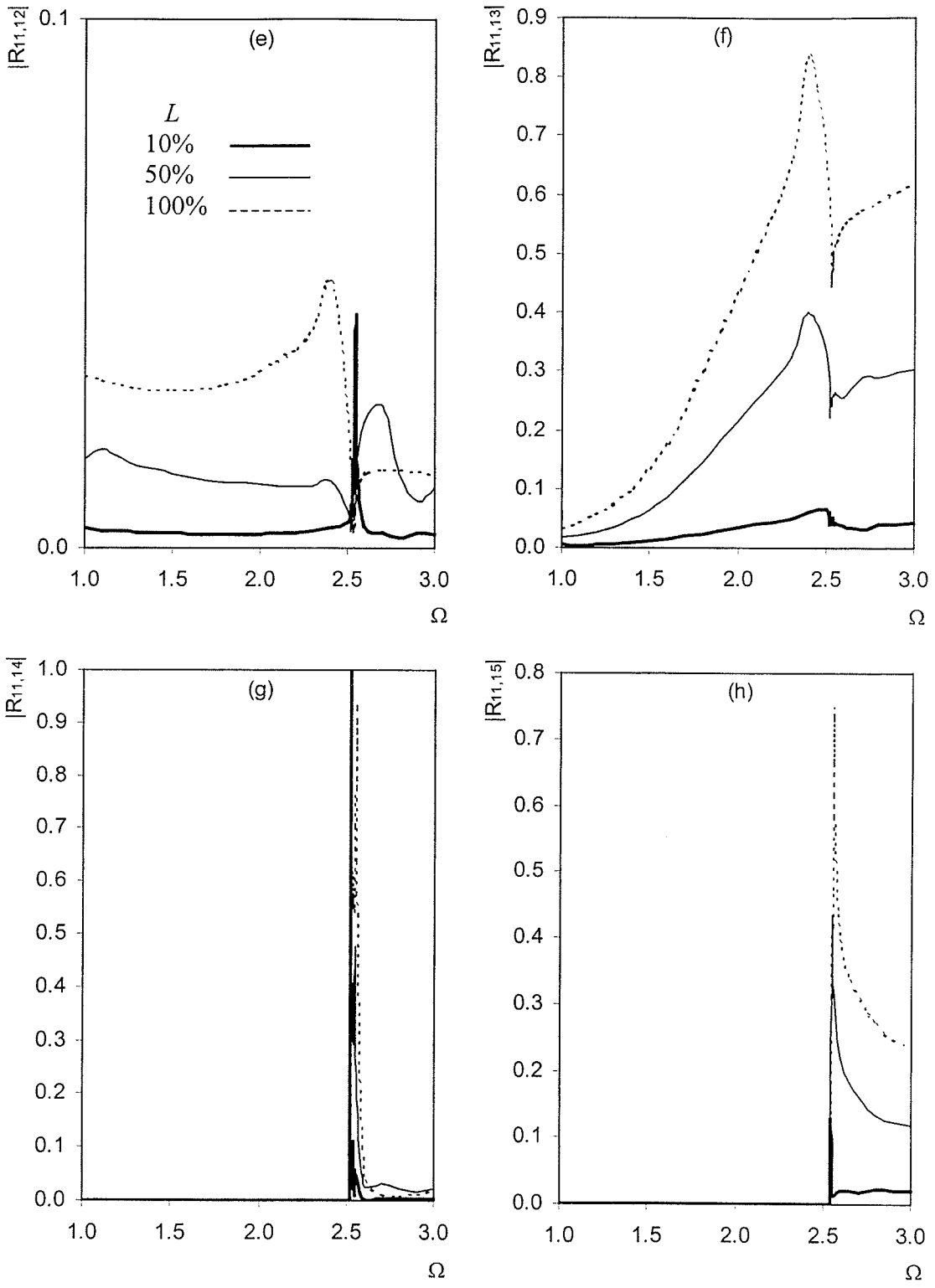

Figure 3.14. Variation of reflection coefficients with different Ω for three normalized crack lengths in a 2-ply [0°/90°] graphite/epoxy cylinder. $H/R = 0.1$, $D = 0.50$. (e) $|R_{11,12}|$, (f) $|R_{11,13}|$, (g) $|R_{11,14}|$, (h) $|R_{11,15}|$

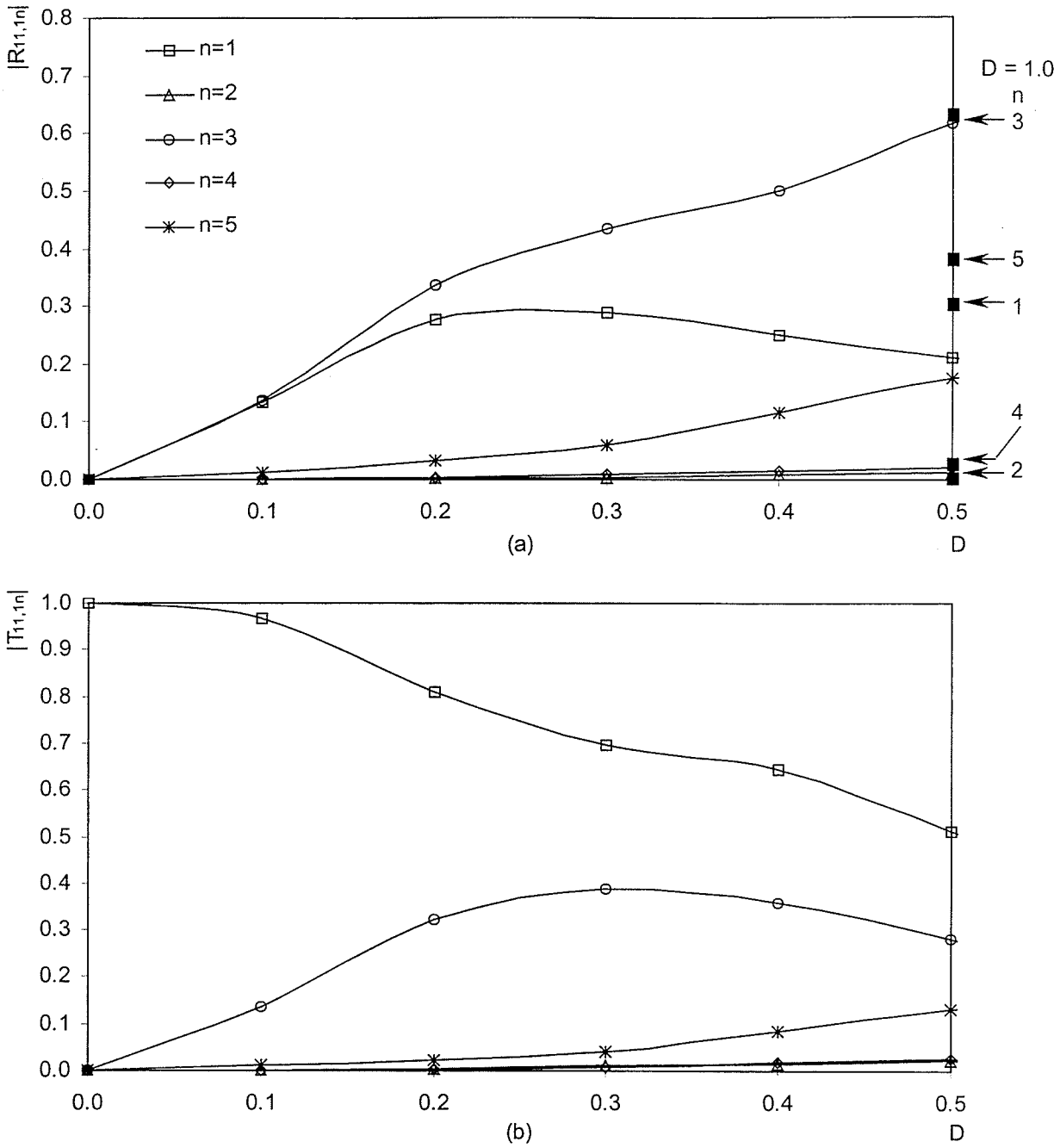

Figure 3.15. Reflection and transmission coefficients, $|R_{11,1n}|$ and $|T_{11,1n}|$, as functions of crack depth in a 2-ply [0°/90°] graphite/epoxy cylinder at $\Omega = 3.0$. H/R = 0.1, L = 100%

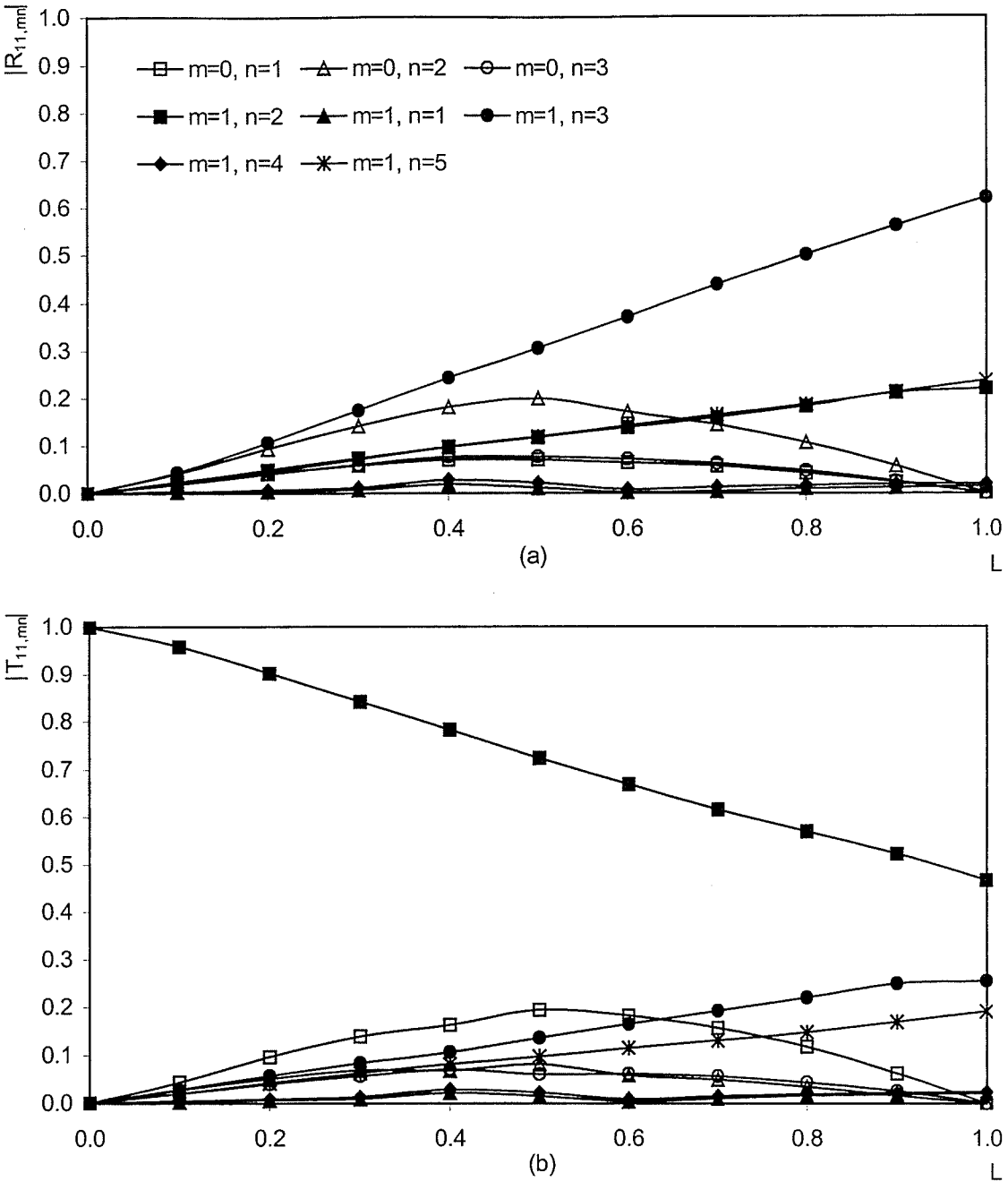

Figure 3.16. Reflection and transmission coefficients, $|R_{11,mn}|$ and $|T_{11,mn}|$, as functions of crack length in a 2-ply [0°/90°] graphite/epoxy cylinder at $\Omega = 3.0$. H/R = 0.1, D = 0.50

Chapter 4

BEM for Wave Scattering in Cylinders

4.1 Introduction

The boundary element method (BEM) is a numerical procedure derived from the integral equations describing an engineering problem. The advantageous reduction by one spatial dimension in a problem's original dimension is the most attractive feature of the BEM compared with the finite element method. Therefore, only boundary surfaces and curves need to be discretized for three and two dimensional problems, respectively. Consequently, in principle, the BEM reduces computational time and increases accuracy. Moreover, there is no need to discretize an infinite or semi-infinite domain because the BEM automatically satisfies radiation boundary conditions if the proper Green's functions are employed. In addition, when Green's functions like those derived in Chapter 2 are used in the BEM, traction-free boundary conditions are satisfied automatically on the inner and outer surfaces of a cylinder. Therefore, the boundary

discretization is simplified further. However, unlike the finite element, the BEM disadvantageously produces equations whose corresponding matrices are fully populated and non-symmetrical.

4.2 Formulation

Consider a linearly elastic body of volume V bounded by a regular surface, S. The boundary integral equation is given in the frequency domain by (Brebbia, 1984),

$$c_{ij}(\mathbf{y})u_j(\mathbf{y}) = \int_S \left[G_{ij}(\mathbf{x};\mathbf{y})t_j(\mathbf{x}) - H_{ij}(\mathbf{x};\mathbf{y})u_j(\mathbf{x})\right]dS(\mathbf{x}) + \int_V G_{ij}(\mathbf{x};\mathbf{y})b_j(\mathbf{x})dV(\mathbf{x}) \quad (4.1)$$

where $u_i(\mathbf{x})$ and $t_i(\mathbf{x})$ (i = 1, 2, 3) are the boundary displacements and tractions, respectively, and $b_i(\mathbf{x})$ (i = 1, 2, 3) are the body forces. $G_{ij}(\mathbf{x};\mathbf{y})$ and $H_{ij}(\mathbf{x};\mathbf{y})$ represent the displacement and traction Green's functions, respectively, in the j direction at location $\mathbf{x}$ when a unit point load applied at point $\mathbf{y}$ in the i direction. The $c_{ij}(\mathbf{y})$ is a discontinuity term that is defined as,

$$c_{ij}(\mathbf{y}) = \begin{cases} \delta_{ij}, \text{ when } \mathbf{y} \in V \text{ and } \mathbf{y} \notin S \\ \frac{1}{2}\delta_{ij}, \text{ when } \mathbf{y} \in S \\ 0, \text{ when } \mathbf{y} \notin V \text{ and } \mathbf{y} \notin S \end{cases} \quad (4.2)$$

where δ_{ij} (i, j = 1, 2, 3) is the Kronecker delta.

There is generally no analytical solution for equation (4.1). A numerical solution procedure for equation (4.1) usually involves the following steps.

1. Boundary S is discretized into a series of elements, as illustrated in Figure 4.1, over which the displacements and tractions are chosen to permit a piecewise interpolation between nodal points of the boundary elements.

2. Equation (4.1) is applied, in a discretized form, to each nodal point, **y**, of boundary S. The integrals are computed usually by using a numerical quadrature scheme over each boundary element. Then a system of linear algebraic equations is obtained that involve the nodal tractions and displacements.
3. Boundary conditions are imposed so that the nodal values of the traction or displacement are prescribed in each direction at a node. The ensuing equations can be solved by utilizing standard methods so that the remaining boundary data can be found.
4. Calculate the required displacements and forces at specified (nodal) points in domain V by using equation (4.1).

For three dimensional wave scattering in a cylinder, the boundary surface is discretized into a number of quadrilateral elements, N. (See Figure 4.2.) Using the isoparametric element methodology (Bathe, 1982), the approximation of the boundary displacement and traction is given, for a typical element, by,

$$u_i(\mathbf{x}) = \sum_{\alpha=1}^{l} h_\alpha^e(\xi,\eta) u_{i,\alpha}, \quad t_i(\mathbf{x}) = \sum_{\alpha=1}^{l} h_\alpha^e(\xi,\eta) t_{i,\alpha} \tag{4.3}$$

in terms of the local variables $-1 \leq \xi$ and $\eta \leq 1$. Therefore, ξ_α and η_α are the local coordinates of node number α. The $u_{i,\alpha}$ and $t_{i,\alpha}$ are the node displacement and traction, respectively. $h_\alpha^e(\xi,\eta)$ is the interpolation function and l is the number of nodes in an element. The coordinate transformation is given by

$$\mathbf{x} = \sum_{\alpha=1}^{l} h_\alpha^e(\xi,\eta)\mathbf{x}_\alpha \tag{4.4}$$

where $\mathbf{x}_\alpha$ corresponds to the node coordinates in the global coordinate system. Thus, for a function f, the general transformation is,

$$\begin{Bmatrix} \frac{\partial f}{\partial \xi} \\ \frac{\partial f}{\partial \eta} \\ \frac{\partial f}{\partial \varsigma} \end{Bmatrix} = \begin{bmatrix} \frac{\partial x}{\partial \xi} & \frac{\partial y}{\partial \xi} & \frac{\partial z}{\partial \xi} \\ \frac{\partial x}{\partial \eta} & \frac{\partial y}{\partial \eta} & \frac{\partial z}{\partial \eta} \\ \frac{\partial x}{\partial \varsigma} & \frac{\partial y}{\partial \varsigma} & \frac{\partial z}{\partial \varsigma} \end{bmatrix} \begin{Bmatrix} \frac{\partial f}{\partial x} \\ \frac{\partial f}{\partial y} \\ \frac{\partial f}{\partial z} \end{Bmatrix} = \mathbf{J} \begin{Bmatrix} \frac{\partial f}{\partial x} \\ \frac{\partial f}{\partial y} \\ \frac{\partial f}{\partial z} \end{Bmatrix}. \tag{4.5}$$

The partial derivatives of the Jacobi matrix, **J**, are all calculated from relation (4.4).

With the help of the above relations, the differential volume and surface area are given by,

$$dV = \left|\det(\mathbf{J})\right| d\xi d\eta d\varsigma \text{ and } dS = |\mathbf{S}| d\xi d\eta \tag{4.6}$$

where vector **S** is given by,

$$\mathbf{S} = \{s_1, s_2, s_3\} \tag{4.7}$$

$$\begin{aligned} s_1 &= \frac{\partial y}{\partial \xi}\frac{\partial z}{\partial \eta} - \frac{\partial z}{\partial \xi}\frac{\partial y}{\partial \eta} \\ s_2 &= \frac{\partial z}{\partial \xi}\frac{\partial x}{\partial \eta} - \frac{\partial x}{\partial \xi}\frac{\partial z}{\partial \eta} \\ s_3 &= \frac{\partial x}{\partial \xi}\frac{\partial y}{\partial \eta} - \frac{\partial y}{\partial \xi}\frac{\partial x}{\partial \eta} \end{aligned} \tag{4.8}$$

and

$$|\mathbf{S}| = \sqrt{s_1^2 + s_2^2 + s_3^2}\,. \tag{4.9}$$

The discretized version of equation (4.1) is given, for a boundary node **y**, by,

$$\begin{aligned} c_{ij}(\mathbf{y})u_j(\mathbf{y}) + \sum_{n=1}^{N}\sum_{\alpha=1}^{l} \iint_{-1\le\xi,\eta\le 1} H_{ij}(\xi,\eta,0;\mathbf{y}) h_\alpha^e(\xi,\eta) u_{j,\alpha} |\mathbf{S}| d\xi d\eta \\ = \sum_{n=1}^{N}\sum_{\alpha=1}^{l} \iint_{-1\le\xi,\eta\le 1} G_{ij}(\xi,\eta,0;\mathbf{y}) h_\alpha^e(\xi,\eta) t_{j,\alpha} |\mathbf{S}| d\xi d\eta + b_i^e(\mathbf{y}), \quad i,j = 1,2,3 \end{aligned} \tag{4.10}$$

where N is the number of elements, $b_i^e(\mathbf{y})$ is the contribution of the body force from the last integral in equation (4.1) and $|\mathbf{S}|$ is given in equation (4.9).

Three linear equations are obtained from equation (4.10) for each boundary node, **y**. The application of this equation to all the boundary nodes results in equations whose matrix form is given by,

$$\mathbf{Hu} = \mathbf{Gt} + \mathbf{b}\,. \tag{4.11}$$

The vector **u** corresponds to the boundary node displacements, **t** involves the boundary node tractions and matrix **H** contains the $c_{ij}(\mathbf{y})$ tensor as well as the traction kernel integrals. Matrix **G** contains the displacement kernel integrals. Moreover, **H** and **G** are composed of block, three by three matrix elements, $\mathbf{H}_{ij}$ and $\mathbf{G}_{ij}$, respectively, so that,

$$\mathbf{H} = \begin{bmatrix} \mathbf{H}_{11} & \mathbf{H}_{12} & \cdots & \mathbf{H}_{1n} \\ \mathbf{H}_{21} & \mathbf{H}_{22} & \cdots & \mathbf{H}_{2n} \\ \vdots & \vdots & \ddots & \vdots \\ \mathbf{H}_{n1} & \mathbf{H}_{n2} & \cdots & \mathbf{H}_{nn} \end{bmatrix} \text{ and } \mathbf{G} = \begin{bmatrix} \mathbf{G}_{11} & \mathbf{G}_{12} & \cdots & \mathbf{G}_{1n} \\ \mathbf{G}_{21} & \mathbf{G}_{22} & \cdots & \mathbf{G}_{2n} \\ \vdots & \vdots & \ddots & \vdots \\ \mathbf{G}_{n1} & \mathbf{G}_{n2} & \cdots & \mathbf{G}_{nn} \end{bmatrix}. \tag{4.12}$$

Each row block corresponds to one boundary node and n is the total number of boundary nodes.

The boundary conditions of the problem are given by (i) $\mathbf{u}_i = \hat{\mathbf{u}}_i$ on S_u and (ii) $\mathbf{t}_i = \hat{\mathbf{t}}_i$ on S_t. If the displacements are known, equation (4.11) can be used to find the tractions and vice versa. If mixed boundary conditions are given, the system of equations (4.11) can be reordered so that all the unknowns are on the left-hand side of the equation. Therefore, the solution of the reordered equations gives the unknown displacements and tractions.

4.3 Special Considerations

4.3.1 Evaluation of CPV and Weakly Singular Integrals

It is well known that the boundary integral equation (4.1) contains singular integrals when the source point, **y**, is on the boundary of the domain. The diagonal 3×3 block matrix, $\mathbf{H}_{ii}$, of the **H** matrix contains the tensor c_{ij} as well as the Cauchy principal value (CPV) integral of the traction kernel. The $\mathbf{G}_{ii}$ of matrix **G**, on the other hand, contains weakly singular, displacement kernel integrals. The accurate evaluation of these singular integrals is the key for the successful use of the BEM. Zhu (1996) and Zhu et al. (1996) developed a numerical procedure that indirectly but simultaneously evaluates the CPV and weakly singular integrals in a way similar to the rigid-body-movement method (Cruse, 1974 and 1988). However, this technique is designed for the BEM without the use of the full space Green's functions. Zhuang (1998) applied the method to axisymmetrical wave scattering in cylinders.

The advantage of the numerical approach of Zhu (1996) and Zhu et al. (1996) lies in using a far-field value of the Green's function instead of the value in the near field. It is well known that numerical values are unreliable around the source point. They are much more accurate in the far field. This replacement makes the approach not only stable but also more accurate. Note that the **H** and **G** matrices do not change with the alteration of the body forces. Therefore once **H** and **G** are formed, they can be used for solving different problems if the domain and boundary element distribution is unchanged.

The numerical approach starts with the concept of artificial sources (usually, point loads). Assume that an artificial source is applied in the interior of the domain and that

the displacement and traction Green's functions can be computed at any boundary node by using the methods presented in Chapter 2. These tractions, together with the artificial sources, form a complete boundary value problem. If (i) the boundary value problem is solved with the BEM and the same discretization, and (ii) the CPV and weakly singular integrals are evaluated accurately, then it is expected that the boundary displacements should be identical to those from the displacement Green's function. Consider this problem in a different way. For every boundary node i, assume that the diagonal 3×3 matrices $\mathbf{H}_{ii}$ (h_{pq}, p, $q = i$, i+1, i+2) and $\mathbf{G}_{ii}$ (g_{pq}, p, $q = i$, i+1, i+2) are not known but that the displacement and traction are known. The boundary integral equation (4.11) takes the form, for a single node i,

$$\begin{aligned}
h_{i,i}u_i + h_{i,i+1}u_{i+1} + h_{i,i+2}u_{i+2} - g_{i,i}t_i &= -\sum_{j\neq i,i+1,i+2} h_{i,j}u_j + \sum_{j\neq i} g_{i,j}t_j + b_i \\
h_{i+1,i}u_i + h_{i+1,i+1}u_{i+1} + h_{i+1,i+2}u_{i+2} - g_{i+1,i+1}t_{i+1} &= -\sum_{j\neq i,i+1,i+2} h_{i+1,j}u_j + \sum_{j\neq i+1} g_{i+1,j}t_j + b_{i+1} \\
h_{i+2,i}u_i + h_{i+2,i+1}u_{i+1} + h_{i+2,i+2}u_{i+2} - g_{i+2,i+2}t_{i+2} &= -\sum_{j\neq i,i+1,i+2} h_{i+2,j}u_j + \sum_{j\neq i+2} g_{i+2,j}t_j + b_{i+2}
\end{aligned} \tag{4.13}$$

where u_i and t_i are the displacement and traction Green's functions due to the artificial sources. The $h_{p,j}$ and $g_{p,j}$ ($p = i$, i+1, i+2) at the right side of equation (4.13) are derived from regular integrals because all the singular integrals are contained in h_{pq} and g_{pp} (p, $q = i$, i+1, i+2). There are three equations and twelve unknown h_{pq} and g_{pq} (p, $q = i$, i+1, i+2) in equation (4.13) that come from one artificial source. By selecting three more artificial sources, a system of linear equations can be formulated for the twelve unknowns as,

$$\begin{bmatrix} u_i^1 & u_{i+1}^1 & u_{i+2}^1 & -t_i^1 \\ u_i^2 & u_{i+1}^2 & u_{i+2}^2 & -t_i^2 \\ u_i^3 & u_{i+1}^3 & u_{i+2}^3 & -t_i^3 \\ u_i^4 & u_{i+1}^4 & u_{i+2}^4 & -t_i^4 \end{bmatrix} \begin{Bmatrix} h_{i,i} & h_{i+1,i} & h_{i+2,i} \\ h_{i,i+1} & h_{i+1,i+1} & h_{i+2,i+1} \\ h_{i,i+2} & h_{i+1,i+2} & h_{i+2,i+2} \\ g_{i,i} & g_{i+1,i} & g_{i+2,i} \end{Bmatrix} = \begin{Bmatrix} r_i^1 & r_{i+1}^1 & r_{i+2}^1 \\ r_i^2 & r_{i+1}^2 & r_{i+2}^2 \\ r_i^3 & r_{i+1}^3 & r_{i+2}^3 \\ r_i^4 & r_{i+1}^4 & r_{i+2}^4 \end{Bmatrix}. \tag{4.14}$$

The u_i^n, u_{i+1}^n and u_{i+2}^n ($n = 1, 2, 3, 4$) are the displacement components at node i due to the *nth* artificial source, t_i^n, t_{i+1}^n and t_{i+2}^n are the corresponding tractions. On the other hand, r_i^n, r_{i+1}^n and r_{i+2}^n are evaluated by substituting the displacement and traction of the n^{th} artificial source in the right side of equation (4.13).

4.3.2 Corner Points

When the boundary surface of a domain is not always smooth, special consideration must be given to the non-smooth surface points because the normal of the surface has a jump and the tractions are discontinuous at a corner. This discontinuity makes the computation of the singular integrals more difficult. The numerical procedure presented in the last section can still be used, however, for discontinuous normals by incorporating the double node technique illustrated in Figure 4.3. Here, the i and j nodes have the same spatial position.

4.3.3 Degeneration of the BEM in Crack Problems

An ideal mathematical crack is composed of two surfaces that occupy the same spatial positions, as shown in Figure 4.4. The displacement at an internal point, $\mathbf{y}$, is given by (see equation (4.1)),

$$u_i(\mathbf{y}) = \int_{S+\Gamma^+ +\Gamma^-} \left[G_{ij}(\mathbf{x};\mathbf{y}) t_j(\mathbf{x}) - H_{ij}(\mathbf{x};\mathbf{y}) u_j(\mathbf{x}) \right] dS(\mathbf{x}) \tag{4.15}$$

when no body forces are present. In the last equation, Γ^+ and Γ^- correspond to the upper and lower crack surfaces which have normals $\boldsymbol{n}^+$ and $\boldsymbol{n}^-$, respectively. These two surfaces

are defined, in the limit, as Γ whose normal is $\boldsymbol{n}^+$. The displacement and traction Green's functions at the upper and lower crack surfaces satisfy,

$$G_{ij}\left(\mathbf{x}^+;\mathbf{y}\right)=G_{ij}\left(\mathbf{x}^-;\mathbf{y}\right),\quad H_{ij}\left(\mathbf{x}^+;\mathbf{y}\right)=-H_{ij}\left(\mathbf{x}^-;\mathbf{y}\right),\quad \mathbf{x}^+\in\Gamma^+,\quad \mathbf{x}^-\in\Gamma^-. \tag{4.16}$$

The change in sign of H_{ij} is due to the change in the direction of the normals of the upper and lower crack surfaces.

Define the following two quantities next,

$$\Sigma t_j\left(\mathbf{x}\right)=t_j\left(\mathbf{x}^+\right)+t_j\left(\mathbf{x}^-\right),\quad \Delta u_j\left(\mathbf{x}\right)=u_j\left(\mathbf{x}^+\right)-u_j\left(\mathbf{x}^-\right),\quad \mathbf{x}\in\Gamma. \tag{4.17}$$

Then equation (4.15) becomes, in the limit,

$$\begin{aligned} u_i\left(\mathbf{y}\right)=&\int_S\left[G_{ij}\left(\mathbf{x};\mathbf{y}\right)t_j\left(\mathbf{x}\right)-H_{ij}\left(\mathbf{x};\mathbf{y}\right)u_j\left(\mathbf{x}\right)\right]dS\left(\mathbf{x}\right)+\\ &\int_\Gamma\left[G_{ij}\left(\mathbf{x};\mathbf{y}\right)\Sigma t_j\left(\mathbf{x}\right)-H_{ij}\left(\mathbf{x};\mathbf{y}\right)\Delta u_j\left(\mathbf{x}\right)\right]d\Gamma\left(\mathbf{x}\right). \end{aligned} \tag{4.18}$$

The tractions on the crack surfaces are usually equal and opposite (as, for example, on a traction free crack surface) so that $\Sigma t_j = 0$.

Following the general BEM derivation and letting $\mathbf{y}\rightarrow\mathbf{x}$ on the boundary, the boundary integral equation for the crack is given by,

$$\begin{aligned} u_i\left(\mathbf{y}\right)-\Delta u_j\left(\mathbf{y}\right)/2=&\int_S\left[G_{ij}\left(\mathbf{x};\mathbf{y}\right)t_j\left(\mathbf{x}\right)-H_{ij}\left(\mathbf{x};\mathbf{y}\right)u_j\left(\mathbf{x}\right)\right]dS\left(\mathbf{x}\right)-\\ &\int_\Gamma H_{ij}\left(\mathbf{x};\mathbf{y}\right)\Delta u_j\left(\mathbf{x}\right)d\Gamma\left(\mathbf{x}\right) \end{aligned} \tag{4.19}$$

There are two serious deficiencies that arise from the last equation. First, the solution of equation (4.19) is not unique. Any set of equal and opposite tractions on the crack surface, Γ, results in the same equation and, therefore, an identical solution. Second, there are two unknown displacements on Γ, namely Δu_i and u_i. However, these deficiencies can be resolved by utilizing the "multidomain" method which is introduced next.

4.3.4 Multidomain Technique

The multidomain technique was introduced by Lachat and Watson (1976) for the BEM. It has been applied successfully to crack problems (Blandford et al., 1981). This technique is a quite general approach which can be used to analyze large structures, inhomogeneities, etc. Consider the domain having the crack shown Figure 4.5 as an illustrative example. The whole domain is split into regions 1 and 2 so that each region contains one surface of the crack. Therefore, the boundary of each region has two parts, namely the interface and the external surfaces, including a crack surface. By applying boundary integral equation (4.11) to the two regions, the following equations are produced,

$$\left[\mathbf{H}^{(\alpha)} \quad \mathbf{H}_I^{(\alpha)}\right]\begin{Bmatrix}\mathbf{u}^{(\alpha)}\\ \mathbf{u}_I^{(\alpha)}\end{Bmatrix}=\left[\mathbf{G}^{(\alpha)} \quad \mathbf{G}_I^{(\alpha)}\right]\begin{Bmatrix}\mathbf{t}^{(\alpha)}\\ \mathbf{t}_I^{(\alpha)}\end{Bmatrix}+\mathbf{b}^{(\alpha)}, \quad \alpha=1,2. \tag{4.20}$$

Here $\mathbf{u}_I^{(\alpha)}$ and $\mathbf{t}_I^{(\alpha)}$ are the displacement and traction, respectively, on the interface of region α, $\alpha = 1, 2$. The $\hat{\mathbf{b}}^{(\alpha)}$ is the external force contribution due to the body force of region α, $\mathbf{H}_I^{(\alpha)}$ and $\mathbf{G}_I^{(\alpha)}$ are the matrix entries corresponding to the nodes on the interface. The continuity condition on the interface is given by,

$$\mathbf{u}_I^{(1)}=\mathbf{u}_I^{(2)}=\mathbf{u}_I, \quad \mathbf{t}_I^{(1)}=-\mathbf{t}_I^{(2)}=\mathbf{t}_I. \tag{4.21}$$

Applying the interface condition (4.21) to equation (4.20) results in the following equations,

$$\begin{bmatrix}\mathbf{H}^{(1)} & \mathbf{H}_I^{(1)} & -\mathbf{G}_I^{(1)} & \mathbf{0}\\ \mathbf{0} & \mathbf{H}_I^{(2)} & \mathbf{G}_I^{(2)} & \mathbf{H}^{(2)}\end{bmatrix}\begin{Bmatrix}\mathbf{u}^{(1)}\\ \mathbf{u}_I\\ \mathbf{t}_I\\ \mathbf{u}^{(2)}\end{Bmatrix}=\begin{bmatrix}\mathbf{G}^{(1)} & \mathbf{0}\\ \mathbf{0} & \mathbf{G}^{(2)}\end{bmatrix}\begin{Bmatrix}\mathbf{t}^{(1)}\\ \mathbf{t}^{(2)}\end{Bmatrix}+\begin{Bmatrix}\mathbf{b}^{(1)}\\ \mathbf{b}^{(2)}\end{Bmatrix}. \tag{4.22}$$

The last equation is solved after imposing the boundary conditions such as a zero traction on the crack surfaces. Then the displacements can be evaluated at specified internal points through equation (4.10).

4.3.5 Crack-Tip Element

The stress and displacement near a crack tip (or front) has a singularity that behaves like $1/\sqrt{r}$ and $\sqrt{r}$, respectively, where r is the distance from the front. This characteristic behavior can be simulated by using an 8-node, quadrilateral element that includes nodes at the quarter points of the sides running from the crack front (Henshell and Shaw 1975 and Barsoum 1976 and 1977). Such a representation is illustrated in Figure 4.6 where nodes 5 and 7 are located at the quarter points (i.e. they are classified as quarter nodes).

Let u_i and v_i (i = 1, 2, ..., 8) be the in plane node displacements. Then the displacements at a point on the line joining nodes 1 and 2 are,

$$u = u_1 - \left(3u_1 + u_2 - 4u_5\right)\sqrt{\frac{r}{a}} + 2\left(u_1 + u_2 - 2u_5\right)\frac{r}{a} \tag{4.23}$$

and

$$v = v_1 - \left(3v_1 + v_2 - 4v_5\right)\sqrt{\frac{r}{a}} + 2\left(v_1 + v_2 - 2v_5\right)\frac{r}{a} \tag{4.24}$$

where a is the length of the line and r is the point's distance from the crack front. The corresponding strains are,

$$\varepsilon_{xx} = \frac{2\left(u_1 + u_2 - 2u_5\right)}{a} + \frac{\left(-3u_1 - u_2 + 4u_5\right)}{2a\sqrt{r/a}} \tag{4.25}$$

$$\varepsilon_{yy} = -\frac{(3v_1 + v_4 - 4v_8)}{b} + \frac{(5v_1 - v_2 - 3v_3 - v_4 - 4v_5 + 4v_6 + 4v_7 - 4v_8)}{b}\sqrt{\frac{r}{a}} + \frac{2(-v_1 - v_2 + v_3 + v_4 + 2v_5 - 2v_7)}{b}\frac{r}{a} \tag{4.26}$$

and

$$\varepsilon_{xy} = -\frac{3u_1 + u_4 - 4u_8}{b} + \frac{2(v_1 + v_2 - 2v_5)}{a} - \frac{-5u_1 + u_2 + 3u_3 + u_4 + 4u_5 - 4u_6 - 4u_7 + 4u_8}{b}\sqrt{\frac{r}{a}} - \frac{2(u_1 + u_2 - u_3 - u_4 - 2u_5 - 2u_7)}{b}\frac{r}{a} - \frac{3v_1 + v_2 - 4v_5}{2a\sqrt{\frac{r}{a}}} \tag{4.27}$$

where b is the length of the line connecting nodes 1 and 4. The resulting stress components are derived from the general stress-strain relation. They have a singularity of $O\left(1/\sqrt{r}\right)$, as expected. Similar results hold for the displacements at a point on the line joining nodes 3 and 4.

Numerical results arising from the use of the BEM, multidomain method and singular elements are given in the next section for wave scattering in two differently cracked cylinders.

4.4 Numerical Applications

The two numerical examples given next demonstrate the versatility of the modified boundary element method developed previously in this chapter. Example 1 considers wave scattering by an axially symmetric crack in a hollow, isotropic cylinder. Example 2 deals with the problem of a radial-axial crack in a hollow, isotropic cylinder.

The incident wave arises from a ring-load and a point load in the first and second example, respectively.

Example 1

This example was studied by Zhuang (1998). It is used here to check the proposed numerical procedure. An infinitely long, homogeneous, isotropic, hollow cylinder is considered in here whose Poisson ratio, ν, is 1/3. The ratio of the thickness to the mean radius of the cylinder, *H*/*R*, is,

$$H/R = 0.1. \tag{4.28}$$

The non-dimensional frequency, Ω, is defined as,

$$\Omega = \frac{\omega}{\omega_{ref}} \text{ where } \omega_{ref} = \frac{1}{H}\sqrt{\frac{\mu}{\rho}} \tag{4.29}$$

and μ is the shear modulus whilst ρ is the mass density. An axisymmetrical, circumferential surface-breaking, vertical crack is located in the planar section, $z = 0$, of the cylinder. The crack's depth is half the thickness of the cylinder, as shown in Figure 4.7. The ring-load is applied in the *r*-direction on the cylinder's outer surface at $z = 5H$.

The multidomain technique is adopted to circumvent difficulties caused by the presence of the crack. Consequently, the cylinder is partitioned into two subdomains with a vertical, fictitious boundary that extends from the crack front to the cylinder's outer surface, as shown in Figure 4.7. It should be noted that only half the axisymmetric cylinder is given in this figure. Quadrilateral element with quarter-nodes, which are shown as the unblocked circles in Figure 4.7b, are used adjacent to the crack front. The

boundary element mesh includes 32, quadratic 8-node elements having 112 nodes in each subdomain. It is distributed uniformly in the circumferential direction. As before, only four layers are used in the radial direction.

A transparency check is performed initially by evaluating the displacements and tractions at cross-section $z = 0$ that are caused by a point load at $z = 5H$. These variables correspond, in actuality, to the displacement and traction Green's functions obtained in Chapter 2. The differences between the values found from the BEM and those from the Green's functions are less than an insignificant 0.1%.

The non-dimensional radial displacement amplitude, $|U_r|$, at the cylinder's outer surface points (R_{outer}, $0.05H$) and (R_{outer}, $-5H$), which are located in the near and far wave fields respectively, is presented in Figure 4.9. (Details of the non-dimensionalizations, which relate not only to the displacements but also to the stresses and tractions, are given more conveniently in Appendix C.) The legends "BEM (Zhuang 1998)" and "FEM (Zhuang 1998)", which are used in Figure 4.9, designate the results from a boundary element method and finite element method that assume axisymmetry a priori. The legend "BEM (present study)", on the other hand, indicates the present data obtained from the boundary element method with a fully three-dimensional capability. In the latter case, of course, a problem need not necessarily be axisymmetric.

Figure 4.9 shows that, regardless of the numerical approach, results are always in good agreement apart from a very small discrepancy in the near field's radial displacement amplitude for Ω just less than the cutoff frequency $\Omega = 3.05$. This discrepancy probably arises from the near field response's greater sensitivity to a small frequency change near a cutoff frequency.

Although the present approach is more generally applicable, it needs a two-dimensional boundary surface as opposed to a one-dimensional curve to be discretized. On the other hand, only four layers are used in the radial direction rather than the thirty layers employed in the axisymmetric approach of Zhuang (1998). Fewer layers, of course, lead to fewer linear equations whose numerical solution, therefore, requires much less effort. Overall, the present approach demands about a thirty and six times increase in the computer time and storage needs, respectively, to solve an axisymmetric problem.

Example 2

The cylinder and its material properties considered next are identical to those used in example 1 of Chapters 2 and 3. Young's modulus is 216.9 GPa, the Poisson ratio, υ, is 0.287 and the longitudinal and torsional wave speeds are given, respectively, by,

$$c_1 = 5.96\times10^3\, m/s,\ c_2 = 3.26\times10^3\, m/s\,.$$

The inner radius, R_{inner}, and thickness, H, of the cylinder are,

$$R_{inner} = 38mm,\ H = 5.5mm$$

so that the ratio of the cylinder's thickness to mean radius, H/R, is 0.135. The non-dimensional frequency is given again by equation (4.29). Now l is defined as the axial crack length and d is the crack's depth which is measured from the cylinder's outer surface. The non-dimensional crack length, L, is given by,

$$L = \frac{l}{H} \tag{4.30}$$

and the non-dimensional crack depth, D, is,

$$D = \frac{d}{H}. \tag{4.31}$$

The axially planar crack is located at $\theta = 0^\circ$ and it is symmetrical with respect to the $z = 0$ plane. The crack's geometry is indicated by the shaded region in Figure 4.8.

The crack's depth in the radial direction, d, is always half the thickness of the cylinder, H, i.e. $D = 0.5$ throughout. Three different crack lengths are considered in the axial direction. They correspond to l equal $0.5H$, H and $1.5H$. The partitioning of the domain and a typical boundary element mesh are illustrated in Figure 4.8. The unblocked circles shown in this figure represent the quarter nodes. Subdomains 1 and 2 are both bounded by the planes $z = 0.5l$ and $z = -0.5l$ as well as by the cylinder's inner and outer surfaces, $r = R_{inner}$ and $r = R_{outer}$. However, subdomain 1 lies within $0^\circ \leq \theta \leq 10^\circ$ and subdomain 2 is in the remaining region. As the curved boundaries $r = R_{inner}$ and $r = R_{outer}$ are traction free, they need not be discretized. Thus, the boundary element mesh is distributed on only four planar surfaces. It has 64, 8-node quadrilateral elements with 224 boundary nodes on each subdomain. More elements are used in the crack surface $\theta = 0^\circ$, compared with the $\theta = 10^\circ$ plane, because the former plane contains the discontinuous crack front.

An incident wave is introduced in the cylinder by applying a point load at (R_{outer}, 35°, 0). Four observation points are located at (R_{outer}, 35°, 0), (R_{outer}, 8°, 0), (R_{outer}, −8°, 0) and (R_{outer}, −35°, 0). The (R_{outer}, 35°, 0) and (R_{outer}, 8°, 0) are between the source point and the crack surface whereas (R_{outer}, −8°, 0) and (R_{outer}, −35°, 0) are on the other side of the crack to the source. Therefore, the first two points are in the region of "reflected" waves and the last two points are affected by the "transmitted" waves. The

non-dimensional displacement amplitudes in the radial and circumferential directions, $|U_r|$ and $|U_\theta|$, respectively, are presented in Figures 4.10 through 4.13 at the four observation points for the three chosen crack lengths. Analogous results for an identical, crack-free cylinder are also shown in each figure. The frequency range, $0.6 \leq \Omega \leq 0.9$, is essentially identical to that used in examples 1 and 2 of Chapter 3.

Figure 4.10a indicates that $|U_r|$ hardly changes at (R_{outer}, 35°, 0) in $0.6 \leq \Omega \leq 0.9$ with the introduction of an axial crack, except around $\Omega = 0.62$. Even at $\Omega = 0.62$, a noticeable difference in $|U_r|$ requires L to be greater than 0.5. A given percentage growth in L beyond 0.5 leads to a somewhat higher percentage increase in $|U_r|$ so that the relationship between $|U_r|$ and L is not quite linear. Figure 4.10b, on the other hand, suggests that the corresponding $|U_\theta|$ has greater sensitivity at more discrete frequencies than $|U_r|$, especially for $L = 0.5$. However, the greatest change in $|U_\theta|$, with increasing L, generally occurs at the few lowest Ω of about 0.62, 0.65, 0.68 and 0.72. Although $|U_\theta|$ alters most at $\Omega = 0.68$, when L grows from zero (the uncracked case) to 0.5, further enlargements L are distinguished more clearly at $\Omega = 0.65$ because $|U_\theta|$ increases monotonically with L there.

Figures 4.10 and 4.11 indicate that the behavior of $|U_r|$ and $|U_\theta|$ is generally similar for different Ω and L at the two observation points located in the reflected wave region, (R_{outer}, 35°, 0) and (R_{outer}, 8°, 0). The introduction of a crack usually has the greatest effect in Figure 4.11 below $\Omega = 0.72$. However, $|U_r|$ again has the greatest growth of all at $\Omega = 0.62$ when L increases from 0.5 to 1.5. On the other hand, $|U_r|$ experiences little change at $\Omega = 0.62$ with the introduction of the smallest crack length, $L = 0.5$, in the crack-free cylinder. Such an introduction is discerned most easily by

monitoring $|U_\theta|$ at $\Omega = 0.68$ again. However, unlike before, an increase in L from 0.5 to 1.0 cannot be distinguished in Figure 4.11 by using $|U_\theta|$ at $\Omega = 0.68$ or even $\Omega = 0.65$ even though $|U_\theta|$ changes most noticeably at $\Omega = 0.65$ when L increases further to 1.5. Therefore, more than one observation position is clearly needed in the reflected wave region to continuously monitor the introduction and growth of a crack. A comparison of Figures 4.11 and 4.12, as well as Figures 4.10 and 4.13, suggests that the overall behavior of $|U_r|$ and $|U_\theta|$ for different Ω and L is little different in the transmitted wave region from that in the reflected region. Consequently, the detection of a small crack length needs $|U_\theta|$ to be determined but non-dimensional crack lengths, L, greater than 0.5 are more readily apparent by observing $|U_r|$ at $\Omega = 0.62$.

4.5 Concluding Remarks

A boundary element method for generally solving three-dimensional wave scattering by a crack oriented arbitrarily in a cylinder is developed in this chapter. However, computational data are presented for only two specific orientations. They correspond to an axial crack and a circumferential crack. A multidomain technique and 8-node quadrilateral elements handle the singularity introduced by a crack. Computed results show good agreement with available data. The determination of both $|U_r|$ and $|U_\theta|$ at more than one value of Ω and observation point is shown to be necessary to detect the initiation and growth of an axial crack.

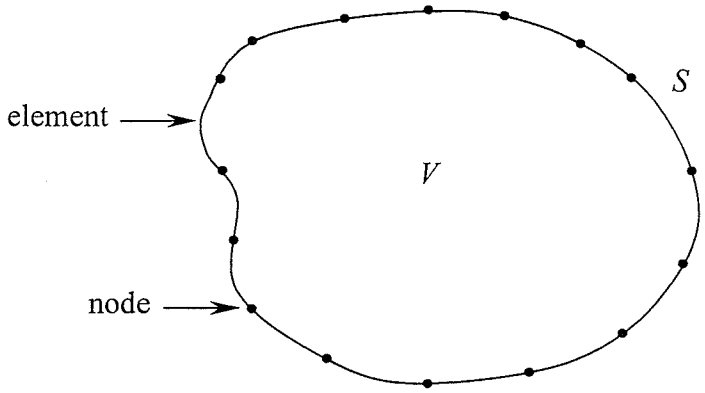

Figure 4.1. Discretization of a boundary surface in the BEM.

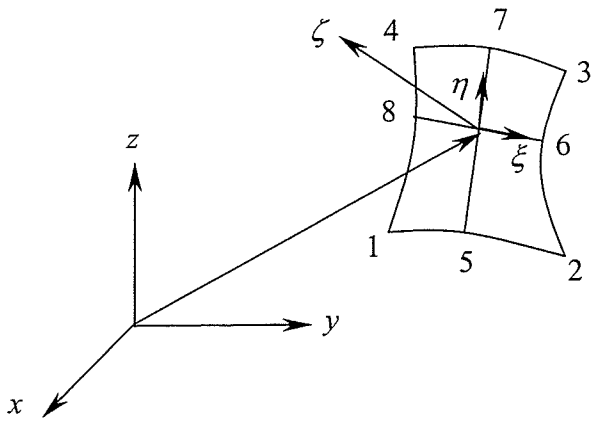

Figure 4.2. Eight-node quadrilateral element and the global-local coordinate systems (x, y, z) and (ξ, η, ζ)

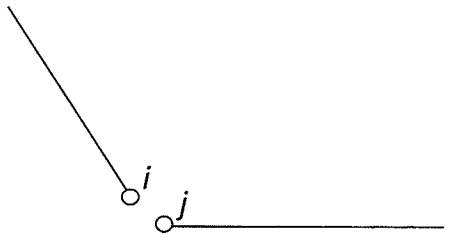

Figure 4.3. Illustrating a corner point configuration and the double node technique

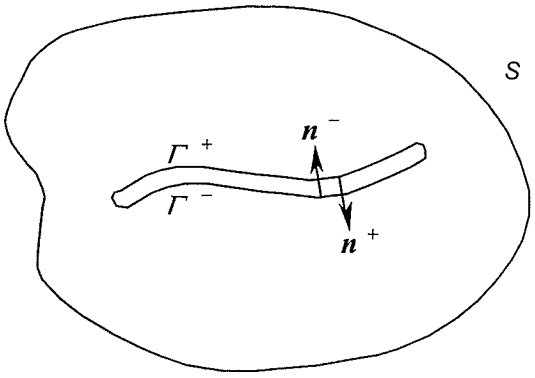

Figure 4.4. Geometry of crack surfaces

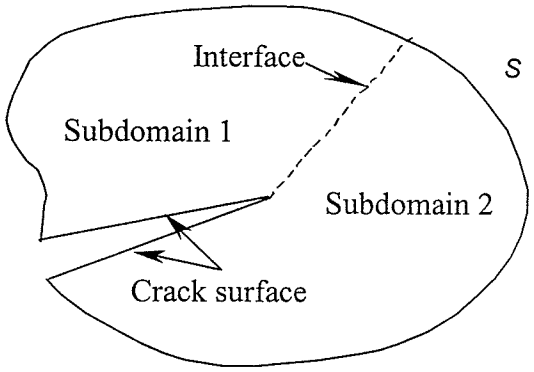

Figure 4.5. Partitioning a cracked domain

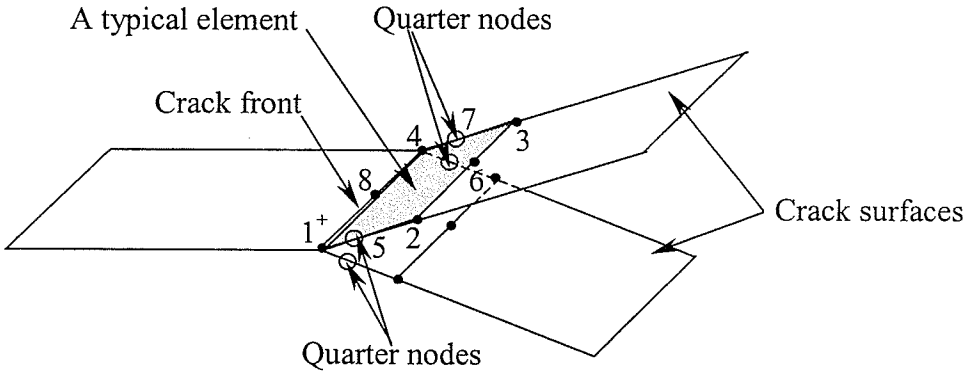

Figure 4.6. Configuration of a quarter point, crack-tip element. + indicates numbering of element's nodes

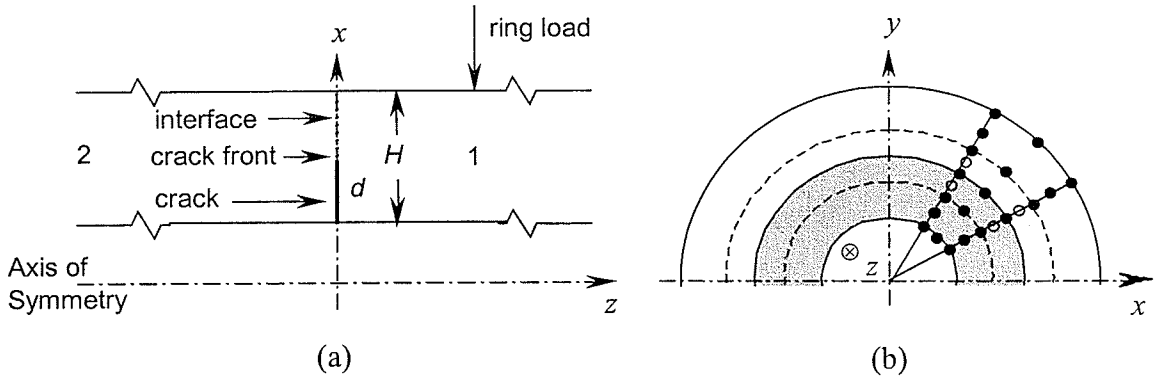

Figure 4.7. Showing (a) a circumferential crack's configuration and partitioning of the domain, and (b) a typical mesh on the cracked cross-section

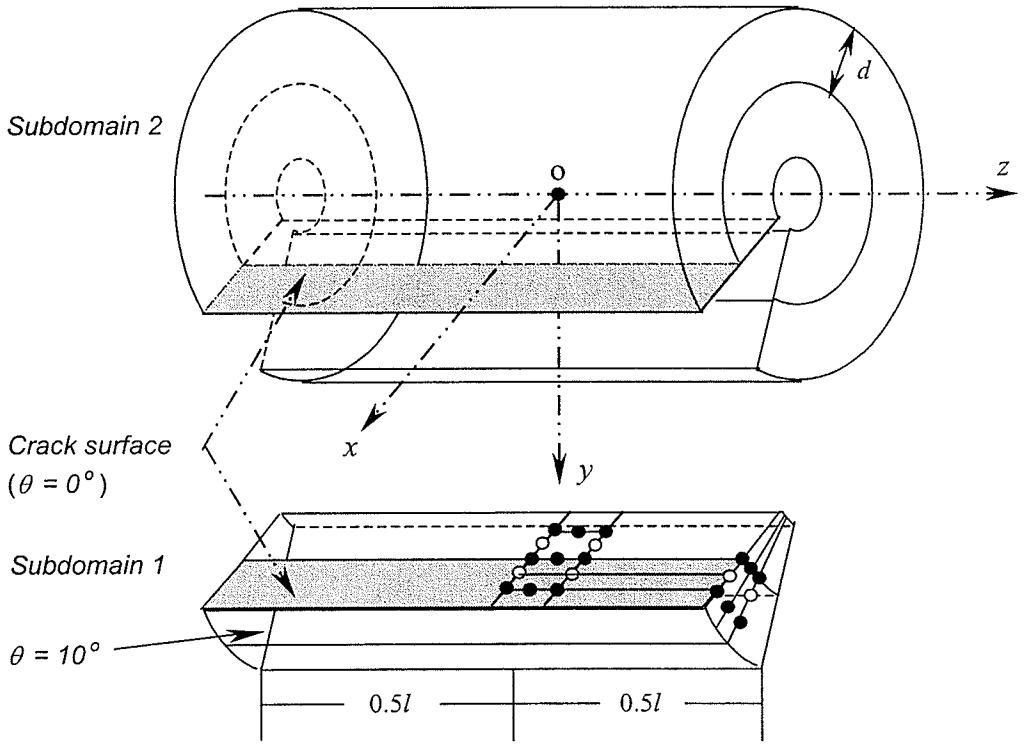

Figure 4.8. Illustrating the axial crack's configuration and the partitioning of the domain

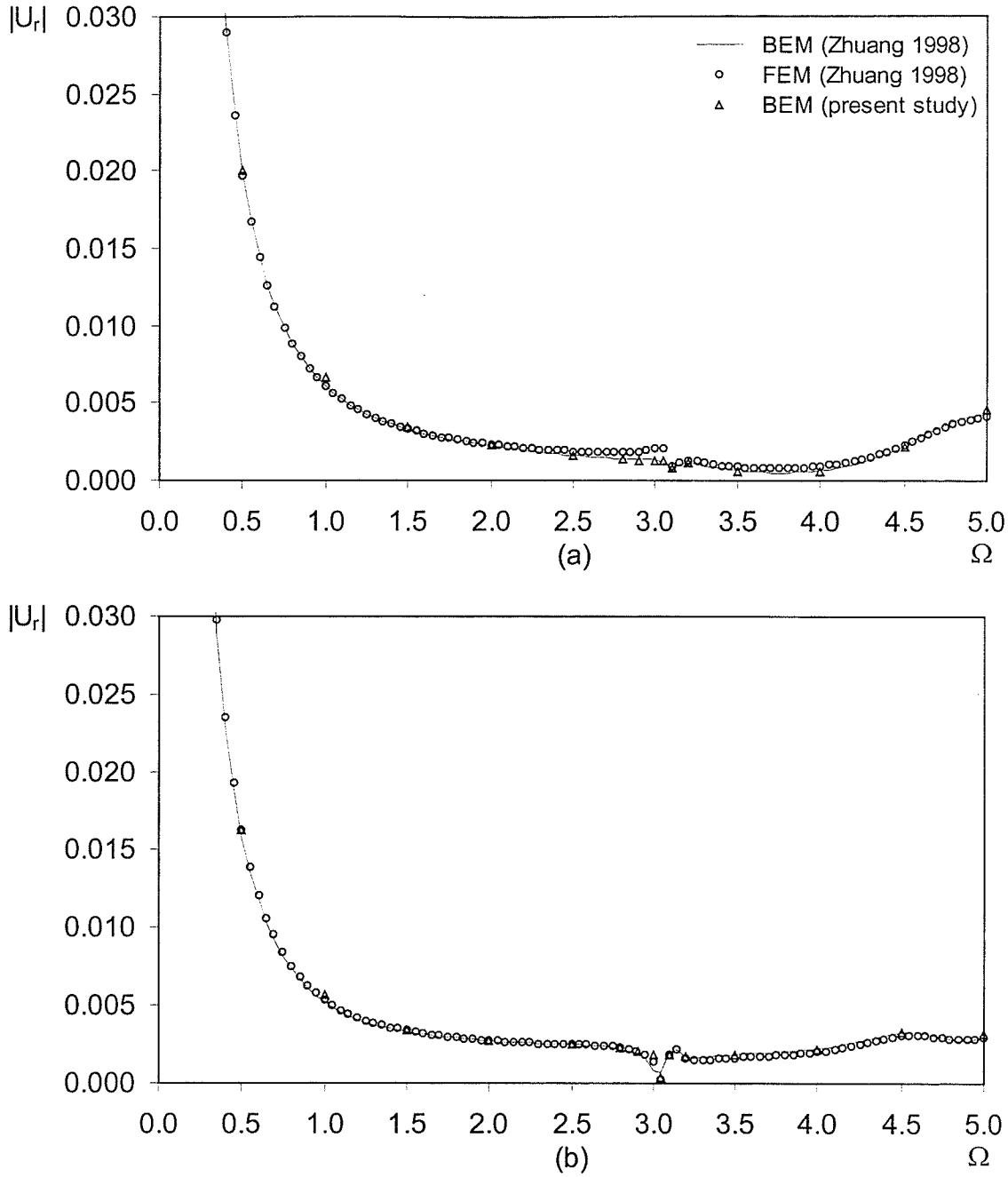

Figure. 4.9. Radial displacement amplitude at (a) (R_{outer}, 0.05H) and (b) (R_{outer}, -5H) due to a ring load at (R_{outer}, 5H)

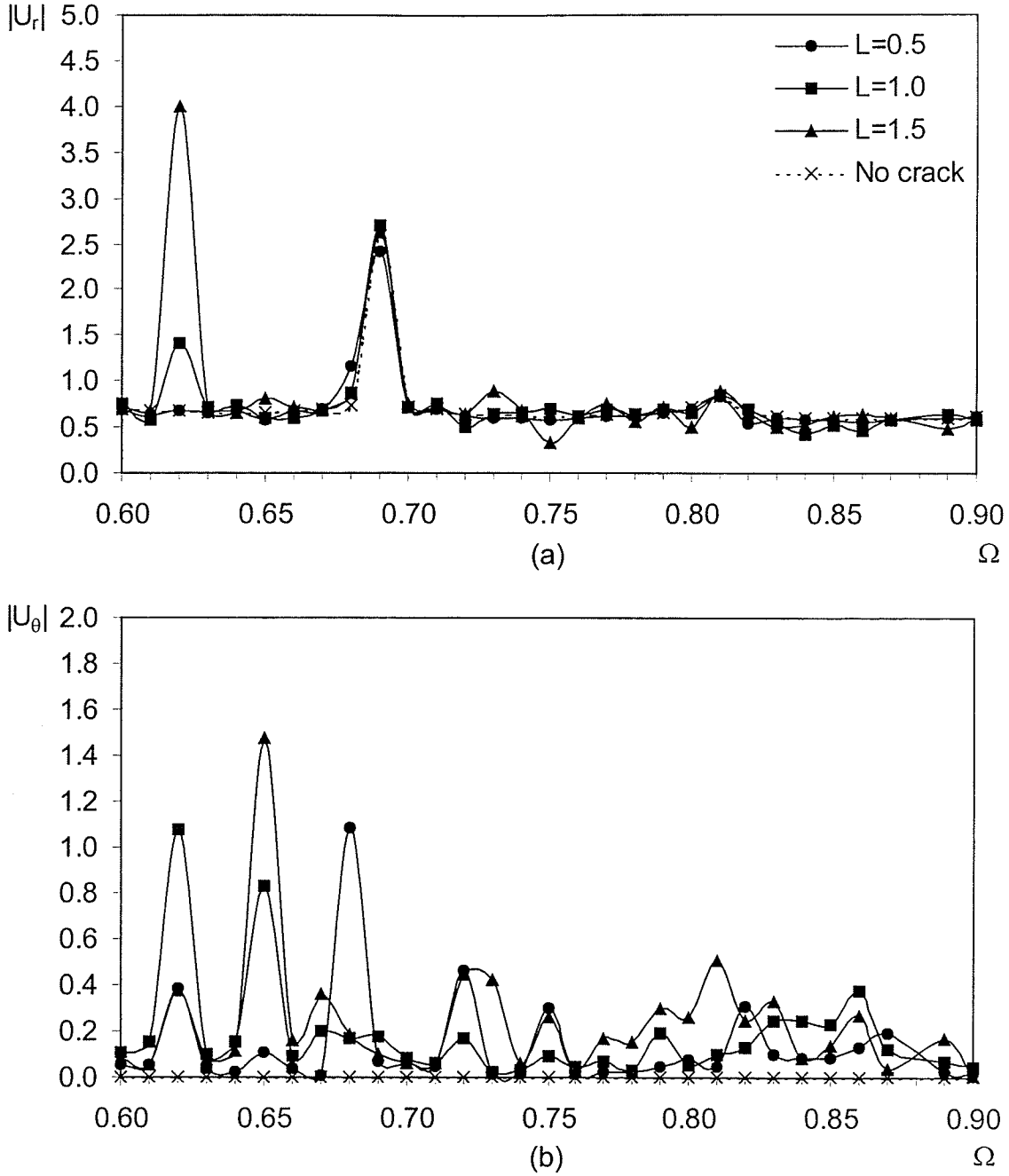

Figure 4.10. Displacement amplitude at (R_{outer}, 35°, 0) for three crack lengths and a point load in the r direction located at (R_{outer}, 35°, 0). (a) Radial displacement, $|U_r|$, and (b) the circumferential displacement, $|U_\theta|$

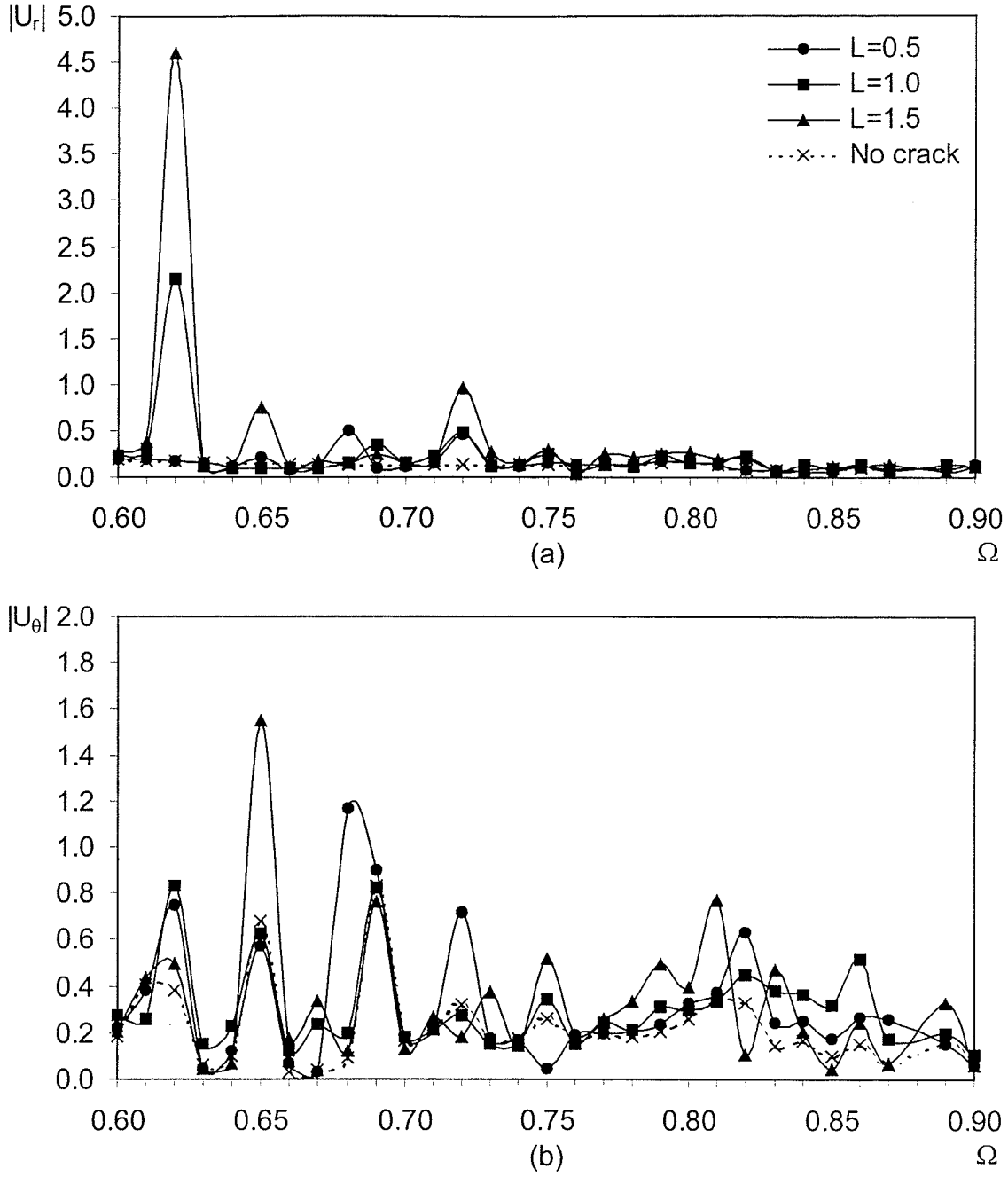

Figure 4.11. Displacement amplitude at (R_{outer}, 8°, 0) for three crack lengths and a point load in the r direction located at (R_{outer}, 35°, 0). (a) Radial displacement, $|U_r|$, and (b) the circumferential displacement, $|U_\theta|$

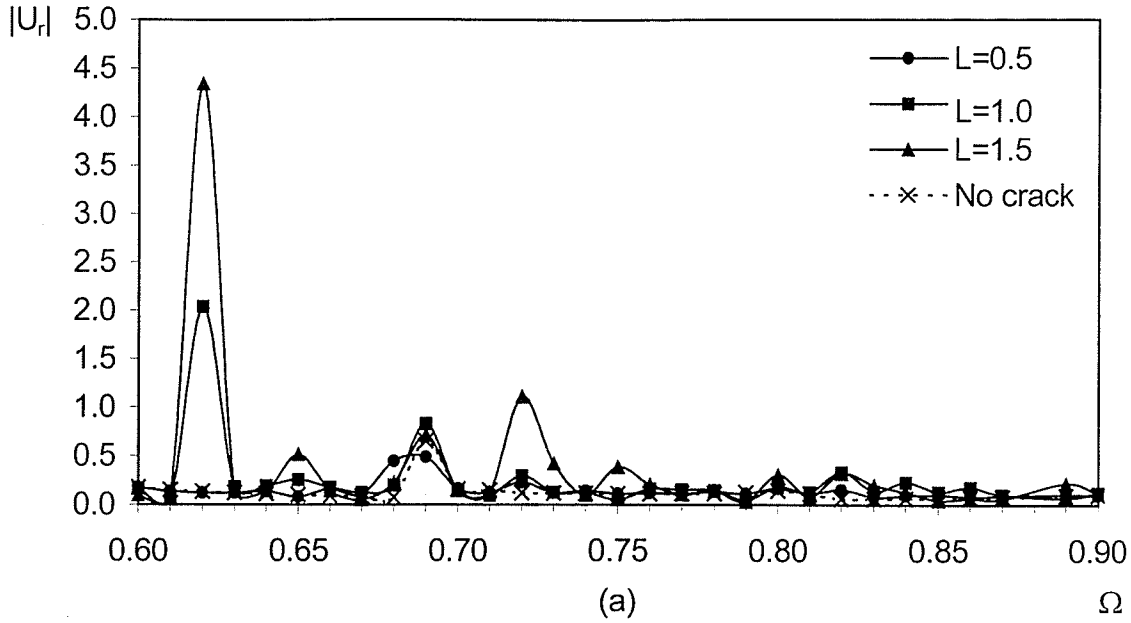

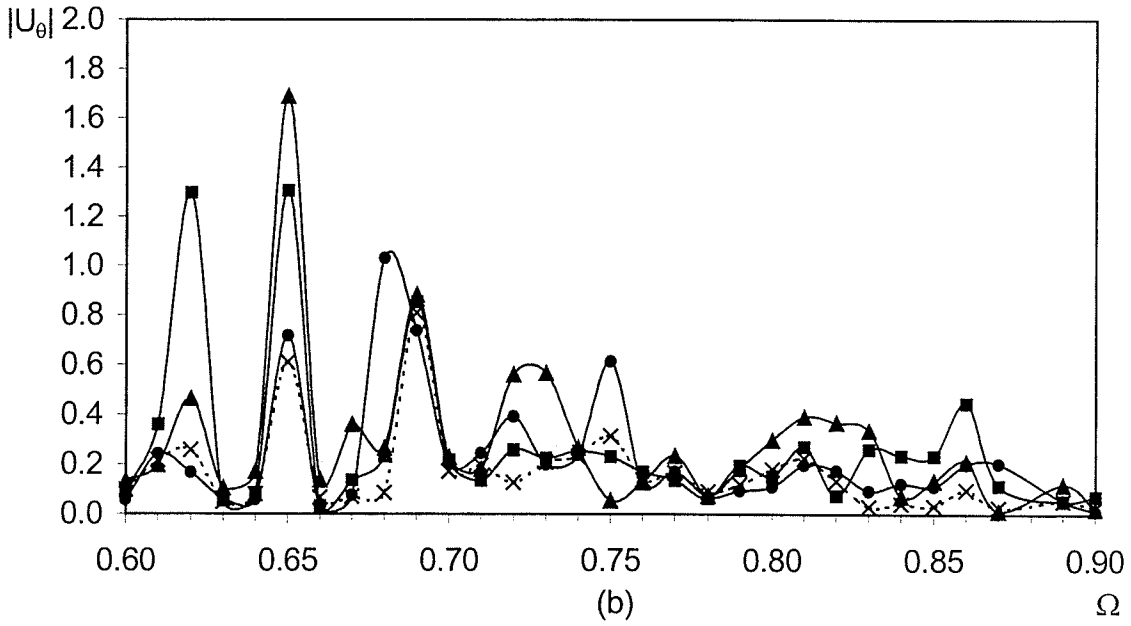

Figure 4.12. Displacement amplitude at (R_{outer}, -8°, 0) for three crack lengths and a point load in the r direction located at (R_{outer}, 35°, 0). (a) Radial displacement, $|U_r|$, and (b) the circumferential displacement, $|U_\theta|$

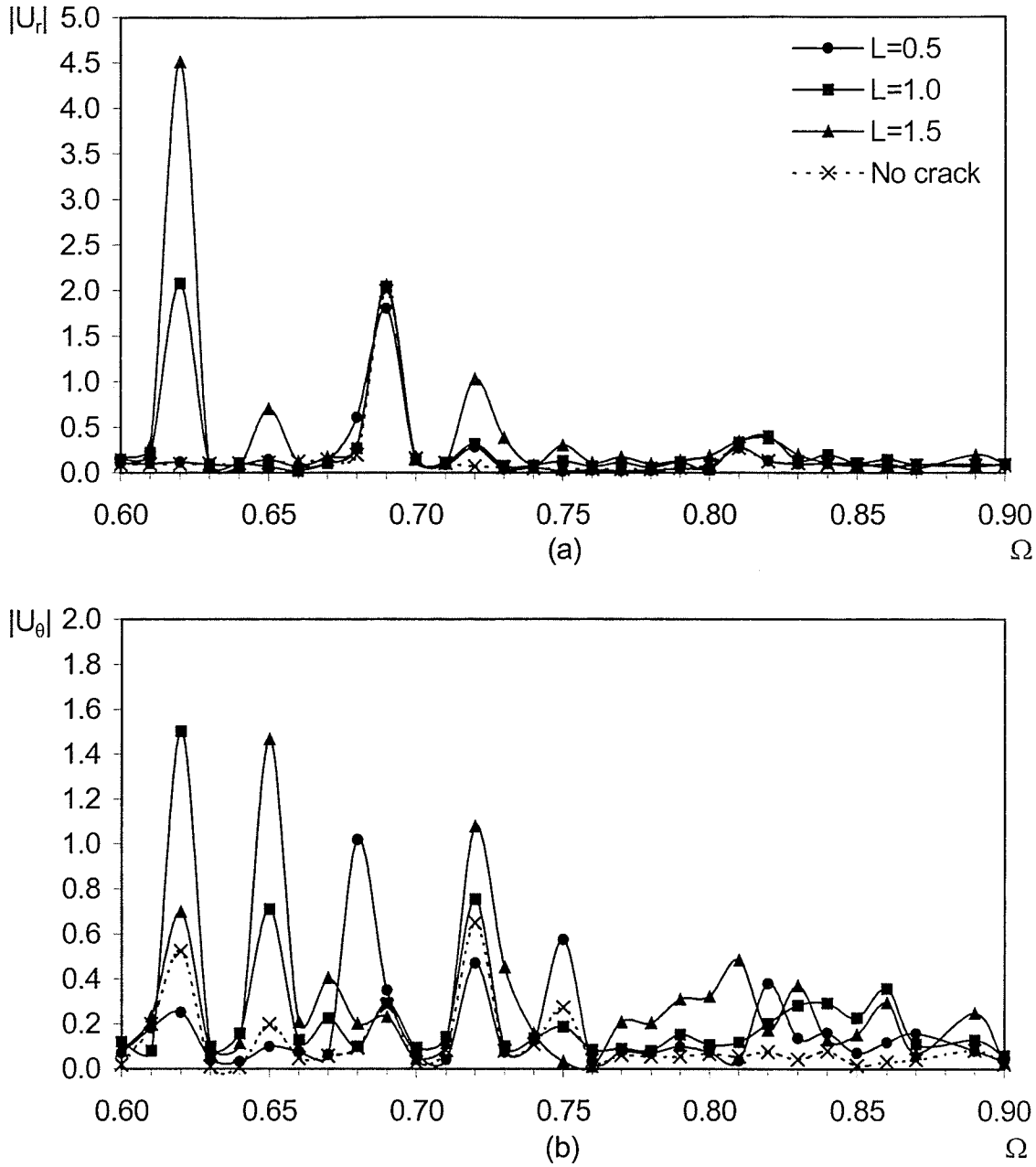

Figure 4.13. Displacement amplitude at (R_{outer}, -35°, 0) for three crack lengths and a point load in the r direction located at (R_{outer}, 35°, 0). (a) Radial displacement, $|U_r|$, and (b) the circumferential displacement, $|U_\theta|$

Chapter 5

Conclusions and Recommendations

5.1 Conclusions

An analytical formulation of the dispersion relation in a homogeneous, isotropic cylinder is studied first. By treating the radial dependence of the displacement as a one-dimensional finite element model through the thickness of the cylinder, the approximate dispersion relation of a laminated composite cylinder is formulated as a standard eigenvalue problem. The eigenvalues serve as an initial approximation for an isotropic cylinder when Muller's method is employed to obtain the exact (refined) solution. Three dimensional elastodynamic Green's functions are established in an isotropic or laminated composite cylinder in terms of the guided wave modes due to a point load.

A novel solution procedure is presented for the scattering of guided waves in a pipe having a planar circumferential crack of arbitrary circumferential length and radial depth. In this procedure, the original three dimensional problem is decomposed first into

a symmetric sub-problem and an anti-symmetric sub-problem. Hence, only half the cylinder needs to be considered. Because the wave functions automatically satisfy the boundary conditions at the inner and outer curved surfaces as well as the radiation conditions at infinity, only the plane of the crack needs to be discretized. After employing a transfer matrix from radius to radius, these two sub-problems can be simplified further to quasi-one-dimensional problems. This procedure is computationally efficient; it requires only about 5% of the time needed for a fully three dimensional finite element analysis. The resulting numerical data agree well with limited available experimental data. However, it is shown that the modal representation of the scattered and incident wave fields is sensitive to the length and depth of a planar crack.

The new method is extended easily to a more complex, composite lay-up in cylindrical tubes because the semi-analytic finite element method is quite generally applicable. It can also be used for arbitrary anisotropy. However, the circumferential crack must be vertical.

A boundary element method for generally solving three-dimensional wave scattering by a crack oriented arbitrarily in a cylinder is developed in Chapter 4. The incident wave is taken as a point load. However, computational data are presented for only two specific orientations, an axial crack and a circumferential crack. A multidomain technique and 8-node quadrilateral elements handle the singularity introduced by a crack. Computed results show good agreement with limited available data. The determination of both the non-dimensional radial and circumferential displacement amplitude, $|U_r|$ and $|U_\theta|$, at more than one value of the non-dimensional frequency, Ω, and observation point is shown to be necessary to detect the initiation and growth of an axial crack. Although

the numerical results are presented only for an isotropic cylinder in this thesis, the method can be extended straightforwardly for a composite cylinder. However, the method demands about a twenty fold increase in the computational time compared with the approach described in Chapter 3.

5.2 Recommendations

As a research program whose aim is to develop an efficient and accurate numerical method for the three-dimensional wave scattering in a cylinder, the following recommendations are suggested for future work.

1. The numerical data presented in this thesis has been limited to values of Ω below five. Further studies are needed when Ω is above five.
2. The numerical techniques presented in Chapter 3 are valid only for a vertical circumferential crack. They might be extended to a crack having a small inclination to the vertical by using a (small) perturbation method.
3. The BEM described in Chapter 4 can be made computationally faster by taking advantage of the known analytical variations of the Green's functions in a cylinder's circumferential and axial directions. The computations are presently performed inefficiently on a point by point basis.
4. The wave scattering results given in Chapter 4 should be validated experimentally.

References

Alleyne, D. N., Lowe, M. J. S., and Cawley, P., 1998, "The Reflection of Guided Waves from Circumferential Notches in Pipes," ASME *Journal of Applied Mechanics*, **65**, pp. 635-641.

Armenàkas, A. E., 1965, "Torsional Waves in Composite Rods," *Journal of the Acoustical Society of America*, **38**, pp. 439–446.

Armenàkas, A. E., Gazis, D. C., and Herrmann, G, 1969, *Free Vibrations of Circular Cylindrical Shells*, Pergamon Press, Oxford.

Armenàkas, A. E. and Reitz, E. S., 1973, "Propagation of Harmonic Waves in Orthotropic Circular Cylindrical Shells," ASME *Journal of Applied Mechanics*, **27**, pp. 663-668.

Barbero E. J., Reddy, J. N., and Teply, J. L., 1990, "General Two-Dimensional Theory of Laminated Cylinder Shells," *AIAA Journal*, **28**(3), pp. 544-553.

Barsoum, R. S., 1976, "On the Use of Isoparametric Finite Elements in Linear Fracture Mechanics," *International Journal for Numerical Methods in Engineering*, **10**, pp. 25-37.

Barsoum, R. S., 1977, "Triangular Quarter-Point Elements as Elastic and Perfectly-Plastic Crack-Tip Elements," *International Journal for Numerical Methods in Engineering*, **11**, pp. 85-98.

Bathe, K. J., 1982. *Finite Element Procedures in Engineering Analysis*. Prentice-Hall Inc, Englewood Cliffs, New York.

Blandford, G. E., Ingraffea, A. R., and Liggett, J. A., 1981, "Two-Dimensional Stress Intensity Factor Computations Using the Boundary Element method," *International Journal for Numerical Methods in Engineering*, **17**, pp. 387 – 404.

Brebbia, C. A., Telles, J. C. F., and Wrobel, L. C., 1984, *Boundary Element Techniques – Theory and Applications in Engineering*, Springer Verlag, Berlin, Heldeberg, New York, Tokyo.

Chree, C., 1889, "The Equations of an Isotropic Elastic Solid in Polar and Cylindrical Coordinates, their Solutions and Applications," *Trans. Cambridge Philosophical Society*, **14**, pp. 250-269.

Chou, F. H. and Achenbach, J. D., 1972, "Three-Dimensional Vibrations of Orthotropic Cylinders," *Journal of Engineering Mechanics*, **98**, pp. 813-822.

Cruse, T. A., 1974, "An Improved Boundary Integrals Equation Method for Three-Dimensional Elastic Stress Analysis," *Computers and Structures*, **4**, pp. 741 – 754.

Cruse, T. A., 1988, *Boundary Element Analysis in Computational Fracture Mechanics*, Kluwer Academic Publishers, Dordrecht, Boston, London.

Datta, S. K., Achenbach, J. D., and Rajapakse, Y. S., (Eds.), 1990, Elastic Waves and Ultrasonic Nondestructive Evaluation, Elsevier Science Publishers, Amsterdam, North Holland.

Davies, R. M., 1948, "A Critical Study of the Hopkinson Pressure Bar," Phil. Trans. R. Soc., **A240**, pp. 375-457.

Folk, R. T., Fox, G., Shook, C. A., and Curtis, C. W., 1958, "Elastic Strain Produced by Sudden Application of Pressure to One End of a Cylindrical Bar--I. Theory," *Journal of the Acoustical Society of America*, **30**, pp. 559–563.

Fox, G. and Curtis, C. W., 1958, "Elastic Strain Produced by Sudden Application of Pressure to One End of a Cylindrical Bar--II. Experimental Observations," *Journal of the Acoustical Society of America*, **30**, pp. 786–794.

Gazis, D. C., 1959, "Three-Dimensional Investigation of the Propagation of Waves in Hollow Circular Cylinders. I. Analytical Foundation, II. Numerical Results," *Journal of the Acoustical Society of America*, **31**(5), pp. 568-578.

Green, W. A., 1964, "Dispersion Relations for Elastic Waves in Bars," in *Progress in Solid Mechanics*, (Eds., Sneddon, I. N. and Hill, R.), Vol. 1, Chap. 5, North-Holland Publishing Company, Armsterdam.

Gregory, R. D. and Gladwell, I., 1989, "Axisymmetric Waves in a Semi-Infinite Elastic Rod," ASME *Journal of Applied Mechanics*, **42**, pp. 327–337.

Huang, K. H. and Dong, S. B., 1984, "Propagating Waves and Edge Vibrations in Anisotropic Composite Cylinder," *Journal of Sound and Vibration*, **96(3)**, pp. 635-641.

Jones, O. E. and Norwood, F. R., 1967, "Axially Symmetric Cross-Sectional Strain and Stress Distributions in Suddenly Loaded Cylindrical Elastic Bars," ASME *Journal of Applied Mechanics*, **34**, pp. 718–724.

Keck, H. E. and Armenàkas, A. E., 1971, "Wave Propagation in Transversely Isotropic Layered Cylinders," *Journal of Engineering Mechanics*, **97**, pp. 541–558.

Khdeir, A. A., Reddy, J. N., and Frederick, D., 1989, "A Study of Bending, Vibration and Buckling of Cross-Ply Circular Cylindrical Shells with Various Shell Theories," *International Journal of Engineering Science*, **27**(11), pp. 1337-1351.

Kohl, T., Datta, S. K. and Shah, A. H., 1992, "Axially Symmetric Pulse Propagation in Semi-Infinite Hollow Cylinders," *AIAA Journal*, **30**(6), pp. 1617-1624.

Lachat, J. C. and Watson, J. O., 1976, "Effective Numerical Treatment of Boundary Integral Equations," *International Journal for Numerical Methods in Engineering*, **10**, pp. 991 – 1005.

Lowe, M. J. S., Alleyne, D. N., and Cawley, P., 1998, "The Mode Conversion of a Guided Wave by a Part- Circumferential Notch in a Pipe," ASME *Journal of Applied Mechanics*, **65**, pp. 649-656.

McNiven, H. D., Sackman, J. L., and Shah, A. H., 1963, "Dispersion of Axially Symmetric Waves in Composite, Elastic Rods," *Journal of the Acoustical Society of America*, **35**, pp. 1602-1609.

McNiven, H. D., 1961, "Extensional Waves in a Semi-Infinite, Elastic Rods," *Journal of the Acoustical Society of America*, **33**, pp. 23-27.

McNiven, H. D., Shah, A. H., and Sackman, J. L., 1966a, "Axially Symmetric Waves in Hollow, Elastic Rods: Part I," *Journal of the Acoustical Society of America*, **40**(4), pp. 784-792.

McNiven, H. D., Shah, A. H., and Sackman, J. L., 1966b, "Axially Symmetric Waves in Hollow, Elastic Rods. Part II," *Journal of the Acoustical Society of America*, **40**(5), pp. 1073-1076.

McNiven, H. D., Shah, A. H., 1967, "The Influence of End Mode on the Resonant Frequencies of Finite, Hollow, Elastic Rods," *J. Sound Vib.* **6**, pp. 8-19.

Meitzler, A. H, 1961, "Mode Coupling Occurring in the Propagation of Elastic Pulses in Wires," *J. Acoust. Soc. Am.*. **33**, pp. 435-445.

Meitzler, A. H, 1965, "Backward-Wave Transmission of Stress Pulses in Elastic Cylinders and Plates," *J. Acoust. Soc. Am.*. **38**, pp. 835-842.

Miklowitz, J., 1955, "Travelling Compressional Waves in an Ealstic Rod According to the More Exact One-Dimensional Theory," *Proc. 2nd U.S. National Congress of Applied Mechanics*, pp. 179-186, ASME, New York.

Miklowitz, J., 1957, "The Propagation of Compressional Waves in a Dispersive Elastic Rod, Part I-Results from the Theory" ASME *Journal Applied Mechanics*, **24**, pp. 231-239.

Miklowitz, J., 1958, "On the Use of Approximate Theories of an Elastic Rod in Problems of Longitudinal Impact," *Proc. 3rd U.S. National Congress of Applied Mechanics*, pp. 179-186, ASME, New York.

Miklowitz, J., 1960, "Recent Developments in Elastic Wave Propagation," ASME *Applied Mechanics Review*, **13**(12), pp. 865-878.

Mindlin, R. D. and Herrman, G., 1950, "A One-Dimensional Theory of Compressional Waves in an Elastic Rod," *Proc. 1st U.S. National Congress of Applied Mechanics*, pp. 187-191.

Mindlin, R. D. and McNiven, H. D., 1960, "Axially Symmetric Waves in Elastic Rods," ASME *Journal of Applied Mechanics*, **27**, pp. 145-151.

Mirsky, I., 1964, "Axisymmetric Vibrations of Orthotropic Cylinders," *Journal of the Acoustical Society of America*, **36**, pp. 2106-2122.

Mirsky, I., 1966, "Three-Dimensional and Shell-Theory Analysis for Axisymmetric Vibrations of Orthotropic Shells," *Journal of the Acoustical Society of America*, **39**, pp. 549-554.

Mitrinovic, D. S. and Keckic, J. D., 1984, *The Cauchy Method of Residues*, D. Reidel Publishing Co., Boston.

Muller, D. E., 1956, "A Method for Solving Algebraic Equations Using an Automatic Computer," *Mathematical Tables and Aids to Computation*, **10**, pp. 208 – 215.

Nelson, R. B., Dong, S. B., and Kalra, R. D., 1971, "Vibration and Waves in Laminated Orthotropic Circular Cylinders," *Journal of Sound and Vibration*, **18**, pp. 429 – 444.

Nowinski, J. L., 1967, "Propagation of Longitudinal Waves in Circular Cylindrically Orthotropic Bars," *ASCE Journal of Engineering for Industry*, **89**, pp. 408 – 412.

Oliver, J., 1957, "Elastic Wave Dispersion in a Cylindrical Rod by a Wide-Band Short_Duration Pulse Technique," *Journal of the Acoustical Society of America*, **29**, pp. 189-194.

Onoe, M., McNiven, H. D., and Mindlin, R. D., 1962, "Dispersion of Axially Symmetric Waves in Elastic Rods," *ASME Journal of Applied Mechanics*, **29**, pp. 729-734.

Pan, E, Rogers, J., Datta, S. K., and Shah, A. H., 1999, "Mode Selection of Guided Waves for Ultrasonic Inspection of Gas Pipelines with Thick Coating," *International Journal of Mechanics of Materials*, **31**, pp. 163-174.

Pochhammer, L., 1876, "Ueber die Fortpflanzungsgeschwindigkeiten Schwingungen in einem Unbegrenzten Isotropen Kreiscylinder," *Zeitschrift für Mathematik*, **81**, pp. 324-336.

Rattanawangcharoen, N., and Shah, A. H., 1992a, "Guided Waves in Laminated Isotropic Circular Cylinders," *Computational Mechanics*, **10**, pp. 97-105.

Rattanawangcharoen, N., and Shah, A. H., 1992b, "Wave Propagation in Laminated Composite Circular Cylinders," *International Journal of Solids and Structures*, **29**(6), pp. 767-781.

Rattanawangcharoen, N., Zhuang, W., Shah, A. H. and Datta, S. K., 1997, "Axisymmetric Guided Wave in Jointed Laminated Cylinders," ASCE *Journal of Engineering Mechanics*, **123**, No. 10, pp. 1020-1026.

Skalak, R., 1957, "Longitudinal Impact of a Semi-Infinite Circular Elastic Bar," *ASME Journal of Applied Mechanics*, **34**, pp. 59-64.

Sneddon, I. N., 1951, *Fourier Transforms*, McGraw-Hill Book Co., New York.

Soldatos, K. P., 1994, "Review of Three Dimensional Dynamic Analysis of Circular Cylinders and Cylindrical Shells," *ASME Applied Mechanics Review*, **47**(10), pp. 501-516.

Xu, P. C. and Datta, S. K., 1991, "Characterization of Fibre-Matrix Interface by Guided Waves: Axisymmetric Case, " *Journal of the Acoustical Society of America*, **89**(6), pp. 2573-2583.

Zemanek, J., 1972, "An Experimental and Theoretical Investigation of Elastic Wave Propagation in a Cylinder," *Journal of the Acoustical Society of America*, **51**(1), pp. 265-283.

Zhu, J., 1996, "Numerical Modeling for Wave in Laminated Composite Plates," *Ph.D. thesis*, University of Manitoba, Winnipeg, Manitoba, Canada.

Zhu, J., Shah, A. H., and Datta, S. K., 1996, "The Evaluation of Cauchy Principal Value Integrals and Weakly Singular Integrals in BEM and Their Applications," *International Journal for Numerical Methods in Engineering*, **39**, pp. 1017-1928.

Zhuang, W., 1998, "Numerical Modeling for Elastodynamic Problems in Laminated Composite Cylinders," *Ph.D. thesis*, University of Manitoba, Winnipeg, Manitoba, Canada.

Zhuang, W., Shah, A. H., and Datta, S. K., 1997, "Axisymmetric Guided Wave Scattering by Cracks in Welded Steel Pipes," *Journal of Pressure Vessel Technology*, **119**, pp. 401-406.

Zhuang, W., Shah, A. H., and Dong, S. B., 1999, "Elastodynamic Green's Function for Laminated Anisotropic Circular Cylinders," ASME *Journal of Applied Mechanics*, **66**, pp. 665-674.

Appendix A

Propagator Matrix for an Isotropic Cylinder

For a hollow cylinder, the propagator matrix defined in Chapter 2 is expressed as a combination of Hankel functions. The first three columns of the Q_k matrix used in equation (2.22) are defined by,

$$Q_{11}(r) = \frac{m}{r} Z_m(\alpha r) - \alpha Z_{m+1}(\alpha r)$$

$$Q_{12}(r) = \xi Z_{m+1}(\beta r)$$

$$Q_{13}(r) = \frac{im}{r} Z_m(\beta r)$$

$$Q_{21}(r) = \frac{im}{r} Z_m(\alpha r)$$

$$Q_{22}(r) = -i\xi Z_{m+1}(\beta r)$$

$$Q_{23}(r) = -\frac{m}{r} Z_m(\beta r) + \beta Z_{m+1}(\beta r)$$

$$Q_{31}(r) = -i\xi Z_m(\alpha r)$$

$$Q_{32}(r) = -i\beta Z_m(\beta r)$$

$$Q_{33}(r) = 0$$

$$Q_{41}(r)=\mu\left\{\left[\frac{2m(m-1)}{r^2}+\xi^2-\beta^2\right]Z_m(\alpha r)+\frac{2\alpha}{r}Z_{m+1}(\alpha r)\right\}$$

$$Q_{42}(r)=2\mu\xi\left\{\beta Z_m(\beta r)-\frac{m+1}{r}Z_{m+1}(\beta r)\right\}$$

$$Q_{43}(r)=\frac{2i\mu m}{r}\left\{\frac{m-1}{r}Z_m(\beta r)-\beta Z_{m+1}(\beta r)\right\}$$

$$Q_{51}(r)=\frac{2i\mu m}{r}\left\{\frac{m-1}{r}Z_m(\alpha r)-\alpha Z_{m+1}(\alpha r)\right\}$$

$$Q_{52}(r)=i\mu\xi\left\{-\beta Z_m(\beta r)+\frac{2(m+1)}{r}Z_{m+1}(\beta r)\right\}$$

$$Q_{53}(r)=\mu\left\{\left[\beta^2-\frac{2m(m-1)}{r^2}\right]Z_m(\beta r)-\frac{2\beta}{r}Z_{m+1}(\beta r)\right\}$$

$$Q_{61}(r)=2i\mu\xi\left\{-\frac{m}{r}Z_m(\alpha r)+\alpha Z_{m+1}(\alpha r)\right\}$$

$$Q_{62}(r)=i\mu\left\{-\frac{\beta m}{r}Z_m(\beta r)+\left(\beta^2-\xi^2\right)Z_{m+1}(\beta r)\right\}$$

and

$$Q_{63}(r)=\frac{\mu m\xi}{r}Z_m(\beta r) \tag{A.1}$$

where $Z_m = H_m^{(1)}$ and m is the circumferential wave number. The other three columns of the Q_k matrix, which correspond to j = 4, 5, 6, can be obtained from the first three columns by replacing the Hankel function $H_m^{(1)}$ by $H_m^{(2)}$. The propagator matrix for the k^{th} sublayer is defined in equation (2.22). It is given by,

$$\mathbf{P}_k = \mathbf{Q}_{k+1}\mathbf{Q}_k^{-1} \tag{A.2}$$

where

$$\mathbf{Q}_k = \left[Q_{ij}\left(R_k\right)\right]_{6\times 6},\ \mathbf{Q}_{k+1} = \left[Q_{ij}\left(R_{k+1}\right)\right]_{6\times 6}.$$

For a solid cylinder, the innermost core is treated differently. Suppose R_0 is the radius of the innermost core. Then the stiffness matrix, **K**, in equation (2.27) is given, at layer $r = R_0$, by,

$$\mathbf{K} = \mathbf{T}\mathbf{R}^{-1} \tag{A.3}$$

where

$$\mathbf{R} = \begin{bmatrix} Q_{11}(R_0) & Q_{12}(R_0) & Q_{13}(R_0) \\ Q_{21}(R_0) & Q_{22}(R_0) & Q_{23}(R_0) \\ Q_{31}(R_0) & Q_{32}(R_0) & Q_{33}(R_0) \end{bmatrix},\quad \mathbf{T} = \begin{bmatrix} Q_{41}(R_0) & Q_{42}(R_0) & Q_{43}(R_0) \\ Q_{51}(R_0) & Q_{52}(R_0) & Q_{53}(R_0) \\ Q_{61}(R_0) & Q_{62}(R_0) & Q_{63}(R_0) \end{bmatrix}$$

and $Z_m = J_m$.

The dispersion relation defined in equations (2.30) and (2.31) for a hollow and solid cylinder can be evaluated through the matrices given in equations (A.2) and (A.3), respectively.

Appendix B

Specific Form of the Matrices in Equations (3.14) and (3.20)

The following matrices, which are used in Chapter 3 for wave scattering by a crack, are detailed here.

$$\mathbf{F}^R_{C,i,m} = \begin{bmatrix} f_{i1,m1} & f_{i1,m2} & \cdots & f_{i1,mN_m} \\ f_{i2,m1} & f_{i2,m2} & \cdots & f_{i2,mN_m} \\ \vdots & \vdots & \ddots & \vdots \\ f_{iP_C,m1} & f_{iP_C,m2} & \cdots & f_{iP_C,mN_m} \end{bmatrix} \in \mathbf{C}^{P_C \times N_m}, \quad i = r,\theta,z \tag{B.1}$$

$$\mathbf{F}^R_{N,i,m} = \begin{bmatrix} f_{iP_c+1,m1} & f_{iP_c+1,m2} & \cdots & f_{iP_c+1,mN_m} \\ f_{iP_c+2,m1} & f_{iP_c+2,m2} & \cdots & f_{iP_c+2,mN_m} \\ \vdots & \vdots & \ddots & \vdots \\ f_{iP_c+P_N,m1} & f_{iP_c+P_N,m2} & \cdots & f_{iP_c+P_N,mN_m} \end{bmatrix} \in \mathbf{C}^{P_N \times N_m}, \quad i = r,\theta \tag{B.2}$$

$$\mathbf{U}^R_{N,z,m} = \begin{bmatrix} u_{zP_c+1,m1} & u_{zP_c+1,m2} & \cdots & u_{zP_c+1,mN_m} \\ u_{zP_c+2,m1} & u_{zP_c+2,m2} & \cdots & u_{zP_c+2,mN_m} \\ \vdots & \vdots & \ddots & \vdots \\ u_{zP_c+P_N,m1} & u_{zP_c+P_N,m2} & \cdots & u_{zP_c+P_N,mN_m} \end{bmatrix} \in \mathbf{C}^{P_N \times N_m}, \tag{B.3}$$

$$\mathbf{U}^R_{C,i,m} = \begin{bmatrix} u_{i1,m1} & u_{i1,m2} & \cdots & u_{i1,mN_m} \\ u_{i2,m1} & u_{i2,m2} & \cdots & u_{i2,mN_m} \\ \vdots & \vdots & \ddots & \vdots \\ u_{iP_C,m1} & u_{iP_C,m2} & \cdots & u_{iP_C,mN_m} \end{bmatrix} \in \mathbf{C}^{P_C \times N_m}, \quad i = r,\theta,z \tag{B.4}$$

$$\mathbf{U}_{N,i,m}^{R} = \begin{bmatrix} u_{iP_c+1,m1} & u_{iP_c+1,m2} & \cdots & u_{iP_c+1,mN_m} \\ u_{iP_c+2,m1} & u_{iP_c+2,m2} & \cdots & u_{iP_c+2,mN_m} \\ \vdots & \vdots & \ddots & \vdots \\ u_{iP_c+P_N,m1} & u_{iP_c+P_N,m2} & \cdots & u_{iP_c+P_N,mN_m} \end{bmatrix} \in \mathbf{C}^{P_N \times N_m}, \quad i = r,\theta \tag{B.5}$$

$$\mathbf{F}_{N,z,m}^{R} = \begin{bmatrix} f_{zP_c+1,m1} & f_{zP_c+1,m2} & \cdots & f_{zP_c+1,mN_m} \\ f_{zP_c+2,m1} & f_{zP_c+2,m2} & \cdots & f_{zP_c+2,mN_m} \\ \vdots & \vdots & \ddots & \vdots \\ f_{zP_c+P_N,m1} & f_{zP_c+P_N,m2} & \cdots & f_{zP_c+P_N,mN_m} \end{bmatrix} \in \mathbf{C}^{P_N \times N_m} \tag{B.6}$$

The quantities appearing in the about matrices are the forces, $f_{rn,ml}$, $f_{\theta n,ml}$, $f_{zn,ml}$, as well as the displacements, $u_{rn,ml}$, $u_{\theta n,ml}$, $u_{zn,ml}$, which correspond to the circumferential wave number, m. Moreover, n is node number in radial direction and l is the axial wave number.

Appendix C

Dimensional Analysis of Green's Functions in a Cylinder

Equation Section 3The equations of harmonic motion for linear, isotropic elasticity are,

$$\sigma_{ij,j} + f_i = -\rho\omega^2 u_i \tag{C.1}$$

$$\sigma_{ij} = \lambda u_{k,k}\delta_{ij} + 2\mu\varepsilon_{ij} \tag{C.2}$$

$$\varepsilon_{ij} = \frac{1}{2}\left(u_{i,j} + u_{j,i}\right) \tag{C.3}$$

where λ and μ are the Lame constants, ρ is the mass density, ω is the circular frequency, f_i is the body force per volume, u_i is the displacement, and σ_{ij}, ε_{ij} are the stress and strain tensor, respectively. The dimension of each variable in equation (C.1) is,

$$[u_i] = m, [\sigma_{ij}] = \frac{N}{m^2}, [f]_i = \frac{N}{m^3}, [\omega] = \frac{\text{rad}}{s^2}, [\lambda] = [\mu] = \frac{\text{N}}{m^2}, [\rho] = \frac{\text{kg}}{m^3}. \tag{C.4}$$

Suppose H is the thickness of the cylinder. Introduce the following non-dimensional quantities,

$$R = \frac{r}{H}, \quad Z = \frac{z}{H} \tag{C.5}$$

$$U_i = \frac{u_i}{H}, \quad \Sigma_{ij} = \frac{\sigma_{ij}}{\mu} \tag{C.6}$$

with

$$c_2 = \sqrt{\frac{\mu}{\rho}} \text{ and } \Omega = \frac{\omega H}{c_2}. \tag{C.7}$$

Then the equations of motion in the non-dimensional cylindrical coordinate system (R, θ, Z) can be written as,

$$\Sigma_{ij,j} + F_i = -\Omega^2 U_i. \tag{C.8}$$

Here, differentiations are evaluated in the non-dimensional coordinate (R, θ, Z) and

$$F_i = \frac{H}{\mu} f_i. \tag{C.9}$$

Thus, the displacement and stress Green's functions, U_i and Σ_{ij}, are obtained by letting F_i = 1 (a non-dimensional value).